Reactive Ink Metallization

for Next Generation Photovoltaics

By
April M. Jeffries

Dissertation Presented in Partial Fulfillment
of the Requirements for the Degree
Doctor of Philosophy

Approved May 2019 by the
Graduate Supervisory Committee:

Mariana Bertoni, Chair
Zachary Holman
Rebecca Saive
Terry Alford

ARIZONA STATE UNIVERSITY

May 2019

ABSTRACT

In order to meet climate targets, the solar photovoltaic industry must increase photovoltaic (PV) deployment and cost competitiveness over its business-as-usual trajectory. This requires more efficient PV modules that use less expensive materials, and longer operational lifetime. The work presented here approaches this challenge with a novel metallization method for solar PV and electronic devices.

This document outlines work completed to this end. Chapter 1 introduces the areas for cost reductions and improvements in efficiency to drive down the cost per watt of solar modules. Next, in Chapter 2, conventional and advanced metallization methods are reviewed, and our proposed solution of dispense printed reactive inks is introduced. Chapter 3 details a proof of concept study for reactive silver ink as front metallization for solar cells. Furthermore, Chapter 3 details characterization of the optical and electrical properties of reactive silver ink metallization, which is important to understanding the origins of problems related to metallization, enabling approaches to minimize power losses in full devices. Chapter 4 describes adhesion and specific contact resistance of reactive ink metallizations on silicon heterojunction solar cells. Chapter 5 compares performance of silicon heterojunction solar cells with front grids formed from reactive ink metallization and conventional, commercially available metallization. Performance and degradation throughout 1000 h of accelerated environmental exposure are described before detailing an isolated corrosion experiment for different silver-based metallizations. Finally, Chapter 6 summarizes the main contributions of this work.

DEDICATION

To William and Sophia.

ACKNOWLEDGEMENTS

Thank you to my committee, my family, and my friends for their time, support, and encouragement. I would also like to thank the National Science Foundation and Department of Energy for the funding to make this work possible. Most importantly, I would like to thank Mariana Bertoni for taking me in as her guinea pig, pushing me to do my best work and constantly grow, and for her support and encouragement through the rough patches. Steven Jeffries, thank you for being the earliest believer in me and my abilities, teaching me calculus, and moving from a comfortable life out to Arizona to struggle a little bit with me. Joe Karas, thank you for being my partner, your dedication to my success, health, and well-being (and of course for your numerous edits). Lastly, I would like to thank my past self for wholly living outside of my comfort zone, and not opting for the easier path through these 6 challenging and transformative years.

TABLE OF CONTENTS

CHAPTER Page

I. LIST OF FIGURES vii

II. LIST OF TABLES xvii

1. INTRODUCTION 1

1.1 Motivation: Climate, Levelized Cost of Energy & Metallization 2

1.1.1 Module Production Costs 3

1.2 Metallization Requirements 8

1.2.1 Media Resistivity 12

1.2.2 Optical & Geometric Considerations 14

1.2.3 Specific Contact Resistance & Adhesion 15

1.2.4 Performance Over Time 16

1.2.5 Summary 17

2. CONVENTIONAL & STATE-OF-THE-ART METALLIZATIONS 19

2.1 Screen-Printing of Silver Pastes 19

2.2 Stencil Printing 24

2.3 Copper Pastes 25

2.4 Metal Plating 26

2.5 Dispense Printing of Particle-Based Inks & Pastes 27

2.6 Dispense Printing of Reactive Inks 30

2.6.1 Introduction to Reactive Inks 31

CHAPTER Page

2.6.2 State-of-the-Art Reactive Inks ... 36

3. REACTIVE SILVER INK METALLIZATION PROPERTIES ... 39

3.1 Proof-of-Concept for Dispense Printed Reactive Inks for Solar Cell Front Metallization ... 40

3.1.1 Drop-on-Demand Reactive Silver Inks for Solar Cell Front-Grid Metallization: Proof of Concept ... 40

3.2 Optical and Electrical Properties of Reactive Silver Ink Metallization ... 50

3.2.1 Optical Characterization of RSI ... 50

3.2.2 Electrical Characterization of Reactive Silver Ink ... 55

4. ADHESION & SPECIFIC CONTACT RESISTANCE ... 65

4.1 The Effect of In-Filling on Adhesion Performance ... 65

4.2 Properties of a Sn-Sensitization Adhesion Promoting Layer ... 68

4.2.1 Introduction to Sn-Sensitization with $SnCl_2$ Solutions ... 69

4.3 Development of a Printable Sn-Sensitization Solution for Indium Tin Oxide Thin Films ... 71

4.3.1 ITO Surface Cleaning & Hydroxylation ... 71

4.3.2 Sn-Sensitization Solution Formulation: A First Approximation ... 75

4.4 Properties of a Printed Sn-Sensitization Layer ... 76

4.4.1 Adhesion of a Printed Sn-Sensitization Layer ... 76

4.4.2 Electrical Properties of a Printed Sn-Sensitization Layer ... 78

CHAPTER Page

4.4.3 The Effect of Sn-Sensitization Solutions on Work Function of ITO...... 85

4.4.4 The Effect of HCl Concentration on ITO... 88

4.4.5 The Effect of Rinsing Sn-Sensitization Solution from Indium Tin Oxide Surface 91

4.5 Tin Sensitization and Silver Activation on Indium Tin Oxide....................... 96

5. DEVICE PERFORMANCE & DEGRADATION STUDIES 105

5.1 Performance of Silicon Heterojunction Solar Cells with RSI and SP Ag Paste 105

5.1.1 Printing Process Variation & Optimization Opportunities 110

5.2 Reliability & Performance of RSI and SP Ag Paste Cells Through Damp Heat 113

5.3 Corrosion of Silver-Based Metallizations in Diluted Acetic Acid 123

6. SUMMARY OF REACTIVE SILVER INK METALLIZATION FOR NEXT GENERATION PHOTOVOLTAICS... 131

7. ACCOMPLISHMENTS.. 133

7.1 Peer-Reviewed Journal Publications 133

7.2 Patents.. 133

7.3 Conference Proceedings 134

7.4 Presentations... 135

7.5 Awards... 136

CHAPTER Page

8. REFERENCES 137

LIST OF FIGURES

Figure Page

1. Current and prospective module production costs for traditional c-Si and SHJ technologies broken down into components, data taken from [7]. Metallization (red) accounts for the largest non-Si cost at the cell level for c-Si, for SHJ technology the cost from metallization is even more significant. 5
2. Projected amount of Ag/cell used to form front contacts, values taken from [8]. This shows current c-Si cells use around 100 mg Ag/cell and is expected to reduce to 40 mg Ag/cell by 2026... 7
3. Schematic of a simple front grid pattern (in red) and active front region of a solar cell (outlined in light grey). Power losses are described in relation to the shown dimension.. 8
4. Effective media percolation model for resistivity of porous Ag as a function of porosity. Modeled following McLachlan's approximation for an asymmetric medium Ag host [23]. As f approaches 1, the media resistivity of porous Ag (solid red line) approaches the bulk resistivity of Ag (dashed black line)..................... 13
5. Schematic showing the process of screen printing paste onto a solar cell. Schematic was modified from an original figure by Aleeva and Pignataro [27].. 20
6. Schematic of high-temperature glass frit Ag paste firing through a SiNx layer on Si. (a) Shows the etching through the SiNx by the PbO in the frit, (b) shows Ag–Pb alloying, (c) shows Ag moving through molten frit and deposition at the Si interface, and (d) shows the final fired-finger morphology, with a sintered Ag particle network in glass. Schematic taken from Fields *et al.* [30]...................... 21

Figure Page

7. Examples of fingers printed with low-temperature Ag paste by screen-printing (a), and stencil printing (b-e). The cross-sectional image in e) shows the high aspect ratio that is achieved using double-print stencil printing. Figure taken from De Wolfe *et al.* [31]. 25

8. Scanning electron microscope image of a cross-sectional view of a Ni-Cu finger plated by light induced plating, with finger width less than 50 µm, and height of 16-18 µm. Figure taken from Lennon *et al*. [39]. 26

9. SEM images of a screen-printed paste finger, dispense printed with 40 µm nozzle (left), and a narrower, high aspect ratio modified paste, dispense printed finger with a 40 µm nozzle diameter (right). Figure taken from Pospichil *et al*. [34]. ... 28

10. Schematic of chemical sintering process of metal nanoparticles with a capping agent, taken from Glunz *et al*. [45]. 29

11. Particle-based inks and pastes consist of conductive particles (grey circles) suspended in solvents and ink/paste modifiers (such as glass-frit or binders, represented by red circles). Reactive inks are particle-free precursors to a chemical reaction that once printed begin to reduce metal ions (M^+) and precipitate solid metal (represented by grey circles). Reactive inks can be formed at mild temperatures with chemical sintering, whereas particle-based inks require high temperatures to thermally sinter conductive particles. 32

12. (a) Schematic of dispense printing of reactive ink. (b-f) Parameters that influence the resulting metallization properties, along with the properties that are most

Figure Page

heavily influenced by changes in the corresponding parameter. R denotes resistance, ρ_m is media resistivity, ρ_c is specific contact resistance, and α is adhesion. 34

13. Media resistivity of RSI-printed pads formed for various substrate temperatures compared with the resistivity of pure Ag, and SP Ag paste pads after curing for 20 min at 200 °C, showing that the media resistivity of RSI is lower than SP paste when printed at low temperatures. Figure taken from our publication [55]. 44

14. Reflectance spectra of a DoD RSI metallization pad, an SP paste metallization pad, and a pure Ag mirror from [63]. Figure taken from our publication [55]..... 45

15. Schematic of SHJ solar cell layers in cross-sectional (a) contrast enhanced photograph of SHJ solar cells with front-grid metallization formed from (b) SP paste and (c) DoD RSI. Figure taken from our publication [55]. 46

16. SEM cross-sectional image of a porous DoD RSI finger on a textured SHJ solar cell. Figure taken from our publication [55]. 47

17. One-sun and suns–V_{oc} – I–V curves for SHJ solar cells with front-grid metallizations formed from SP paste (top) and DoD RSI (bottom). Figure taken from our publication [55]. 49

18. Finger width (w_f) and surface metal coverage of a DoD-printed RSI finger as a function of number of printing passes, for RSI prepared with solvent:ink ratios of 10:1, 5:1, and 1:1. 51

19. Optical properties of RSI for varying number of printing passes (layers) and solvent:ink ratios. 52

Figure Page

20. Schematic of RSI film morphology for varying number of print passes, and solvent:ink ratios. 53

21. Schematic of the in-filling process. A reactive ink (blue) is deposited onto a heated substrate. The ink is allowed to dry completely and volatilize all residuals before printing additional layers, resulting in a less porous feature than the previous layer. 56

22. Schematic of RSI lines printed on ITO coated Si polished substrate. The use of the evaporated Ag pads allows electrical probing without damaging the RSI pads. 57

23. Line resistance of five 5-mm-long RSI lines for 3-, 5-, and 7-layers with time delay between printing consecutive layers, and 5-layers RSI lines with no time delay between printing consecutive layers. The no-time-delay 5-layers lines have higher average resistance compared to the time-delay 5-layers lines despite having the same amount of Ag per line. The arrow indicated lines that were further characterized by x-ray transmission.......... 58

24. Top-view optical microscope images of each RSI lines indicated by arrows in Figure 23. Line resistance of five 5-mm-long RSI lines for 3-, 5-, and 7-layers with time delay between printing consecutive layers, and 5-layers RSI lines with no time delay between printing consecutive layers. The no-time-delay 5-layers lines have higher average resistance compared to the time-delay 5-layers lines despite having the same amount of Ag per line. The arrow indicated lines that were further characterized by x-ray transmission.. This qualitatively shows the

Figure Page

difference in RSI morphology for time-delay RSI lines and no-time-delay RSI line. 60

25. Average cross-sectional profiles determined from profilometry mapping of the entire length of RSI lines (blue and red profiles), and cross-sectional thickness of pure Ag from synchrotron x-ray transmission (grey profiles). The average cross-sectional area A from profilometry is used to determine ρ_m, and the cross-sectional thickness of pure Ag is used to determine the porosity. 62

26. Media resistivity of RSI lines compared to the resistivity of pure Ag (dashed line). For the RSI lines with time-delay between printing of layers, the media resistivity decreases as number of layers increases, suggesting in-filling of pores as additional layers are printed on top of the dried RSI. 64

27. (a) SEM images of 3, 7, and 15-layer RSI samples after tape peel testing.; (b) Load versus extension plots for the 3, 7, and 15-layer RSI lines are shown. L_1, L_2, L_3 denotes location of the three RSI lines printed on the ITO films. Figure taken from Mamidanna *et al*. [67]. 66

28. Optical microscope images of a region of the front grid of the RSI SHJ cell without the use of an adhesion promoter before and after IV testing. This shows finger dislodgement from a probe scratch during IV characterization. This exemplifies the importance of improving the durability of RSI metallization for solar cells. 68

29. Sn-sensitization and Ag-activation on a glass surface. Taken from Wei and Roper [53]. 70

Figure Page

30. Effect of oxygen plasma duration on ITO sheet resistance, and droplet wettability on ITO films. ... 72

31. Top-down optical microscope images of RSI printed on ITO films with varying concentrations of a Sn-sensitization layer, before (left) and after (right) qualitative scratch tests. Top row shows a control with D.I. water printed prior to RSI printing. ... 77

32. Schematic of TLM test structure used to determine specific contact resistance of RSI pads to ITO. S1, S2… are the spacing between adjacent RSI pads. The use of the evaporated Ag pads allows electrical probing without damaging RSI pads. Schematic is not drawn to scale. ... 79

33. Resistance of each RSI pads printed with the same concentration of Sn-sensitization solution. Pad resistances of three samples with no-time-delay between printing layers (a), and pad resistances from three samples with time-delay between layers (b). Note that the pad resistance scales vary by an order of magnitude. Consistent, low resistance values are shown for each RSI pad when a time-delay (b) is employed, this range in indicated by the blue region in (a). These measurements are done prior to TLM; consistent pad resistance values are a requisite for determining specific contact resistance values using the TLM method. ... 81

34. Boxplots showing the range of RSI pad resistances for varying Sn-sensitization solution concentrations, and for pads printed with no-time-delay between layers (left) and for pads that were allowed to dry before printing additional layers (right). This shows that the resistance varies significantly when the ink is not

Figure Page

allowed to dry before printing additional layers. Also, this shows that the resistance of the RSI pad does not change with increasing Sn-sensitization solution concentration. The numbers above each box indicate the number of samples. [HCl] molar concentration is twice that of [$SnCl_2$]............................... 82

35. An example of TLM results showing the resistance between adjacent RSI pads as a function of pad spacing. The trend lines, which are well-fitted with the data points, are used to extrapolate the specific contact resistance. 83

36. Boxplot of specific contact resistance range for all TLM samples prepared with varying concentrations of Sn-sensitization solution. The numbers adjacent to each box is the total number of samples represented in the boxplot. [HCl] molar concentration is twice that of [$SnCl_2$]. 84

37. Relative change in work function of ITO films before and after treatment with Sn-sensitization solutions of varying concentrations ([$SnCl_2$]: [HCl] is 1:2). Note that actual work function is not accurate for measurements conducted in ambient atmosphere due to modified surface termination of reference sample. 86

38. Profilometry of ITO films after pipetting Sn-sensitization solutions with varying concentrations of $SnCl_2$ and HCl ([$SnCl_2$]: [HCl] is 1:2). 88

39. SEM images of ITO films with Sn-sensitization solutions of varying concentrations pipetted on the surface and allowed to dry fully prior to imaging. a) 0.046 mM $SnCl_2$, 0.092 mM HCl, b) 0.46 mM $SnCl_2$, 0.92 mM HCl, and c) 4.6 mM $SnCl_2$, 9.2 mM HCl. 90

Figure Page

40. Schematic showing processing steps for an experiment to determine the effect of Sn-sensitization solutions on the change in work function of ITO surfaces, before and after rinsing away particulate residue. [HCl] molar concentration is twice that of [$SnCl_2$]. 94

41. CPD maps of ITO films as deposited (top row), after pipetting D.I. water or Sn-sensitization solution (middle row), and after thoroughly rinsing off particulate residue (bottom row), showing the effect of Sn-sensitization solutions on the ITO surface work function. [HCl] molar concentration is twice that of [$SnCl_2$]. 95

42. Simplified schematic showing the steps for Sn-sensitization and Ag-activation of a glass or ITO surface. 97

43. Schematic showing samples ITO and glass samples prepared for XPS study. .. 100

44. XPS spectra of glass and ITO samples treated with various steps of the Sn-sensitization and Ag-activation process. Binding energies of elements of interest are labeled under the spectra. D_{ITO} and D_{glass} were treated with identical processes, following de Minjer *et al.*, showing that the same process used on glass does not work identically on ITO [71]. Figure taken from our publication, which is reported in full detail elsewhere [90]. 101

45. Schematic showing Pd-activation vs Ag-activation on ITO surfaces. 103

46. Efficiency (a), R_s (b), J_{sc} (c), and V_{oc} (d) are shown for 4 cm^2 SHJ cells with front grids formed from RSI formula 1 (teal circles), RSI formula 2 (grey diamonds), and SP Ag Paste (red squares). Boxplots are overlaid on the four data points for each type of metallization to show the mean (black square) and median (horizontal line). 107

Figure Page

47. Optical microscope images of two RSI f1 fingers printed on ITO-coated textured Si. Fingers were printed with similar printing parameters. However, the resulting line widths are significantly different, showing the variation in contact angle of the reactive ink on ITO surfaces. a) High contact angle finger with w_f of 210 µm. b) Low contact angle finger with w_f of 503 µm. 110

48. Normalized power and series resistance throughout 1000 h of damp heat exposure (IEC 61215) for mini cells (4 cm^2) with front grids formed from RSI formula 1 (a,d), RSI formula 2 (b,e), and a low-cure temperature SP Ag Paste (c-f). 114

49. Normalized power (a), efficiency (b), V_{oc} (c), and R_s (d) throughout 1000 h of damp heat exposure (IEC 61215) for full-sized cells (239 cm^2) with front grids formed from RSI formula 1 (green circles), and a low-cure temperature SP Ag Paste (red squares). Line color connecting data points for each individual sample are kept the same for (a-c), and in Figures 50-51. 118

50. Photoluminescence of full-sized cells before and after 1000 h of Damp Heat (IEC 61215). The colored lines next to the sample names indicate the colored lines for each sample shown in Figure 49. 120

51. Electroluminescence of full-sized cells before and after 1000 h of damp heat exposure (IEC 61215). The colored lines next to the sample names indicate the colored lines for each sample shown in Figures 49 and 50. 121

52. Photograph showing the experimental setup for exposing metallization pads to diluted acetic acid by leaching the solution through a cellulose sponge. This figure is copied from our publication, which is reported elsewhere [116]................... 124

Figure Page

53. The $B_{C\text{-}O\text{-}Ag}$ mode of silver acetate is indicated by an asterisk. The $V_{Pb\text{-}OH}$ mode of lead acetate is indicated by a filled diamond. The V_{SiO4} mode from the leaded glass frit is indicated by the filled-black circle. The V_{Ag}, $B_{C=O}$, and R_{CH3} modes for silver acetate are indicated by the unfilled circle, triangle, and square, respectively. 125

54. Boxplots showing the distribution of the $B_{C\text{-}O\text{-}Ag}$ and $V_{Pb\text{-}OH}$ for HT Ag Paste (a), and $B_{C\text{-}O\text{-}Ag}$ for RSI (b), and average slope of the background from 200-1250 cm^{-1} for LT Ag Paste throughout 3000 h of exposure to diluted acetic acid. The colored-box region shows the 25th - 75th percentile, and the whiskers extend to ±1 inner quartile range from the colored-box. The mean is shown by the white square, and the median is shown by a horizontal black line. (a) and (b) are copied from our publication reported elsewhere [116]. 126

LIST OF TABLES

Table Page

1. Comparison of Silver and Sopper Properties. 38

2. Comparison of Solar Cell Electrical Characteristics for One SP Paste Cell, and One DoD RSI cell. 47

3. Pd and Ag ionic cross-sectional areas and hydroxide site density for ITO and glass surfaces. 103

4. Front-Grid Metallization Properties. 106

5. Summarized experiments and findings used to determine the cause for variation in contact angle, θ, for various ITO-coated samples. 111

6. XPS results for ITO-coated textured Si wafers with varying relative contact angles. 112

1. INTRODUCTION

Increases in anthropogenic emission of greenhouse gasses, primarily carbon dioxide, are widely accepted in the scientific community to have resulted in more frequent and more severe heat waves, precipitation events, and storms; acidification of the oceans; rising of the sea-level; and increased vulnerability of human and natural systems. Continuing increases of carbon dioxide emissions over the coming decades are projected to lead to resource scarcity, competition over food and water resources, mass displacement of populations and international political volatility [1]. Avoidance of such detrimental effects of climate change requires the world's carbon dioxide emissions to be curbed in the approaching decades; This could be achieved by deployment of over 10 terawatts of renewable energy generation, such as solar photovoltaics, to phase out more carbon-intensive energy generation [2]–[4].

Trends predicting the deployment of photovoltaics in the upcoming decades show that with business-as-usual, the photovoltaics industry will fall short (by 2-9 TW) of reaching these climate-targets for two main reasons. First, although high cumulative annual growth rates of over 50% in recent years, growth rates are still limiting such high manufacturing capacity and deployment, and second, costs for consumers need to be even more competitive to generate and sustain enough demand [2], [5]. Economic viability of PV technology is dictated by levelized cost of energy (LCOE) for solar PV compared to competing generation sources [6]. The following chapters outline contributions to LCOE, namely cost components of photovoltaic modules, device efficiency, reliability and durability in order to target significant opportunities for photovoltaic manufacturing growth while reducing LCOE for consumers. Specifically, I detail the motivation for

studying novel metallizations –reactive silver inks—their electrical, optical, geometric properties, as well as durability and reliability.

1.1 Motivation: Climate, Levelized Cost of Energy & Metallization

Before reaching climate targets with deployment of terawatts of low-carbon energy, as an industry, photovoltaic module manufacturers must ensure their long-term financial sustainability. Over the past several decades, the photovoltaic industry has seen a decrease in average sale prices following a predictable learning curve. However, in more recent times moments of slack demand have yielded periods of global oversupply of photovoltaic modules. This oversupply drove photovoltaic manufacturers to search for paths to reduce production costs to ensure successful continuation of their ventures [7]. One clear path to reducing production costs is to replace expensive processes and materials with less expensive options. This has already lead to significant cost reductions for existing manufacturing [7], [8]. Yet, simply reducing manufacturing costs alone will not ensure low-enough LCOE for widespread adoption of solar photovoltaic energy generation [9].

$$\mathrm{LCOE} = \frac{\text{total lifecycle cost of PV (\$)}}{\text{lifetime energy production (kWh)}} \qquad \text{Equation 1.1}$$

Levelized cost of energy in its simplest form is the total lifecycle cost of PV over the lifetime energy production (Equation 1.1) [9]. Total lifecycle cost is dependent on capital expenditures (such as module materials, manufacturing equipment, labor, installation hardware, transactional costs for financiers and installers, etc.) in addition to operational and maintenance costs [9], [10]. In addition, lifetime energy production is dependent on module and system performance and reliability, and geographic location of system [9]. In this work, module production costs for Si-heterojunction

(SHJ) architectures are studied as part of the total lifecycle cost of PV; Efficiency, reliability, and durability are studied as part of the lifetime energy production.

In the following chapters, two different Si-based cell architectures (diffused-junction crystalline-Si, and SHJ) are introduced before breaking down the current and projected prospective module production costs. Next, the two cell architectures are compared in terms of current and prospective module production costs and efficiency. A pathway for the new cell architecture to lower module production costs and higher efficiency (lower LCOE) is explained and motivates the studies for novel metallization detailed in the remainder of this work.

*1.1.1 **Module Production Costs***

New solar cell technologies can reduce costs even beyond what is projected for the present industry standard technology. Currently, about 90% of the market share is made up of silicon photovoltaics, primarily diffused-junction crystalline-Si (c-Si) solar cells [8]. Other technologies, including thin-film, carrier-selective-contact (CSC) and silicon heterojunction (SHJ) solar cells, are expected to expand their market share in the next decade [8].

A comparison of c-Si and SHJ current and prospective module production costs in U.S. dollars per peak watt ($\$/W_p$) are shown in Figure 1. Module production costs represented in Figure 1 were taken from a study conducted by Louwen *et al.* [7], where a detailed analysis of production costs was performed using costs associated with standard processes including equipment, materials and energy. The module component of the total module production cost comes from the costs associated with making the module, however the key to reducing module production costs is to increase overall module efficiency in order to

use less module material per watt [7][11]. Again, LCOE can be reduced by reducing the cost of manufacturing and materials and increasing efficiency, reliability, and manufacturing yield.

The Si-based architectures discussed in Figure 1 both start with the production of the monocrystalline-Si wafer, which is the largest cost component of the modules. Production of these Si wafers is an expensive and energy intensive process, starting with reducing silica sand at temperatures (~1900 °C), then refining it to produce metallurgical grade Si, which has a purity of about 98.5-99.5 %. Metallurgical grade Si is further refined to make high purity (>99.99 %) solar-grade silicon. The high purity Si is pulled into a monocrystalline ingot through the Czochralski process and sawn into individual wafers, resulting in large waste (kerf-loss) of this high purity Si. It should be noted that the module cost structure for thin film devices differs significantly, as the main contribution to the production costs are from custom designing, installing, and debugging a large scale manufacturing line [12].

Figure 1 shows that currently Si wafers account for approximately 45% of the c-Si module production cost. Solutions to high kerf-loss in Si ingots are currently under investigation by Coll and colleagues, where low-temperature spalling of Si wafers aims to nearly eliminate all kerf-loss [13]. Another more efficient use of Si through the use of thinner wafers results in reduced wafer costs [7], [8]. Though thinner wafers could reduce wafer costs, an adverse risk associated with this is easier wafer breakage during processing and handling, leading to lower yields or the need to replace standard processes with more delicate ones. Current wafer costs for c-Si are \$0.22 /W_p USD and are projected to decrease to \$0.18 /W_p due to decreasing wafer thickness and kerf-

losses, but also due to gains in module efficiency translating to even more efficient use of Si [7].

SHJ technology has gained significant attention in recent years due to its relatively simple fabrication processes that results in high efficiency cells, which additionally reap large benefit of utilizing thinner wafers compared to c-Si technology. Current to prospective costs associated with wafers from SHJ cells are \$0.19 /W_p to \$0.14 /W_p USD, respectively.

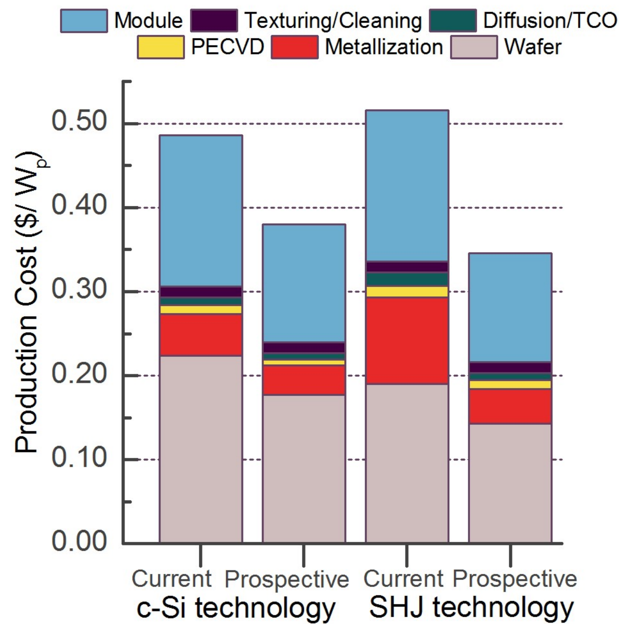

Figure 1. Current and prospective module production costs for traditional c-Si and SHJ technologies broken down into components, data taken from [7]. Metallization (red) accounts for the largest non-Si cost at the cell level for c-Si, for SHJ technology the cost from metallization is even more significant.

In both c-Si and SHJ technologies, metallization (shown by the red bars in Figure 1) accounts for the largest non-Si cost component of the cell. Industrial metallization for Si solar cells is formed from Ag particle-based pastes. Unfortunately, Ag prices can be expensive, and quite volatile. For example, in January 2011 Ag was 0.89 \$/g USD, and by April 2011 the price rose to 1.43 \$/g USD [14]. This spike in Ag price occurred

simultaneously with a period of slack demand and global oversupply of photovoltaic modules, further increasing the hardships faced by many solar cell manufacturers. At this time, it became clear to the PV community that if growth of PV deployment continued following current projections and Ag price volatility continued, the amount of Ag used on solar cells needed to be reduced [15].

Accordingly, reductions in metallization costs can be achieved by 1) reducing amount of Ag, and 2) replacing high-cost materials with less expensive options [7], [8]. The International Technology Roadmap for Photovoltaics (ITRPV) projection shown in Figure 2 shows a trend for expected reductions in Ag usage for standard 156 ×156 mm^2 c-Si solar cells [8]. This projection is based on the known technical reductions (such as improving resistivity of pastes for more efficient use of Ag) that are currently considered state-of-the-art techniques, but are expected to be adopted into industrial processes over the next decade [8]. Chapter 1.2 discusses in more detail the limit to which the amount of metallization can be reduced before detrimentally affecting the efficiency of the device, and Chapter 2.6 details current industry standard metallization practices, and advanced metallization methods to reduce the amount of Ag used in solar cell manufacturing.

Currently, the total amount of Ag used for c-Si solar cells is approximately 100 mg/cell, while SHJ cells require an estimated 200 mg/cell [7], [8]. Figure 1 shows the reduction in metallization cost is more pronounced for SHJ technology: for c-Si metallization a minor cost is decrease from \$0.05 /W_p to \$0.04 /W_p is expected, while SHJ metallization decreases by more than half from \$0.10 /W_p to \$0.04 /W_p. Both technologies employ a screen-printed Ag paste as the standard metallization. For c-Si,

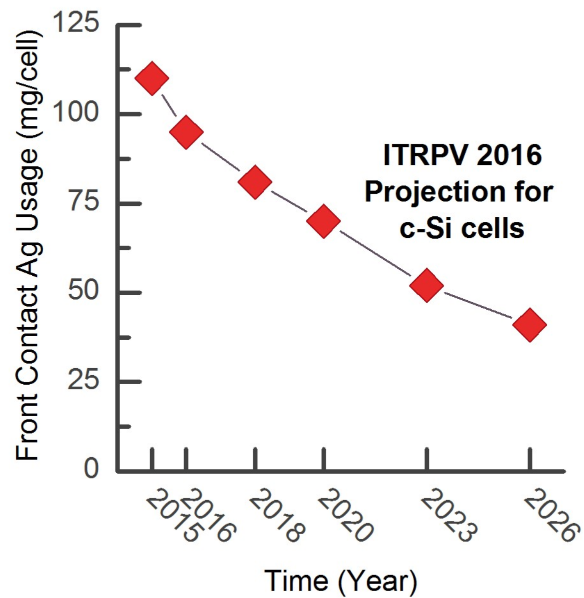

Figure 2. Projected amount of Ag/cell used to form front contacts, values taken from [8]. This shows current c-Si cells use around 100 mg Ag/cell and is expected to reduce to 40 mg Ag/cell by 2026.

the Ag paste contains glass frit that must be fired at temperatures in excess of 700 °C to break through the front antireflective coating (SiN_x) and alloy the interface to form low-resistance ohmic contact. This Ag-frit paste typically used for c-Si technology cannot be used on SHJ cells as cells are substantially more thermally sensitive. Passivation of SHJ cells provided by hydrogenated amorphous Si begins to degrade at temperature just above 200 °C. Therefore, SHJ cells rely on a different type of Ag paste that can be cured at low-temperature, which consequently requires a higher silver content to achieve low resistances compared to the c-Si counterpart. Additionally, the lack of economy of scales for these cells drives the prices of the low-temperature Ag paste higher. Other emerging photovoltaic technologies, such as some CSC and perovskite solar cells, require low-temperature metallization as well due to thermally sensitive layers within the device [16][17]. Of course, this concern is valid outside of the field of photovoltaics as well; realization of low-

temperature metallization methods can expand opportunities for flexible electronics, and organic optoelectronic devices [18].

Photovoltaic module efficiency is the most influential variable of module production cost in $/W$_p$ [7], [11], [19]. Therefore, any efforts to reduce any one cost component, such as metallization, should not sacrifice module efficiency. Following this principle, this work evaluates metallization methods based on whether the cost of metallization can be decreased while maintaining or even improving device efficiency through the use of advanced processes or new materials.

1.2 Metallization Requirements

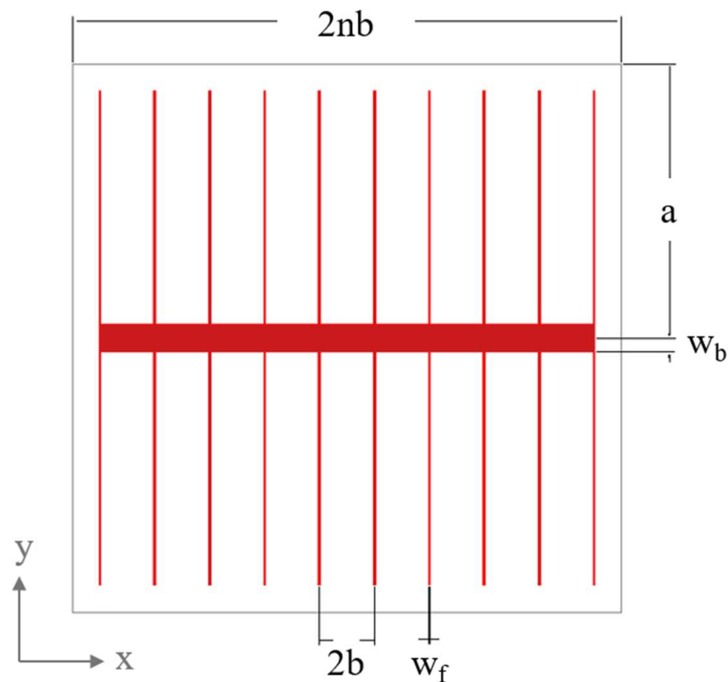

Figure 3. Schematic of a simple front grid pattern (in red) and active front region of a solar cell (outlined in light grey). Power losses are described in relation to the shown dimension.

The amount of Ag required in front grid metallization is determined by the power losses a manufacturer is able to endure [15]. An ideal solar cell front grid would have

no resistance and be completely transparent. In reality, there are power losses from resistive voltage drop in the grid and in photogenerated current from shading from the grid. Resistive losses are inherent due to intrinsic resistivity of metallization, at room temperature Ag is the lowest resistivity material, followed by Cu, and Al. Furthermore, there are power losses from interfacial resistance between the grid and solar cell, and throughout time as degradation occurs.

Front grids are designed to minimize resistive and optical power losses. A typical front grid design is shown in Figure 3, denoting the width and length of fingers, the spacing between fingers, width of busbars, and dimensions of the active front region of a solar cell. Losses from shading can be minimized by using fewer fingers, forming high aspect ratio fingers (narrow width, high height), and by busbarless designs. However, the gains from reduced shading must not be offset by additional resistive losses in the grid. These resistive power losses are not only dependent on the resistivity of the metallization and the contact resistance between metal and cell, but also on the geometry (larger cross-sectional areas have lower resistance), and also on design parameters such as spacing, and number of fingers and busbars.

Total power loss in a solar cell can be quantified and broken down into components associated with various regions of the device. This chapter discusses initial power losses associated with metallization. However, before breaking down power losses, important solar cell parameters need to be described to understand the influence of power losses on the performance of a solar cell. Current voltage (IV) characteristics are commonly used to describe the performance of solar cells; this measurement is characteristically done under one-sun illumination, measuring the voltage as a resistive load swept from short circuit to

open circuit conditions [20]. For a solar cell that behaves like an ideal diode, the IV characteristics can be described by the following [20]:

$$I = I_{recomb.} - I_{gen.} - I_{ph} = I_o\left\{\exp\left(\frac{qV}{kT}\right) - 1\right\} - I_{ph} \qquad \text{Equation 1.2}$$

I_{ph} is the light generated current (which is proportional to the intensity of the light). In reality, a solar cell does not operate as a simple ideal diode; series resistance R_s (a resistance in series with the diode) and shunt resistance R_p (a resistance in parallel with the diode) are also present in the device, and these contributions influence the IV characteristics. The equation describing a one-diode solar cell with these contributions is as follows [20]:

$$I = I_o\left\{\exp\left[\frac{q(V-IR_s)}{kT}\right] - 1\right\} + \frac{V-IR_s}{R_p} - I_{ph} \qquad \text{Equation 1.3}$$

An additional correction still must be made to adequately describe the IV characteristics of a real solar cell, this correction accounts for recombination at the junction, which can be represented by the addition of a non-ideal diode (with ideality factor greater than 1) in parallel with the ideal diode (with an ideality factor of 1). The following equation describes this situation:

$$I = I_{01}\left\{exp\left[\frac{q(V-IR_s)}{m_1 kT}\right] - 1\right\} + \frac{V-IR_s}{Rp} - I_{ph}$$

$$+ I_{02}\left\{exp\left[\frac{q(V-IR_s)}{m_2 kT}\right] - 1\right\} + \frac{V-IR_s}{Rp} - I_{ph} \qquad \text{Equation 1.4}$$

where q is electronic charge, k is the Boltzmann constant, m is a dimensionless constant (1 for idea diodes, and typically between 2.5 and 3 for the non-ideal component), T is the temperature in K, I_0 is the diode saturation current which comes from material properties, and I and V are the current and voltage measured at the terminals [20].

Power losses in a solar cell are associated with various regions across the device. As current travels across each layer and through each interface of the solar cell power

is lost. Resistive losses can be lumped into a singular term called the series resistance, R_s, which appears in Equations 1.3-1.4. The generalized total power loss in a solar cell can be described by the following:

$$P_{LT} = P_{LStack} + P_{LSheet} + P_{LGrid} + P_{LShading} + P_{LContact} \qquad \text{Equation 1.5}$$

Power is lost as current travels through the solar cell stack layers (P_{LStack},) and interfaces (here we include the contribution from back metallization and its interface), P_{LSheet}, the two-dimensional sheet under the metallization to reach the grid, P_{LGrid}, the front metallization grid, $P_{LContact}$, the interface between the front grid and the underlying layer of the solar cell. Additional power is also lost from shading from metallization, which is shown in the $P_{LShading}$ term.

Since this work is focused on front grid metallization of solar cells, only contributions related to the non-design parameters of the front grid will be described in detail. That is, complete grid optimization is not a focus of this work, but it is practically implemented when appropriate.

The following equations detail the importance of several characteristics of solar cell front grid metallization for an example grid shown in Figure 3. The following power losses are described for a cell that is *a* units long and *2nb* units wide following derivations described in full detail by Meier *et. al.* [21]. The total power loss associated with the metallization is therefore:

$$P_{LMetal} = P_{LGrid} + P_{LShading} + P_{LContact} \qquad \text{Equation 1.6}$$

The following subsections detail contributions to P_{LMetal}, and power losses due to degradation throughout time. These factors contribute to metallization performance and degradation are summarized into four categories that will be used to evaluate novel

metallization in this work; 1) media resistivity; 2) optical and geometric properties; 3) specific contact resistance and adhesion (denoted as α); and 4) performance through time.

*1.2.1 **Media Resistivity***

Power loss from the front grid metallization alone is the sum of the power loss from current traveling through the finger ($P_{LFinger}$) and the busbar (P_{LBus}):

$$P_{LGrid} = P_{LFinger} + P_{LBus} \qquad \text{Equation 1.7}$$

$$P_{LFinger} = \frac{4}{3}\frac{J_{MPP}^2 n a^3 b^2 \rho_f}{h_f w_f} \qquad \text{Equation 1.8}$$

$$P_{LBus} = \frac{2}{3}\frac{J_{MPP}^2 a^2 n^3 b^3 \rho_f}{h_b w_b} \qquad \text{Equation 1.9}$$

J_{MPP} is the current density at the cells maximum power point, ρ_f is the resistivity of the finger material, h_f and h_b are the height of the finger and busbar, respectively. Similarly, w_f and w_b are the width of the finger and busbar, respectively. Considering the metallization grid, the non-design factor here is ρ_f, the resistivity of the finger material.

Here it is important to note that a distinction is made between resistivity and media resistivity. Resistivity, ρ, is an intrinsic property of a homogeneous material that describes electrical resistance (R) in relation to geometry of the resistor:

$$\rho = \frac{R \cdot A}{L} \qquad \text{Equation 1.10}$$

Here, A is the cross-sectional area of the resistor, and L is the current-carrying length of the resistor. Media resistivity, denoted ρ_m, describes the effective resistivity of a composite (a material containing more than one constituent) through effective media theory [34].

This distinction is made because metallization is rarely comprised of a single constituent material. Media resistivity treats the metallization as a composite made of a low resistivity material (such as pure Ag) and a high resistivity material (such as air

in pores). In effective media theory, electrical conduction percolates through a porous network and can be modeled as a function of porosity. The general effective media equation to describe the media resistivity of a composite material is [22]:

$$\rho_m = \rho_{low}(1 - \frac{f_{hig}}{f_{low}})^{-c} \qquad \text{Equation 1.11}$$

Resistivity of the low-resistivity phase is ρ_{low}, f_{high} is the volume fraction of the high resistivity phase, f_{low} is the volume fraction of the low resistivity phase, and c is the percolation exponent which is related to the morphology and distribution of the particles. Figure 4 shows an example of modeled resistivity of porous Ag as a function of porosity to demonstrate how dramatically the media resistivity changes with porosity. Here, ρ_m is

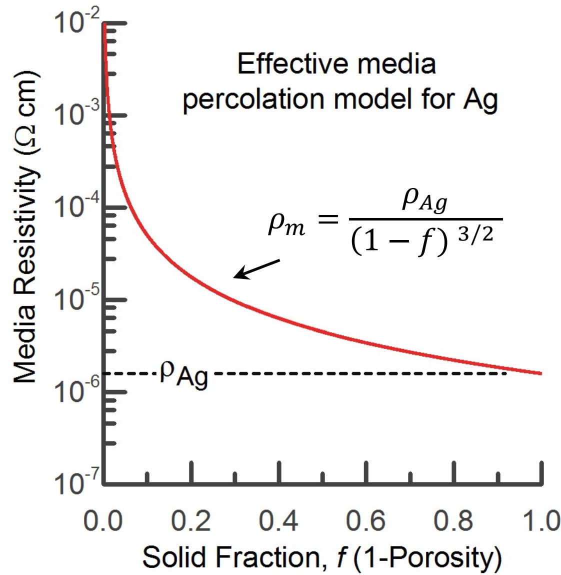

Figure 4. Effective media percolation model for resistivity of porous Ag as a function of porosity. Modeled following McLachlan's approximation for an asymmetric medium Ag host [23]. As f approaches 1, the media resistivity of porous Ag (solid red line) approaches the bulk resistivity of Ag (dashed black line).

the media resistivity of the porous Ag, ρ_{Ag} is the resistivity of pure bulk Ag; the equation displayed in Figure 4 describes the resistivity for an asymmetric conductor medium host, which means the conducting phase (Ag) completely wets and coats the insulating phase of

(pores) with a percolation exponent, c = 3/2 [22]. As the solid fraction (1-porosity) increases, the media resistivity approaches that of pure bulk Ag, as shown by the dashed line. At low solid fraction the media resistivity increases dramatically due to decreasing connectivity of conductive particles throughout the matrix [22].

So, metallization media resistivity—which is dependent on composition, porosity, and morphology—will influence the power losses of the front grid metallization. For metallizations that have lower porosity and less non-conductive constituents, both the resistive losses will be reduced (i.e. energy production will be higher), and the necessary amount of low-resistivity phase—such as Ag—will be lower (i.e. module production costs will be lower). To that end, throughout the remainder of this work ρ_m is evaluated for novel reactive ink metallizations and compared to industry standard and state-of-the-art metallizations.

1.2.2 ***Optical & Geometric Considerations***

Though front grid metallization is suitable for efficiently extracting current from the solar cell, it also shades (reflects or absorbs) some incoming light, preventing additional photogenerated current in the cell. Thus, there is a trade-off between power losses due to resistive losses, and shading. Power loss due to shading, $P_{LShading}$, from the front grid is described by:

$$P_{LShading} = nP_L\eta(aw_f + 2bw_b) \qquad \text{Equation 1.12}$$

Where P_L is the power density of the light incident on the cell, η is the energy conversion efficiency. Again, n is the number of fingers and a, w_f, b, and w_b are described in the previous chapter. For a given finger height (w_h), if finger width (w_f) increases, cross-sectional area will increase resulting in reduced resistive losses (see

Equation 1.10). However, as w_f increases, power losses from shading will increase. Therefore, metallizations with high aspect ratio (defined as w_f/w_h) increases current-carrying cross section while reducing shading. Shading losses can also be mitigated by modifying metallization geometry to reflect incident sunlight into the cell to reduce shading losses, and metallization could be thin enough to transmit some sunlight into the cell below. Metallizations that have minimal shading and resistive losses will have higher efficiency (i.e. energy production will be higher).

To that end, optical and geometric considerations will be a point of evaluation for novel reactive ink metallizations throughout the remainder of this work. Additionally, a brief synopsis of state of the art metallizations with advantageous geometries and optical properties will be given in Chapter 2.

1.2.3 ***Specific Contact Resistance & Adhesion***

Resistive losses occur not only in the front grid, but at the interface of the front grid metallization and the underlying cell. Power loss at the metal/cell interface, $P_{LContact}$, is described by:

$$P_{LContact} = 2J_{MPP}^2 nab^2\sqrt{\rho_c R_{sh}} \qquad \text{Equation 1.13}$$

Here, R_{sh} is the two-dimensional sheet resistance of the layer under the metallization that the current must travel through to reach the grid. Specific contact resistance, ρ_c, describes the electrical resistance across the metallization-underlying layer interface (with units of $\Omega \cdot cm^2$). First, ρ_c of a metal to a semiconductor is dependent on the potential barrier between the metal and semiconductor surface work functions. Second, ρ_c is dependent on the interfacial area that transports the majority of current across the interface, LT^2, where LT is the transfer length. Contact area between the metallization and the underlying layer

can be thought of analogously to the cross-sectional area of a resistor; Higher current-carrying cross-sectional area yields lower resistance (see Equation 1.10). The current-carrying cross-sectional area is generally limited by L_T. However, the actual area in physical contact can be smaller than L_T^2 if the metallization contains pores or voids or loses adhesion (denoted α) over time. Subsequently, like media resistivity (ρ_m), ρ_c is also tied to porosity and morphology. Similarly, if adhesion is poor, less metallization in physical contact with the underlying solar cell, resulting in less area to transport current through.

To that end, ρ_c and adhesion (α) of a novel reactive ink metallizations will be evaluated in Chapter 4. Furthermore, Chapter 4.2 details studies on surface modification of ITO (indium tin oxide, typically the top layer of SHJ cells) surface for improved α and ρ_c of reactive silver ink metallizations.

1.2.4 ***Performance Over Time***

The next phase is to address whether reactive ink metallized solar cells are 1) durable enough to withstand performance degradation throughout handling and the encapsulation process, and 2) durable enough to withstand undue performance degradation from environmental stress in the field. In this work, we study these stresses systematically, and sometimes make use of industry standard accelerated reliability tests. Understanding the long-term reliability and durability along with modes of failure are necessary to determine the industrial potential of reactive ink metallizations.

Finance of PV systems is dependent on perceived degradation risk over the warrantied lifetime of the system. Generally, PV systems are warranted for 20-30 years[9], [23]. Industry standard qualification test protocols, such as IEC 61215, were

developed in part to study the mechanisms identified to result in field failures [23]. Although these qualification test protocols are sufficient for lowering perceived risk for financiers and weeding out infant mortality of poorly-constructed PV modules, they are still far from being representative of actual degradation experienced by field-exposed modules. Even so, they provide a useful starting point for studying reliability in new materials like reactive ink metallizations.

The Damp Heat 1000 h IEC 61215 test (DH1000) is the most relevant of these test protocols relating to degradation of metallization over time. DH1000 consists exposing a module to 85 °C ± 2 °C under 85 % ± 5 % relative humidity for 1000 hours. This prolonged exposure to humidity under elevated temperatures assists moisture ingress into the module, promoting delamination and corrosion of metallization.

Performance and degradation of cells with reactive ink metallizations, and commercially available screen-printed Ag pastes throughout encapsulation and DH1000 is reported in Chapter 5. A detailed study on corrosion of Ag-based metallizations, including reactive silver inks, is presented in Chapter 5.3.

1.2.5 ***Summary***

It follows that there are four primary factors that govern power losses from the front grid. First, the media resistivity, ρ_m, of the metallization along with geometric factors (i.e. grid length, width, height) govern the total power lost from grid resistance. Second, optical and geometric factors are responsible for power losses from shading by the grid. Third, the resistance between the grid and the underlying layer (for example an emitter or transparent conducting oxide) is dependent on interfacial specific contact resistance, ρ_c, and can change throughout time with loss of adhesion. Fourth, performance and degradation of the front

grid throughout exposure to environmental stresses such as high relative humidity at elevated temperatures promotes corrosion of metallization. Minimizing power losses focuses on simultaneously balancing and optimizing these factors. This work focuses on addressing these four primary factors that contribute to power losses from the front grid and evaluate novel reactive ink metallizations in terms of these losses. Before detailing this work, the following chapter will describe the current industry standard and state of the art metallizations, and challenges in terms of these power losses.

2. CONVENTIONAL & STATE-OF-THE-ART METALLIZATIONS

Metallization of solar cells requires both a metallization material (what the front grid will be made of), and a deposition method (how the front grid material will be deposited on the solar cell). Today, screen-printed Ag paste, referred to as SP Ag paste from this point forward, is the industry standard metallization method for Si solar cells. Benefits of this method include high throughput, relatively low-cost equipment with simple process operation [24]. However, Ag usage is high with SP Ag paste metallizations and finger geometries are limited by this conventional method [25].

As described in Chapter 1, reductions of Ag consumption are necessary to sustain current PV growth trajectories, and to reduce impact on total module manufacturing cost [15]. Chapters 2.1-2.6 describe conventional and state-of-the-art metallization methods, along with their advantages and challenges to widespread replacement of SP Ag paste metallization in the PV industry.

2.1 Screen-Printing of Silver Pastes

Screen-printing of Ag paste is the conventional metallization for Si solar cell manufacturing. The screen-printing process is depicted in Figure 5 [26]. The process goes as follows: First, a fine-mesh screen in stretched tightly and secured in a rigid frame. The screen is then patterned with a photosensitive emulsion using photolithography. The patterned screen consists of emulsion covering only designated regions of the screen. Emulsion-covered regions block paste from going through the openings in the mesh, and exposed regions of the mesh allow for paste to be deposited onto the solar cell (i.e. the exposed mesh opening pattern defines the front grid pattern). Next, the framed screen is clamped into a screen-printing machine, which minimally consists of a screen holder,

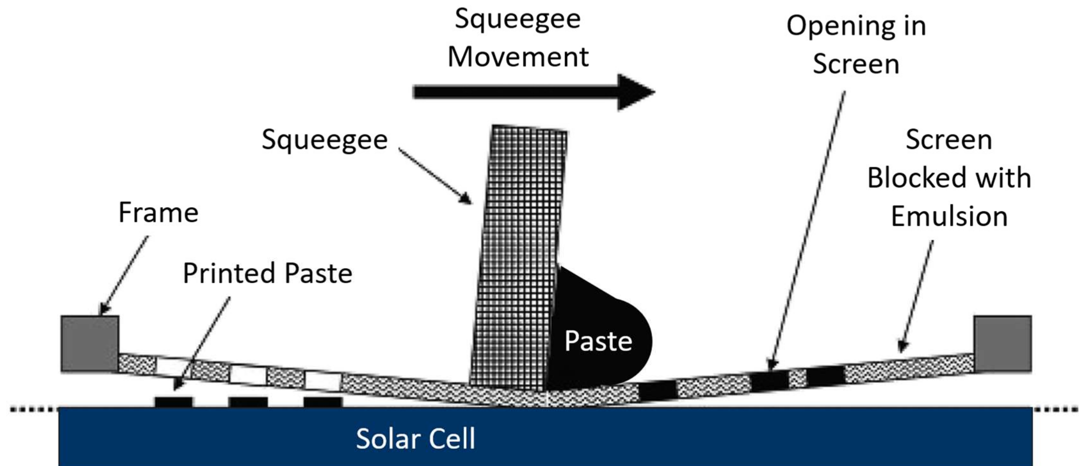

Figure 5. Schematic showing the process of screen printing paste onto a solar cell. Schematic was modified from an original figure by Aleeva and Pignataro [27].

substrate holder, and a squeegee. Metallization paste (typically Ag paste) is applied across the width of the patterned region on top of the screen. Then, a squeegee moves the paste across the entire length of the pattern, flooding paste into openings in the patterned screen. The squeegee then moves back to its initial starting position. A solar cell is placed directly under the screen, and the screen is moved into close proximity of the top surface of the solar cell. Finally, the squeegee presses down on the screen while moving the entire length of the patterned region. The squeegee stretches the screen slightly, pressing the screen into contact with the solar cell surface, depositing paste where the openings are in the screen. Following this process, the paste is dried and cured/fired in a furnace following the paste manufacturers specifications.

Again, the main advantages of SP Ag paste metallization is that the process is relatively simple and robust, has high throughput speeds (>50 mm/s), and has been the primary method used in PV manufacturing for nearly half a century [27]. State-of-the-art screen-printing techniques use screens with 30 µm mesh openings, forming fingers around 46 µm wide, have throughput speeds of over 100 mm/s, and a minimum Ag-

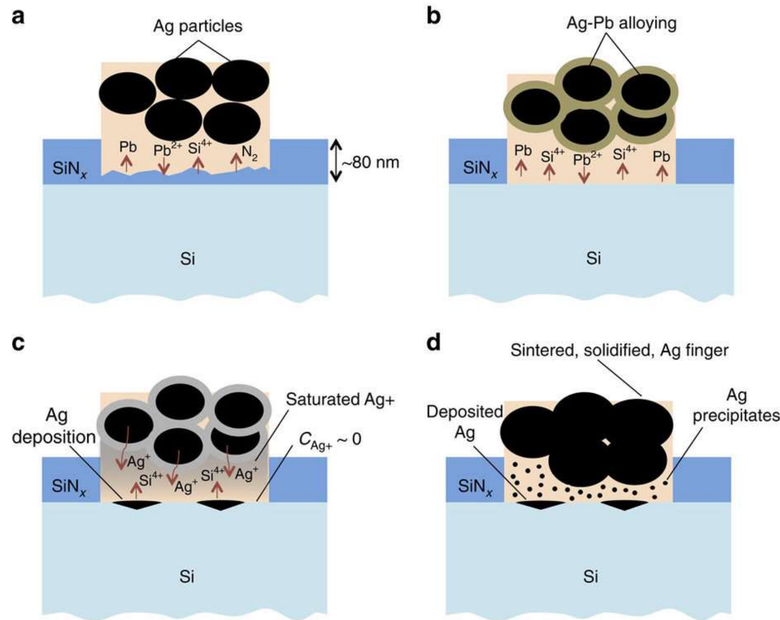

Figure 6. Schematic of high-temperature glass frit Ag paste firing through a SiNx layer on Si. (a) Shows the etching through the SiNx by the PbO in the frit, (b) shows Ag–Pb alloying, (c) shows Ag moving through molten frit and deposition at the Si interface, and (d) shows the final fired-finger morphology, with a sintered Ag particle network in glass. Schematic taken from Fields *et al.* [30].

consumption of 67.7 mg Ag/cell [25], [28]. Still, there is noteworthy room for improvement using SP Ag pastes.

First, further reducing Ag usage is a crucial area for improvement. Historically, the price of Ag has been quite volatile and expensive; for example in 2002 the price of Ag was approximately $5 /troy oz. before nearly quadrupling to $39 /troy oz. in 2011 [15]. For this reason, solar cell manufacturers have already been targeting and achieving reductions in the amount of Ag used in solar cell manufacturing [8], [28]. The International Technology Roadmap for Photovoltaics (ITRPV) describes this trend and projected further reductions in Ag usage; in 2016 c-Si solar cells typically used just above 100 mg Ag/cell, usage is projected to decrease to about 40 mg/cell [8]. This is not only necessary to reduce dependence on a volatile costly commodity; world reserves of Ag supplies could be a limiting material constraint to terawatt levels of PV production unless Ag content is

Third, ITRPV also projects a trend towards thinner wafers in the upcoming decade [8]. This trend towards thinner wafers would encourage a more delicate, non-impact metallization deposition method to minimize breakage of fragile thin wafers to increase yield. At present, wafer thicknesses below 150 μm have higher risk of breakage during cell fabrication [8].

Finally, SP Ag paste metallizations must be tailored to meet requirements for each type of device architecture. As described in Chapter 1, diffused junction c-Si cells generally used a high-temperature screen-printed Ag paste that is fired at temperatures in excess of 700 °C. This high temperature is necessary to sinter the Ag particles together, fire through the nitride layer, and make ohmic contact to the emitter (see Figure 6) [29].

Furthermore, as the market share of SHJ is expected in increase over the next decade, this requires metallization processed under approximately 200 °C [30], [31]. SHJ cells require metallizations that do not need to be heated to temperatures above ~200 °C in order to preserve the passivation provided by hydrogenated intrinsic amorphous Si [30]. Presently SHJ cells are not widely mass-produced, still several specialized low-temperature screen-printed Ag pastes have been commercially produced for such application. The two types of pastes that are used for SHJ cells are thermoplastic and thermoset pastes [30]. These low-temperature pastes still require temperatures near 200 °C to cross-link conductive polymers to form a continuous conductive chain for thermoset pastes, and to evaporate conductivity-limiting solvents for both thermoset and thermoplastic pastes [30]. Since these low-temperature pastes are heavily loaded with polymers, large amounts of Ag must be used to decrease the media resistivity of the paste (see Equation 1.11). An estimated 200 mg of Ag/cell is used for a SHJ cell with low-

temperature Ag paste compared to about 100 mg/cell for a c-Si with high-temperature Ag paste [7], [30]. This means double the amount of Ag is used in the low-temperature pastes while still resulting in higher media resistivity.

Despite these challenges, screen-printing of Ag pastes is expected to remain the dominant metallization technology for the coming decades [8]. Opportunities for improvement of SP Ag paste include the use of knotless screens (screens with only parallel wires in one direction) for homogeneous finger geometry and narrower finger widths, improvements in paste formulation to reduce screen clogging and finger width spreading, and print-on-print methodology [28], [32], [33]. Still, other metallization methods are expected to gain market share year after year as improvements to new technologies are made [8]. The following chapters detail some of these approaches to improve metallization of solar cells.

2.2 Stencil Printing

Stencil printing is similar to screen-printing, where a paste is applied to a thin stainless steel foil patterned chemically or with a laser to form openings down to 15 µm wide [30]. Ag paste is typically squeegeed across the patterned foil, depositing paste onto the solar cell surface. After the paste is dried, another layer may be printed on top of the first layer –this is called double-printing. Double-printing improves finger aspect ratio but requires high-precision alignment to print directly on top of the first layer, which remains a challenge for low-cost industrial practices.

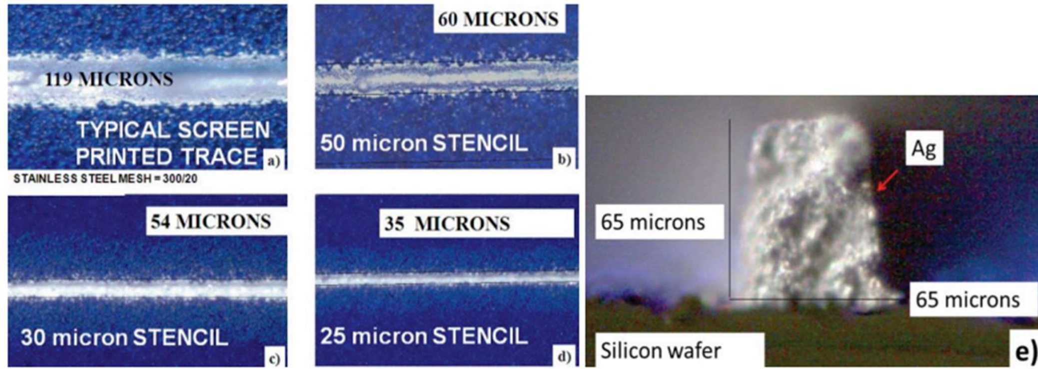

Figure 7. Examples of fingers printed with low-temperature Ag paste by screen-printing (a), and stencil printing (b-e). The cross-sectional image in e) shows the high aspect ratio that is achieved using double-print stencil printing. Figure taken from De Wolfe *et al.* [31].

Figure 7 shows examples of fingers printed from stencil printing compared to screen-printing, including a high aspect ratio finger from double-print stencil printing [30]. The benefits of stencil printing include realization of narrower, taller fingers (if double-printing with micron-scale alignment is used) compared to screen-printing [30]. Still, stencil printing is a contact deposition method that involves pressure applied on the wafer potentially breaking the stencil, or the wafer similarly to the screen-printing challenges described in Chapter 2.1

2.3 Copper Pastes

The path toward reducing Ag usage relies on reducing Ag content of the metallization while maintaining or improving media resistivity. Ag has the lowest resistivity (1.59 μΩ·cm) of all metals and therefore has the greatest potential to minimize power losses related to metallization compared to other materials. However, Cu has relatively low resistivity of 1.68 μΩ·cm and is considerably less expensive than Ag, with 2017 price of $6.3 /kg USD compared to $550 /kg for Ag [34]. Low-temperature (< 200 °C) screen-printed Cu pastes have demonstrated resistivities of 100 μΩ·cm, which still is high compared to resistivity of state-of-the-art low-temperature Ag paste (~5 μΩ·cm) and high-

temperature Ag paste (~4 μΩ·cm) [15], [35], [36]. An additional challenge for Cu metallizations is that Cu is chemically less inert than Ag, and often forms copper oxide under ambient atmospheres and at elevated temperatures [37].

2.4 Metal Plating

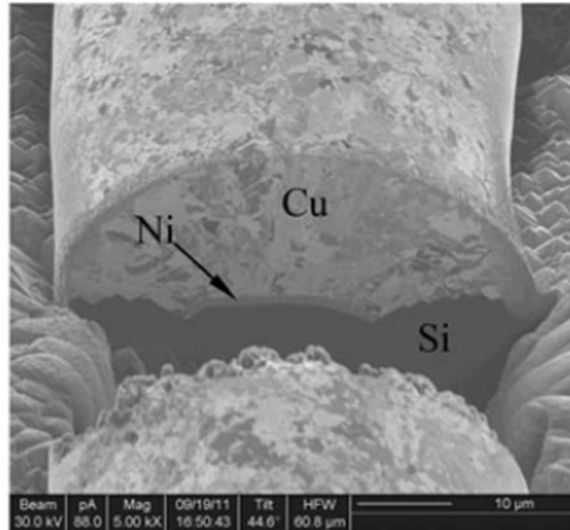

Figure 8. Scanning electron microscope image of a cross-sectional view of a Ni-Cu finger plated by light induced plating, with finger width less than 50 μm, and height of 16-18 μm. Figure taken from Lennon *et al*. [39].

Metal plating is the envisioned substitute for screen-printed Ag paste in PV manufacturing in the coming years [8]. Benefits of metal plating are the realization of high-aspect ratio fingers with low metal usage (see example of plated Cu finger in Figure 8) [38]. Plating requires an initial high-precision process to pattern a masking layer [38]. The most commonly used techniques for selective patterning of solar cell technologies are photolithography, laser processing, soft lithography, screen-printing, aerosol printing, and inkjet printing, these patterning processes often require micron-scale alignment from one step to the next [38], [39]. Each of these existing patterning techniques has limitations in achieving high quality results while also having low capital expenditure and waste, industrial scalability, and process simplicity.

Metal plating can be done by electroplating, electroless plating, or light induced plating; each method has its own advantages and disadvantages. Common plated materials include Ag, Ni and Cu for photovoltaic applications. Electroplating requires physical contact to supply a source of electrons for plating. This results in relatively fast plating rates, however it requires more complex wafer handling equipment [38]. Light induced plating relies on the light-induced current from a solar cell to provide a source of electrons. In electroless plating, a reducing agent in a solution of metal ions provides the source of electrons for the metal reduction process. Concentration of the reducing agent the needs to be continuously monitored, controlled, and replaced, resulting in added waste management costs. Moreover, plating rates for electroless plating are generally much slower than electroplating processes.

Currently, some remaining obstacles for plated metallizations for solar cells include improving adhesion, and demonstrating long-term reliability [38]. Additionally, a substantial challenge remains in proving that plated metallizations' value propositions (cost reductions, efficiency gains, and throughput) are high enough to replace already running and process-proven screen-printers with plating equipment. Furthermore, electroplating results in a large quantity of waste that contains toxic and hazardous chemicals, and use of large amounts of fresh water [40].

2.5 Dispense Printing of Particle-Based Inks & Pastes

Dispense printing has the potential to be a low-cost, industrially scalable, non-contact, high-precision, and maskless deposition method capable of reducing material waste [41]. The printing process involves dispensing a fixed quantity of a liquid ink or paste from a reservoir through a nozzle [41]. There are various types of dispense printers, such as drop-

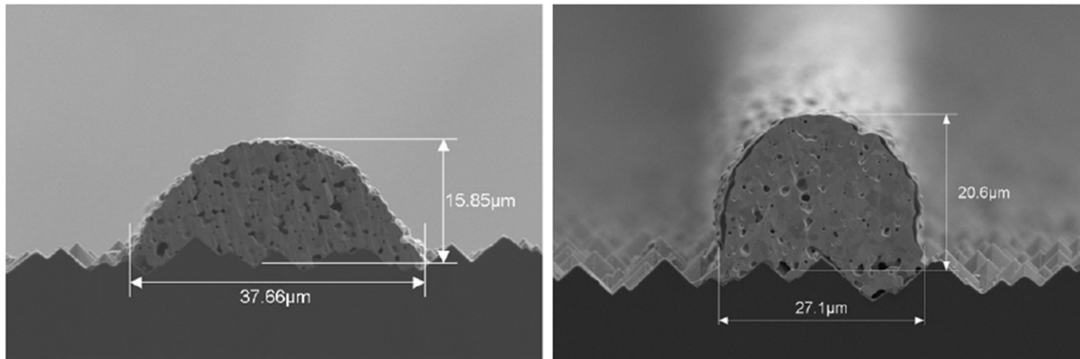

Figure 9. SEM images of a screen-printed paste finger, dispense printed with 40 µm nozzle (left), and a narrower, high aspect ratio modified paste, dispense printed finger with a 40 µm nozzle diameter (right). Figure taken from Pospichil *et al*. [34].

on-demand printers which dispense a single drop at a time, or stream dispense printers which eject a continuous stream of fluid. In 2015, Pospischil *et al*. reported on the realization of dispense printing platform that is competitive with screen-printing in solar cell manufacturing [33]. They demonstrated several advantages of dispense printing over screen-printing; i) processing speeds of over 700 mm/s, which is competitive with state-of-the-art screen-printers; ii) nearly 50% reduction in shading losses due to minimized spreading of paste (see Figure 9); iii) 20 % less Ag consumption due to high homogeneity of finger geometries; (iv) an increase in absolute efficiency of 0.4 % [33].

Dispense printing, though promising, still has some challenges. The most commonly used inks for dispense printing of metallization are nano-particle based metallic inks. Particle-based inks have relatively low metal loading content, and also contain organic additives [42], [43]. These organic additives have several functions; first, to provide a liquid phase solution for dispense printing; second, to coat metallic particles with a capping agent to keep them from clustering and clogging nozzles; and third, to improve mechanical properties of the printed metallization with enhancing

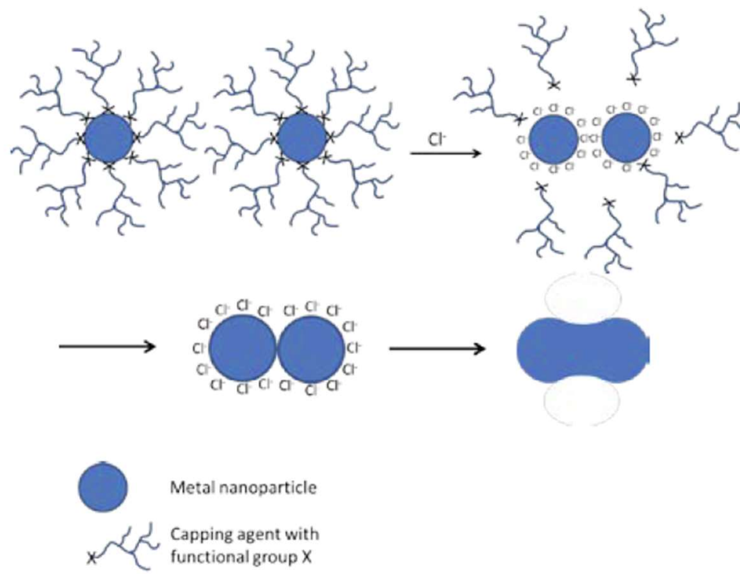

Figure 10. Schematic of chemical sintering process of metal nanoparticles with a capping agent, taken from Glunz *et al*. [45].

agents (binding and adhesion) [41], [42]. Once printed, some of these organic additives need to be removed in order to allow metallic particles to physically contact each other to create a conductive network (see example of capping agent removal in Figure 10) [44]. Heat typically above 200 °C is applied to remove solvents, partially remove the capping agent to create physical contact between adjacent metallic particles, then to sinter those metallic particles together, and finally to cure any mechanical property enhancing agents [42], [45]. Consequently, media resistivities of these particle-based inks are higher than bulk metal resistivity because they contain additives. Achieving low media resistivities is especially challenging if the inks cannot be processed at temperatures over 200 °C to thermally sinter conductive particles together, as in the case for SHJ metallization [30].

Printed feature size (i.e. finger width, w_f) is limited in part by the diameter of the printer nozzle. Particle-based inks must have small particles to avoid clogging nozzles. Even with capping agents, particle sizes can only be minimized to an extent before nozzles will clog. A general rule is that the nozzle diameter must be greater than 7× the particle diameter to

avoid clogging [25]. Thus, smaller nozzle diameters are employed to produce narrower fingers, and particle size must also decrease to avoid clogging. Furthermore, as particle size becomes smaller to accommodate smaller nozzles, the price of the particles increases because special processes are needed to produce nanoparticles compared to microparticles [46].

The remaining challenges for dispense printing of metallization lies in the formulation of the ink or paste, and printing parameters to produce features with desired geometric and electrical properties. Chapters 2.6- 3.2 describe in more detail how ink properties and printing parameters can influence geometric and electrical properties of dispense printed metallizations.

2.6 Dispense Printing of Reactive Inks

The main focus of this work is to evaluate potential of a new metallization technique, dispense printing of reactive inks, to become a high efficiency replacement for solar cell metallization. The previous chapter described the advantages and challenges of dispense printing as a deposition method. Advantages include being a non-contact deposition method, which means there is lower risk of wafer breakage compared to contact methods such as screen-printing and stencil printing, especially for thinner wafers. Additionally, dispense printing offers a low-cost, high performance alternative to traditional methods used in the manufacturing and processing of silicon solar cell technologies [33]. The main challenge remaining for dispense printing of metallization is ink formulation in combination with printing parameters to form metallization with the desired geometry and electrical properties.

This work aims to address the above challenges while also advancing applications and understanding of a novel metallization material: reactive inks. First in this chapter, I introduce reactive inks, and compare them to conventional particle-based inks. Next, I describe the unique sensitivity of reactive inks to processing parameters. Lastly, I give a summary of the state-of-the-art in reactive ink metallizations as reported by others before presenting my own work on dispense printed reactive ink metallizations for photovoltaics in Chapters 3-5.

2.6.1 ***Introduction to Reactive Inks***

Reactive inks have potential to be a low-cost, high performance alternative to conventional, particle-based inks like the ones mentioned in Chapter 2.5. Particle-based inks print clusters of conductive particles. Reactive inks, on the other hand, print chemical reactions that can produce solid metals at mild temperatures. This reaction can be initiated either by elevated temperature (thermally), solvent or stabilizing agent evaporation (chemically), by some increased catalytic activity of the substrate (kinetically), or a combination of the three [43], [47]–[49].

Figure 11 shows a comparison of ink compositions and resulting metallizations for a reactive ink and particle-based ink. Particle-based inks consist of conductive particles (shown as grey circles) suspended in solvents and additives (such as glass-frit or binders, for example, represented by red circles). Reactive inks are particle-free liquids containing metal ions (M^+) and reducing agents (R^-). They are the precursors to a reduction-precipitation reaction that has solid metal as the product. Once printed the reaction begins to reduce and precipitate solid metal (represented by grey circles). Reactive inks can be formed at mild temperatures, with sintering between particles occurring primarily

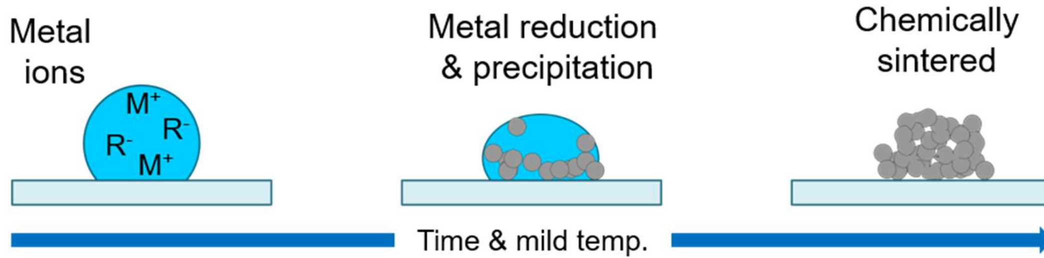

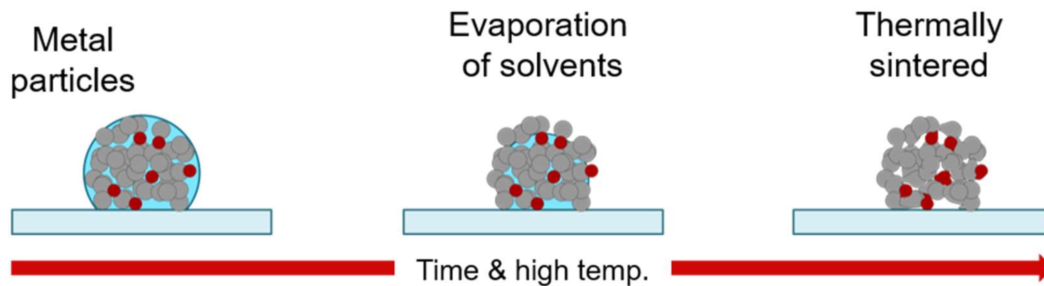

Figure 11. Particle-based inks and pastes consist of conductive particles (grey circles) suspended in solvents and ink/paste modifiers (such as glass-frit or binders, represented by red circles). Reactive inks are particle-free precursors to a chemical reaction that once printed begin to reduce metal ions (M^+) and precipitate solid metal (represented by grey circles). Reactive inks can be formed at mild temperatures with chemical sintering, whereas particle-based inks require high temperatures to thermally sinter conductive particles.

chemically, whereas particle-based inks often require high temperatures (> 200 °C), and sintering is primarily thermal [42], [43].

For particle-based inks and pastes, too large of a particle size will cause nozzles or screens to clog, which limits the minimum mesh and nozzle diameter (see Chapters 2.1 and 2.5). Again, as a general rule, nozzle diameter must be more than 7× the particle size to prevent clogging [25]. The particle-free nature of reactive inks expands the opportunity to further reduce finger widths by using nozzle diameters significantly smaller than those used for particle-based inks.

The base reactive silver ink (RSI) presented in the majority of this work is formed following a modified Tollens' process, as described in full detail by Walker and Lewis [45]. The RSI presented in this work is also typically prepared with ethanol, a high vapor pressure solvent, to alter the viscosity of the ink for dispense printing. The main constituents of the initial ink solution, the reactive silver ink, and the printed feature are shown below [45]:

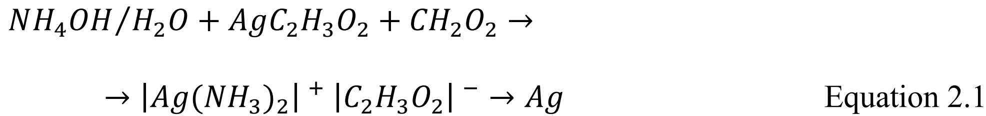

$$NH_4OH/H_2O + AgC_2H_3O_2 + CH_2O_2 \rightarrow$$

$$\rightarrow |Ag(NH_3)_2|^+ \, |C_2H_3O_2|^- \rightarrow Ag \qquad \text{Equation 2.1}$$

The initial solution (reactants in Equation 2.1) consists of aqueous ammonium hydroxide, silver acetate, and formic acid. The reactive silver ink (intermediate products in Equation 2.1), which contains diamine silver cations, acetate and formate anions, is stable at room temperature as long as there is excess ammonia in the solution. Once the reactive silver ink is printed, the excess ammonia evaporates and drives the reaction forward, reducing the silver diamine to silver and residual acetate. Upon a mild temperature treatment of 90 °C, Walker and Lewis reported resistivity identical to that of pure Ag (final product in Equation 2.1) [45].

If properly designed, reactive inks produce highly pure metal at mild temperatures. However, the "reactive" nature of reactive inks presents a unique challenge; Final morphology and composition of the metallization relies on kinetics of a chemical reaction. Therefore, reactive ink metallizations are markedly sensitive to process variations. Figure 12 schematically illustrates the complexity of reactive ink systems where, due to differences in evaporation, heat transfer, reaction rate, and fluid flow, the resulting metallization will vary. Here, a distinction is made between the reactive ink and the

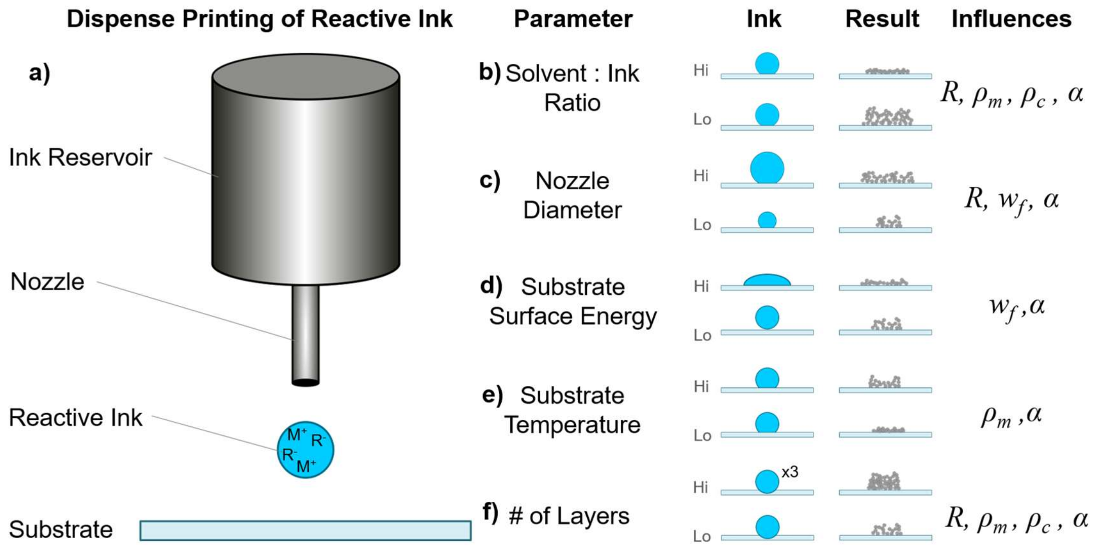

Figure 12. (a) Schematic of dispense printing of reactive ink. (b-f) Parameters that influence the resulting metallization properties, along with the properties that are most heavily influenced by changes in the corresponding parameter. R denotes resistance, ρ_m is media resistivity, ρ_c is specific contact resistance, and α is adhesion.

resulting metallization because of this dependence on factors that influence the ink's reaction to form the metallization.

For clarity, Figure 12 (a) shows a schematic of dispense printing of reactive inks. The reactive ink is prepared and placed in the ink reservoir. The ink is initially composed of metal ions and reducing agents (M^+ and R^-, respectively). The ink is dispensed from the ink reservoir, through a nozzle. The dispense printing systems used in this work are equipped with a heated platen to secure and heat the substrate during printing.

Figure 12 (b-f) also shows some of the major parameters that influence the ink's reaction and therefore the resulting metallization. For each of these major parameters, this schematic shows a comparison of the ink and resulting metallization and lists the metallization characteristics that are largely influenced.

As mentioned above, the RSI in this work is typically prepared with ethanol to adjust the viscosity of the ink for printing. Solvent type and solvent:ink ratio also significantly influence wettability, evaporation rate, and coffee-ring effect of the printed ink [50], [51]. Inks with a higher solvent:ink ratio are more diluted. That is, they have lower metal and reductant ion concentrations, and a relatively slower reaction rate [47]. So, a low solvent:ink ratio ink will react relatively quickly, nucleating and aggregating larger metal clusters that entrap volatile solvents and forming large pores. Accordingly, solvent:ink ratio influences morphology of the resulting metallization, largely influencing media resistivity (ρ_m), specific contact resistance (ρ_c), and adhesion (α) (see Figure 12 (b)).

Nozzle diameter is another parameter that influences the final metallization characteristics. The diameter affects the amount and distribution of ink that is dispensed (Figure 12 (c)). Therefore, nozzle diameter influences metallization resistance (R), and feature width, or finger width (w_f). Notably, adhesion (α) is also influenced by nozzle diameter and will be discussed in more detail in Chapter 4.1.

The substrate on which the ink is printed is similarly important in the resulting metallization characteristics. While the ink is contained in the reservoir, the ink is a particle-free liquid. Once printed, the ink will begin to react, and the ink will conform to the substrate on which it was printed depending on the ink composition and substrate surface energy. The ink and substrate surface energy dictate wettability of the ink too, significantly influencing w_f (see Figure 12 (d)). Furthermore, substrate surface energy and surface termination can be modified to improve adhesion (α) [50]–[52]. This subject—specifically surface modification of ITO—will be discussed in more detail in Chapter 4.2.

Moreover, substrate temperature governs reaction and evaporation rates which influences ρ_m, α, particle nucleation, aggregation, and morphology (see Figure 12 (e)).

Lastly, metallization resistance can be decreased by printing more layers on top of the initial layer, increasing the current-carrying cross-sectional area. However, resistance does not necessarily scale linearly with number of layers; Reactive ink metallizations are porous, so each additional layer that is printed on top can flow into the pores, changing the porosity and ρ_m. Furthermore, depending on other parameters—namely solvent type, solvent:ink ratio, and substrate temperature— ρ_c and α can be influenced by the number of layers printed. If a metal film forms on the top surface of the metallization, solvents can be trapped below the solid surface. The volatilization of trapped solvents builds up pressure under the solid metal surface until the surface ruptures. These phenomena can result in large pores, and decreased adhesion, and will be discussed in more detail in Chapter 4.1.

Much of the work presented in Chapters 3-5 aims to improve understanding of how these parameters influence the reactive ink metallization characteristics, with a focus on improving ρ_c , ρ_m , w_f, and α for low series resistance solar cell metallization. The next chapter will describe current state-of-the-art reactive inks that have been developed by others for general use as conductive inks.

2.6.2 State-of-the-Art Reactive Inks

While the concept of printing conductive lines from chemical precursors or reactions is not new, recent advances in the chemistries of conductive reactive inks have dramatically reduced the reaction temperatures to below 150 °C, and even down to room temperature with recent improvements in electrical properties [10], [11]. To

date, Walker and Lewis' reactive silver ink (RSI) demonstrates the best electrical properties, with resistivity identical to bulk silver with annealing at 90 °C in air [43]. In 2012, Walker and Lewis first reported on synthesis of this RSI using a modified Tollens' process [43]. Their formulation uses silver acetate, formic acid and ammonium hydroxide, which improves upon the original Tollens' process in several ways; First, the use of silver acetate, rather than silver nitrate, results in an ink that is stable and non-explosive; Second, the use of formic acid leaves only water and carbon dioxide as residuals. Because of the excellent electrical properties and potential advantages of the particle-free nature of the ink, the majority of the work presented in Chapters 3-5 employs Walker and Lewis' RSI as the base ink for solar cell metallizations.

Even though Walker and Lewis' RSI has advantageous electrical properties, Ag usage in solar cells is expected to be substantially reduced, or eliminated entirely in the coming decades [8], [30], [43]. Cu is the envisioned replacement for Ag solar cell metallizations due to its comparable resistivity and substantially lower price (see Table I).

To date, several reactive Cu inks have been developed, but none have demonstrated properties competitive with Ag-based metallizations for solar cells [37], [48], [49]. At this time, the best performing Cu reactive inks have been developed by Farraj *et al.*, and Shin *et al.* [37], [49].

Farraj's Cu reactive ink is formulated from copper formate and 2-amino-2-methyl-1-propanol, which decomposes under nitrogen atmosphere at 140 °C, with a resulting ρ_m of 10.5 μΩ·cm [37]. Also using a Cu reactive ink formulated with copper formate and 2-amino-2-methyl-1-propanol, an even lower ρ_m of 9.5 μΩ·cm has been demonstrated by Shin *et al*. However this was only achieved through annealing at 350 °C under a nitrogen

atmosphere [49]. Cu is chemically less inert than Ag, adding to the challenges for Cu reactive inks, as they currently suffer from easy oxidation to form copper oxide under ambient atmospheres. As exemplified in Table I, current state-of-the-art Cu reactive ink properties still have room for improvement to become an industrially viable replacement for Ag-based metallizations for solar cells.

Still, although the majority of this work utilizes Walker and Lewis' reactive silver ink (RSI), evaluation of other reactive inks for use as solar cell metallization can benefit from the work presented here. We propose dispense printing of RSI as an advanced metallization method for solar cells, offering the potential to reduce LCOE for solar photovoltaics.

Table 1. Comparison of silver and copper properties.

Properties	**Silver**	**Copper**
Bulk ρ	1.6 μΩ·cm	1.7 μΩ·cm
Price per kg in USD *	$ 489.00	$ 5.91
State-of-the-art reactive ink ρ_m **	1.6 μΩ·cm	9.5 μΩ·cm
Reactive ink processing temperature **	90 °C	350 °C
Reactive ink processing atmosphere **	air	nitrogen

* Metal spot price on January 21, 2019 from [53].
**Reactive silver and copper ink information from [43], [49]

3. REACTIVE SILVER INK METALLIZATION PROPERTIES

The major goal of this work is to evaluate potential of a novel metallization technique –dispense printing of reactive inks –to become a high efficiency replacement for solar cell metallization. Specifically, this work uses reactive silver inks (RSI) as a prototype, which can be extended to other reactive inks. The characteristics used to evaluate the potential of this novel metallization method are:

1. Media resistivity, ρ_m (Chapter 1.2.1)
2. Optical & geometric properties, such as w_f (Chapter 1.2.2)
3. Specific contact resistance, ρ_c (Chapter 1.2.3)
4. Adhesion, α (Chapter 1.2.3)
5. Performance over time (Chapter 1.2.4)

Before detailed evaluation of the above characteristics, Chapter 3.1 describes a proof-of-concept study using RSI as front grid metallization for SHJ cells. This study shows the basic properties of RSI before complete optimization and motivates the remainder of this work. Following the proof-of-concept study, Chapter 3.2 describes characterization of RSI optical properties and ρ_m for varying deposition parameters (see Figure 12 for examples of parameters). These characteristics are described in relation to the porous structure of RSI, as well as how to characterize porous structures. Chapter 4 details electrical characterization of the ITO/RSI interface (ρ_c and α), including a study on a potential adhesion promoting layer for RSI to ITO surfaces. Chapter 5 outlines and compares device performance and degradation for SHJ cells made with RSI, and SP Ag Paste front grid metallizations.

3.1 Proof-of-Concept for Dispense Printed Reactive Inks for Solar Cell Front Metallization

The first work in this project is a proof-of-concept study for RSI front grid metallization deposited by Drop-on-Demand (DoD) printing. RSI was synthesized according to the process developed by Walker and Lewis [45]. DoD printing was used to attempt to print high-precision, narrow features to minimize power losses from shading. The promising first results of this study show that RSI metallization deposited by DoD printing resulted in low resistivity (2-5 μΩ·cm) metallization at mild temperatures of 78 °C. Solar cells with a front grid formed from DoD RSI performed comparably to cells prepared with its screen-printed counterpart. The main findings of the article are provided below to illustrate these results, as well as frame the motivation for the rest of this work [54]. The full article can be found published elsewhere [54].

*3.1.1 **Drop-on-Demand Reactive Silver Inks for Solar Cell Front-Grid Metallization: Proof of Concept***

High temperatures are often required to form low resistivity Ohmic contact. High temperatures are applied to evaporate conductivity-limiting organic residues in conductive pastes or to sinter conductive particles [42], [45]. Unfortunately, such high temperatures are not compatible with next generation photovoltaics such as SHJ devices [42], [45], [55], [56]. This work aims to demonstrates high-conductivity metallization formed at mild temperatures to broaden device application opportunities to include thermally-sensitive substrates and electronically-active layers.

Reactive metallic inks—such as nickel, copper, and silver—enable dispense printing of highly conductive features at low temperatures (typically 35–120 °C)

without the need of a post-deposition anneal [45], [57], [47]. Here, RSI films were formed from silver acetate, formic acid, and ammonia following a modified Tollens' process, described in detail by Walker and Lewis [45]. The printing process from this RSI results in the reduction and precipitation of Ag, and residual acetate groups [54]. During printing, the substrate (or solar cell) is maintained at mild temperatures below 100 °C to volatilize the organic residues. The resulting in RSI films exhibits composition and resistivity nearly equivalent to that of pure Ag [45], [47].

Again, solar cell metallization requires patterning of micron-size features for optimal device performance, which can advantageously be addressed by DoD RSI printing. This technique facilitates high-precision patterning of fine features without the need of additional masking steps, while also minimizing waste of precious metals in inks and pastes [18]. Here, we present the main results for a proof-of-concept investigate RSI metallization deposited by DoD printing as front grid metallization of solar cells, which to our knowledge, is reported for the first time in our publication [54].

Again, at this time, the highest efficiency for non-concentrated Si solar cells is held by amorphous Si (a-Si)/crystalline Si (c-Si) heterojunction (SHJ) cells with a reported efficiency of 25.6% for standard reference spectra (ASTM G173) [55]. However, a limitation of SHJ cell performance is the considerably high series resistance (R_s) that primarily results from the relatively high-resistivity, low-temperature Ag paste that is used for front grid metallization (see Chapter 2.1). Although low ρ_m of ~ 5 μΩ·cm have been recently reported for state-of-the-art curing processes using screen-printed Ag pastes, there is still notable room for improvement [36].

While diffused-junction Si solar cells can use high temperature annealing to form low resistance metallization from Ag pastes, SHJ cells are substantially more thermally sensitive, as the surface passivation—typically provided by hydrogenated amorphous silicon (a-Si:H)—begins to degrade at temperatures above ~200 °C [31]. Thus, a major challenge for achieving higher efficiency SHJ cells is in minimizing R_s by reducing the metallization ρ_m and ρ_c. This proposed combination of this advanced printing technique with RSI offers opportunities to benefit SHJ performance through (i) formation of highly conductive metallization grids to reduce R_s, (ii) processing at mild temperatures to avoid degradation of passivation layers, and (iii) reduced front grid w_f to minimize shadowing effects and enhance current generation. Moreover, these benefits are not limited to SHJ solar cells only, other thermally sensitive devices such as organic photovoltaics could improve performance using RSI metallization [58].

The work presented here introduces and examines DoD printing of RSI (DoD RSI) as an alternative front grid metallization method for SHJ cells. First, electrical and optical properties of DoD RSI films are characterized and compared to those of commercially-available screen-printed Ag paste ("SP paste") films. Next, w_f, finger aspect ratio, and substrate surface morphology are discussed. Then, the impact of front grid metallization method on SHJ solar cell current-voltage characteristics is analyzed, with emphasis on the contributions to series resistance. Overall, we demonstrate similar device performance for the SP paste and DoD RSI SHJ cell. Finally, we summarize a path towards optimization of the RSI metallization process in order to exceed performance of SP paste metallization.

The base ink was prepared following Walker and Lewis' recipe [45]. The RSI was then diluted 1:1 by volume with ethanol (EtOH, C_2H_6O, ACS reagent grade, Sigma Aldrich). RSI metallization was printed in an ambient atmosphere on a Microfab Jetlab II inkjet printing system with a 60-µm-wide nozzle [47]. All RSI metallizations in Chapter 3.1.1 were printed 5-layers-thick. SP paste grids were printed with an Applied Materials Baccini screen-printer using a low-cure-temperature Ag paste from Namics Corporation.

RSI was characterized by four-point probe, spectrophotometry, and optical mocroscope imaging. The RSI pads were printed at 51, 78 and 107 °C. The SP paste contact pads were printed at room temperature, followed by annealing in a muffle furnace in ambient atmosphere for 20 min. at 200 °C.

SHJ solar cell samples were fabricated, front grids were prepared on half of the samples by screen-printing a low-cure-temperature Ag paste (SP paste). Next, all samples were annealed in air at 200 °C for 20 min. in order to recover damage incurred during ITO sputtering deposition [59], in addition to curing the SP paste. Finally, front metallization was prepared according to the above-described RSI printing recipe at 78 °C on annealed SHJ cells.

Figure 13 shows ρ_m of RSI films printed at various substrate temperatures, bulk ρ of pure Ag (1.6 µΩ·cm), and ρ_m of SP paste pads after curing for 20 min. at 200 °C (20 µΩ·cm). Again, a distinction is made between bulk ρ, and ρ_m, which is used to describe resistivity of a composite or a porous material [22] [22], [47], [60]. As the substrate temperature increases to 78 °C, the RSI film ρ_m decreases, resulting in an average of 4.4 µΩ·cm. At this substrate temperature, the RSI ρ_m is an order of magnitude less resistive than that of the SP paste. The ρ_m of RSI approaches that of pure Ag as residual organics

are removed with elevated temperatures [45]. Upon heating to 90 °C, all organics are volatilized [45]. At 78 °C the RSI film contains traces of these organic residuals, and is porous, which results in ρ_m higher than that of pure Ag. When the substrate temperature is elevated to 107 °C, an even lower ρ_m of 2.0 μΩ·cm is observed. RSI metallization ρ_m is expected to approach that of pure Ag by optimization of: (i) the substrate heating temperature to remove all residual organics, (ii) the RSI recipe to reduce porosity, and

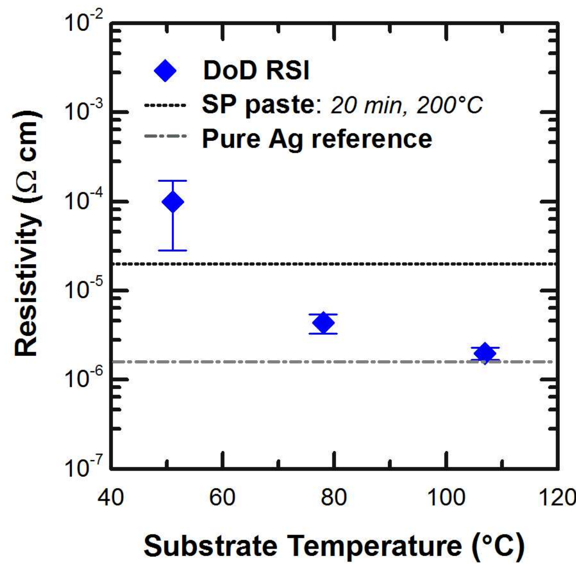

Figure 13. Media resistivity of RSI-printed pads formed for various substrate temperatures compared with the resistivity of pure Ag, and SP Ag paste pads after curing for 20 min at 200 °C, showing that the media resistivity of RSI is lower than SP paste when printed at low temperatures. Figure taken from our publication [55].

(iii) by printing in an inert atmosphere to eliminate oxidation at elevated temperatures [54].

Figure 14 shows total reflectance spectra of films formed from SP paste and RSI compared to a smooth, pure Ag mirror [61]. The spectrum of the RSI film shows high reflectance above the characteristic absorption edge of Ag ~ 310–325 nm, along with the appearance of a distinct dip ~ 350 nm. These are characteristics of a rough Ag surface [61]. This dip around 350 nm is attributed to light absorption by surface

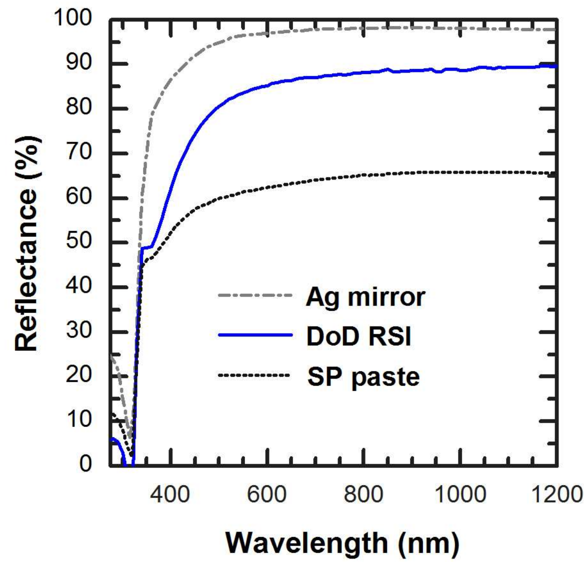

Figure 14. Reflectance spectra of a DoD RSI metallization pad, an SP paste metallization pad, and a pure Ag mirror from [63]. Figure taken from our publication [55].

plasmons on the rough Ag surface, which is negligible for the smooth Ag mirror [61], [62]. For the entire spectral range shown in Figure 14, the SP paste pad exhibits lower reflectance than the Ag mirror and the DoD RSI contact pad, likely due to presence of absorbing organics and polymers.

Next, SHJ cells were prepared with front grid electrodes formed from DoD RSI, and from SP paste, as shown in Figure 15. These solar cells were prepared identically except for the front grid metallization materials. Girds patterns were the same for both the RSI and SP paste cells. The w_f and height were 100–130 µm and 20–25 µm for the SP paste cell, and with more variability 75–145 µm and 1–5 µm for the RSI cell, respectively. In terms of shading losses, w_f for RSI on average is narrower than w_f for SP paste fingers. This should result in lower J_{sc} losses for the RSI cell.

Furthermore, Figure 15 (c) shows imperfections from the DoD printing process, resulting in spots on the bottom region of the RSI cell. This imperfection comes from

instability of the droplet formation during printing. These imperfections add additional shading which, if significant, will result in reduction of photocurrent but is avoidable in the future with further optimization of the printing process.

Figure 16 shows SEM cross-sectional image of a RSI finger on a SHJ cell. It is clear that the RSI has a porous morphology. Interestingly, this SEM image shows a non-uniform coverage of the cell surface, leaving regions of the textured solar cell exposed. The resulting morphology on the textured solar cell surface is expected to influence the RSI metallization properties, such as finger resistance, specific contact resistance, and adhesion and reliability. The exposure of the underlying cell under the

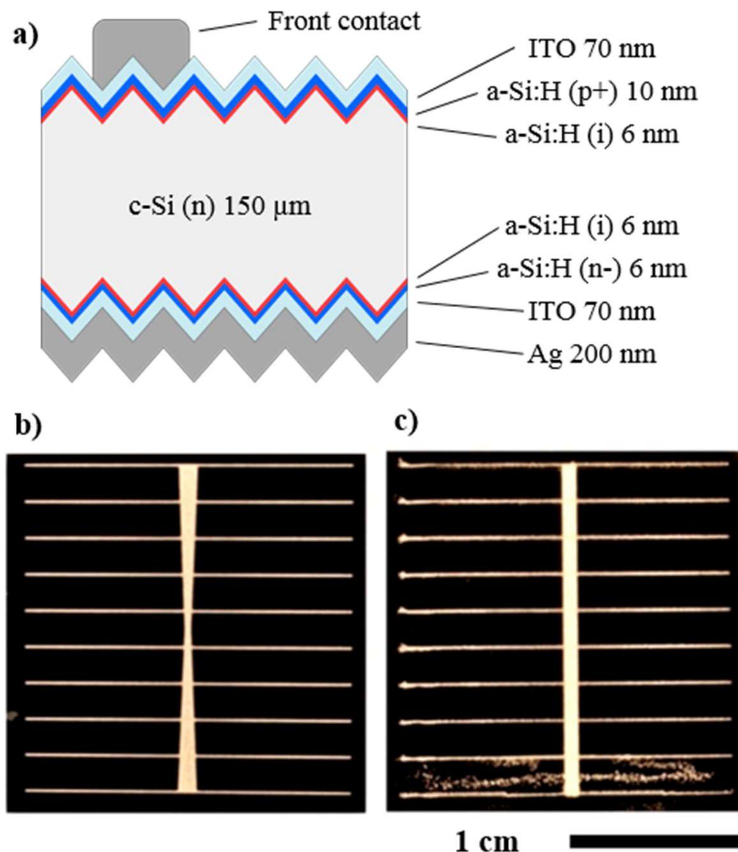

Figure 15. Schematic of SHJ solar cell layers in cross-sectional (a) contrast enhanced photograph of SHJ solar cells with front-grid metallization formed from (b) SP paste and (c) DoD RSI. Figure taken from our publication [55].

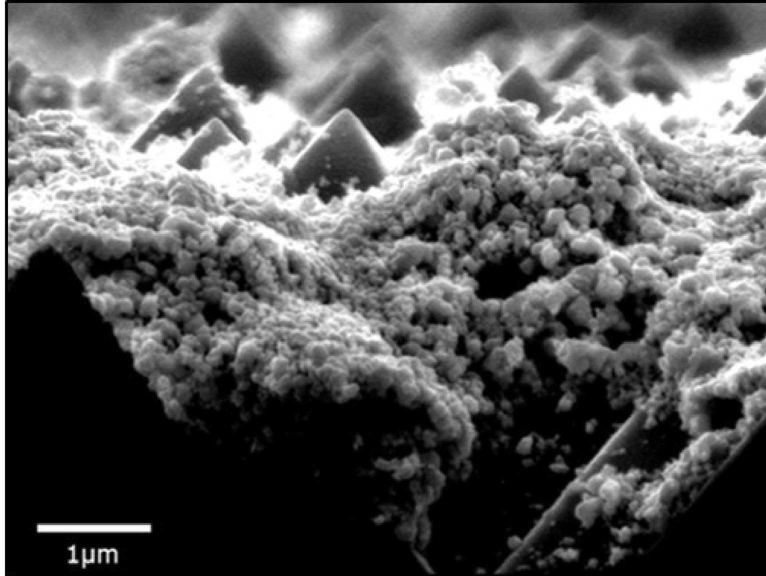

Figure 16. SEM cross-sectional image of a porous DoD RSI finger on a textured SHJ solar cell. Figure taken from our publication [55].

RSI finger might transmit some light through, and potentially increase in photogeneration current. This is discussed in more detail in Chapter 3.2.1.

Solar cell fingers with minimal w_f but high cross-sectional area (high aspect ratio) will result in minimal resistive and shading losses. Interestingly, as shown below, the solar cell prepared with RSI front grid performs comparably to the SP paste solar cell—before complete process optimization— despite fingers with low aspect-ratio, high porosity, and poor adhesion, showing there is room for improvement. This result highlights the motivation for the rest of this work.

Table 2. Comparison of solar cell electrical characteristics for one SP Paste cell, and one DoD RSI cell.

	V_{oc} *(mV)*	J_{sc} *(mA/cm^2)*	***pFF*** *(%)*	***FF*** *(%)*	R_s *(Ω•cm^2)*	***η*** *(%)*
SP Paste Cell	713	35.9	81.3	76.3	1.1	19.5
DoD RSI Cell	712	35.5	80.9	72.9	1.8	18.4

Solar cell performance was evaluated from suns-V_{oc} and one-sun I-V characterization. Pseudo-fill factors (pFF), fill factors (FF), open-circuit voltage (V_{oc}), short-circuit current density (J_{sc}), and series resistance (R_s) are compared for the SP paste and RSI cells (see Table 2). Figure 17 shows the I-V characteristics of the SP paste and DoD RSI cells, taken from our study reported in full detail elsewhere [54]. The SP paste cell and DoD RSI cell demonstrate similar V_{oc} of 713 and 712 mV, and J_{sc} of 35.9 and 35.5 mA/cm^2, for the SP paste and DoD RSI cell, respectively. The small difference in J_{sc} likely originates from additional shading from the imperfection spots from RSI printing instability (shown in Figure 15 (c)). Here it is important to note that the comparable values in pFF, J_{sc}, and V_{oc} for both types of cells suggests that only the difference in front grid metallization methods affect R_s. Next, we compare the suns-V_{oc} and one-sun IV characteristics. R_s (shown in Table 2) is calculated from the voltage difference (ΔV) at maximum power point (MPP), from the suns-V_{oc} and one-sun I-V curves [20], [54], [63]:

$$R_s = \frac{\Delta V}{J_{MPP,OneSun}} \quad \text{Equation 3.1}$$

The difference in R_s is assumed to be only result from differences in resistance of the front grid, and the interfacial contact resistance ρ_c of the front grid to the ITO/Si. The RSI fingers have lower ρ_c than SP paste. However, R_s losses have only a square root dependence on ρ_c; whereas the R_s losses scale proportionally with R per unit length [21], [64]. Thus, in our case where ρ_c values have a wide range due to variations in interfacial connectivity of the porous DoD RSI fingers to the ITO, the difference in the resistance of the fingers per unit length outweighs the benefit of lower average ρ_c [54].

We suggest that this accounts for the slightly higher R_s of the cell with the RSI printed finger [54].

The work presented here demonstrates that there is a path towards exceeding the performance of SP paste using RSI metallizations. The following points must be addressed to improve RSI metallization performance: (i) approach closer to pure Ag resistivity by reducing porosity, (ii) optimize printing parameters to reduce shadowing from imperfect Ag spots, (iii) finally find the optimal power loss tradeoff between porosity, use of adhesion modifiers, features' thickness, and possible enhanced photogeneration by transmission of

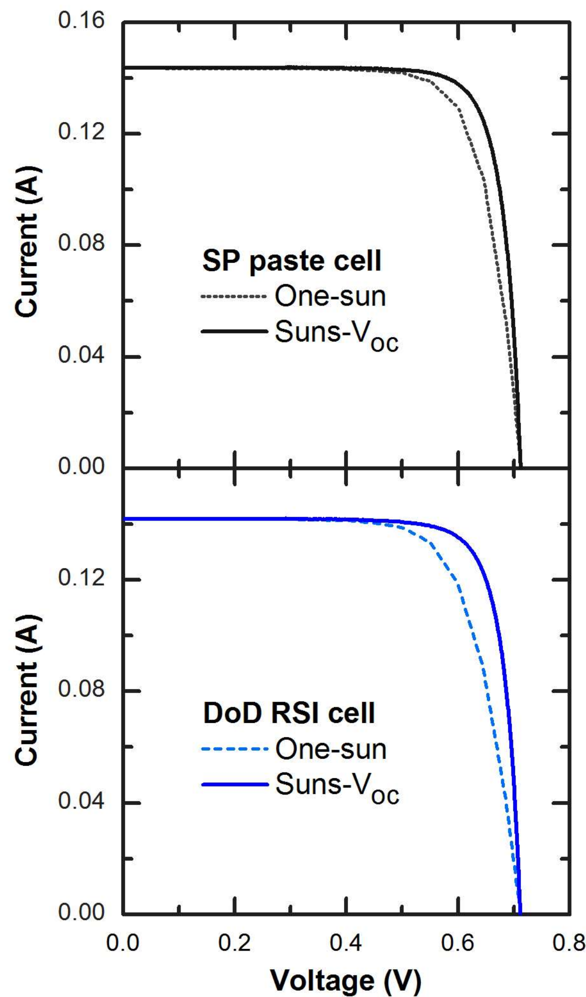

Figure 17. One-sun and suns–V_{oc} – I–V curves for SHJ solar cells with front-grid metallizations formed from SP paste (top) and DoD RSI (bottom). Figure taken from our publication [55].

light through the exposed textured peaks of the solar cell. These points are addressed in the following chapters.

3.2 Optical and Electrical Properties of Reactive Silver Ink Metallization

An ideal solar cell front grid metallization would be completely transparent and have no resistance. In reality, there are power losses from resistive voltage drop in the grid, and in photogenerated current from shading from the grid, as described in Chapter 1.2. First in this chapter, RSI geometric and optical properties, namely finger width (w_f), reflectance, transmittance, and absorptance are characterized for varying deposition parameters, Next, RSI media resistivity (ρ_m) is evaluated in relation to geometry and porosity by varying number of layers printed, and time delay between printing additional layers. An understanding of the influence of these parameters on RSI characteristics enables approaches to minimize power losses in full devices.

*3.2.1 **Optical Characterization of RSI***

Previous work in Chapter 3.1.1 compared the reflectance spectra of an RSI film, an Ag paste film, and a smooth Ag mirror surface, showing that the RSI film exhibited a reflectance spectra representative of a rough porous Ag surface [54]. This previous work also showed resistive power losses due to low cross-sectional area of the RSI fingers as exemplified by the SEM image in Figure 16. In this SEM image, the porous, low-aspect ratio RSI finger only partially shaded the textured ITO/Si surface of the cell underneath; Peaks of the textured surface were visibly exposed through the regions of the finger, possibly contributing to additional photogenerated current. Thus, the morphology and optical properties of RSI fingers might open up the opportunity for

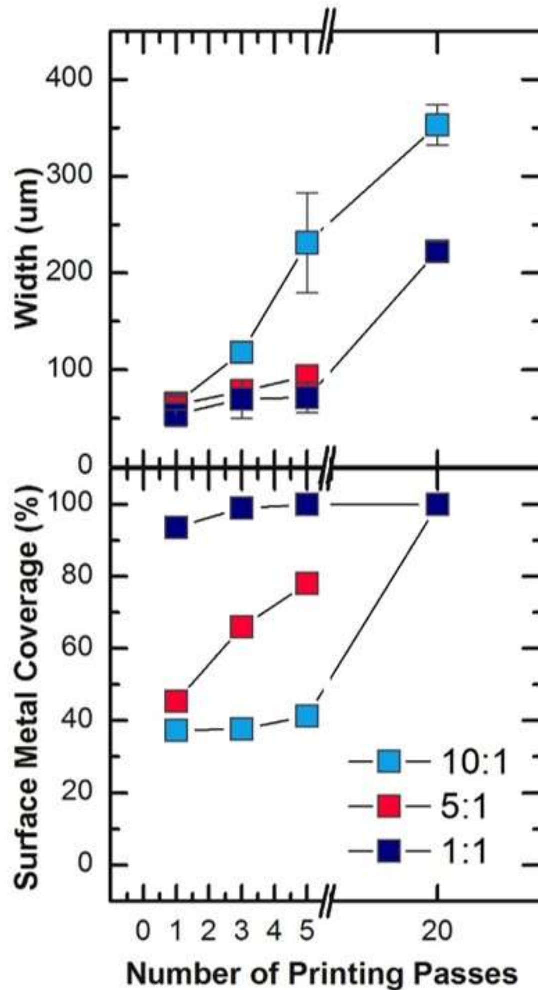

Figure 18. Finger width (w_f) and surface metal coverage of a DoD-printed RSI finger as a function of number of printing passes, for RSI prepared with solvent:ink ratios of 10:1, 5:1, and 1:1.

additional current generation from increased light transmission through the porous, low-profile structure. Here, investigation of the geometric and optical properties of RSI inks with varying solvent:ink ratio studies the possibility to tune the morphology of the film and therefore the power losses due to shading by RSI metallizations. Of course, these potential gains must be balanced against resistive losses.

Several factors contribute to changes in optical and geometric properties of RSI metallization. As RSI is printed on a textured surface of a solar cell, the ink will flow into the valleys, the conformality of the resulting RSI finger will be different than on a flat

substrate. Additionally, solvent to ink ratio and increasing the number of print-passes (this is related to thickness) will affect w_f, peak exposure, resistance, and continuity of conductive Ag particles in the finger.

RSI fingers with varying number of layers, and solvent:ink ratios were prepared to study the relation to surface shading (surface metal coverage), w_f, and finger continuity. The base ink was prepared following Walker and Lewis [43]. The base ink was then diluted with ethanol to prepare inks with solvent:ink ratios (vol.) of 10:1, 5:1, and 1:1.

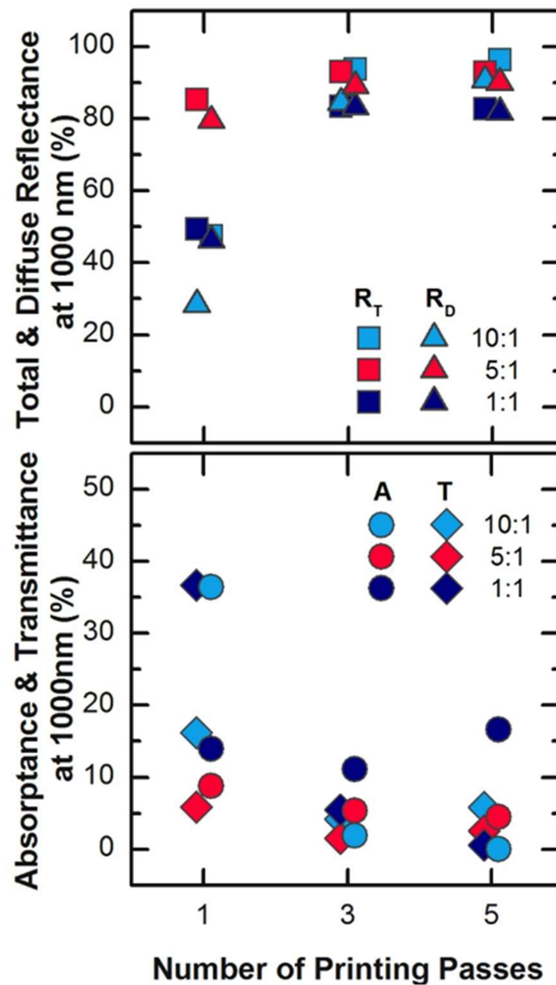

Figure 19. Optical properties of RSI for varying number of printing passes (layers) and solvent:ink ratios.

RSI fingers were printed 1-, 3-, and 5-layers thick on ITO-coated textured silicon (representative of a SHJ cell surface). Finger continuity was obeserved by optical microscope images and confirmed by two-point resistance measurements at the ends of each finger.

Figure 18 shows width and surface metal coverage of RSI fingers for increasing number of print passes and solvent:ink ratios. Surface metal coverage (area of metal coverage in the central region of a finger) was quantified by image processing of optical microscope images. The fingers formed from more dilute inks (10:1 and 5:1 solvent: ink ratios) show less surface coverage compared to the 1:1 ink. At low surface coverage (less than ~60 %) fingers are not continuous; Percolation of current is limited by incomplete connectivity of Ag particles, especially for low number of printing passes.

Next, optical properties were measured by spectrophotometry for RSI of varying number of printing passes (number of layers), and solvent:ink ratios. The base ink was prepared following Walker and Lewis [43]. The base ink was then diluted with ethanol to prepare inks with solvent:ink ratios (vol.) of 10:1, 5:1, and 1:1. 1 cm^2 films of these RSIs

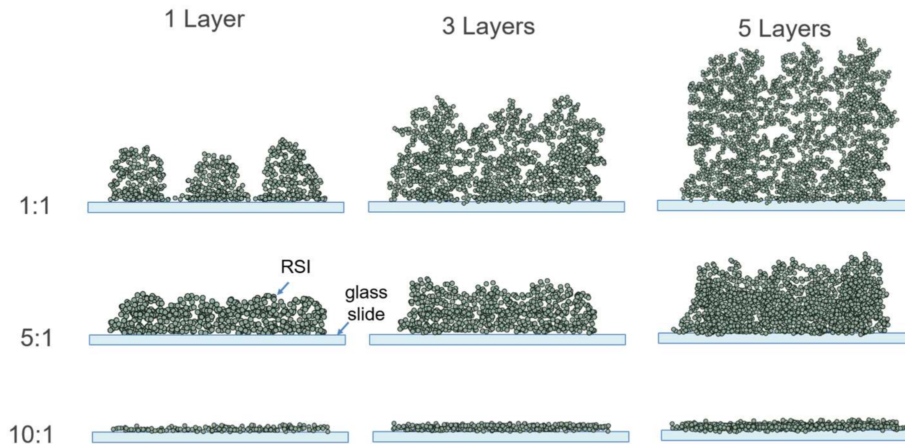

Figure 20. Schematic of RSI film morphology for varying number of print passes, and solvent:ink ratios.

were printed 1-, 3-, and 5-layers thick on glass slides for optical measurements. Spectrophotometry was conducted using an integrating sphere with an opening for specular reflectance (Perkin Elmer). Total reflectance (R_T), diffuse reflectance (R_D), and transmittance (T) were measured, and absorptance (A) was calculated (A= 100% - T – R). Figure 19 shows these measured and calculated optical properties of the RSI films. To aid the discussion of the optical properties, Figure 20 shows exaggerated schematics of RSI film morphology for varying number of print passes, and solvent:ink ratios.

The 1:1 ink has higher silver ion loading, and results in a more porous film compared to the 10:1 ink [47]. Since the 1:1 ink has 1-part solvent to 1-part RSI, the reaction rate is faster than for the more diluted 5:1 and 10:1 inks. This more concentrated 1:1 ink causes faster aggregation of Ag particles around pockets of solvent, leaving larger pores upon evaporation [47]. Additionally, the 1:1 ink is less viscous when printed, so the ink droplets will wet and coalesce less than the more dilute inks. The optical characteristics of our samples are in line with these contact morphology observations.

For 1-pass-thick samples, the 1:1 film exhibits the highest R_T and highest relative R_D from scattering of light off the rough porous surfaces. The 5:1 and 10:1 inks are less porous, and smoother, show decreasing R_D trend with increasing ink dilution. For to 3-passes-thick samples, T through the 1:1 ink film decreases since light is absorbed or reflected off the thicker Ag film. Still the 10:1 ink shows the lowest relative R_D, suggesting a relatively smoother surface morphology of the film. The 5-passes-thick RSI films follows trends that are expected to continue as the number of passes increases; all films become thicker and show decreased T through the thicker layer of

Ag. Furthermore, as dilution increases, T increases, A decreases, and relative R_D decreases due to smoother, more dense film morphology from slower reaction rates.

This study shows the impact of solvent:ink ratio on finger width, surface metal coverage, and optical properties of reactive silver ink metallizations, and that these observations are in line with film morphology [47]. The low aspect ratio finger (Figure 16 in Chapter 3.1.1) that inspired this study was made from the 1:1 ink printed 5-passes-thick. From this previous study, we concluded that R_s of the cell could be improved by reducing the finger resistance by printing more layers. Here, the RSI film printed 5-passes-thick with 1:1 ink, transmittance is negligible. Still, measured diffuse reflectance was high for all solvent:ink ratios investigated, suggesting that some light might be reflected into the cell near the edge of the metallization. However, it should be emphasized that this study uses a 1 cm^2 film of RSI on a flat glass slide to measure optical properties, not fingers printed on a textured cell. We suggest that the trends in optical properties are translatable to textured surfaces, but that there might be a shift in transmittance, reflectance, and absorptance values from the values reported for larger area RSI films on flat glass (Figure 19).

3.2.2 Electrical Characterization of Reactive Silver Ink

Previous work presented in Chapter 3.1.1 showed that although the RSI metallization had lower ρ_m, and lower average ρ_c, R_s was higher in a solar cell with a front grid formed from RSI front grid metallization compared one with a front grid formed from screen-

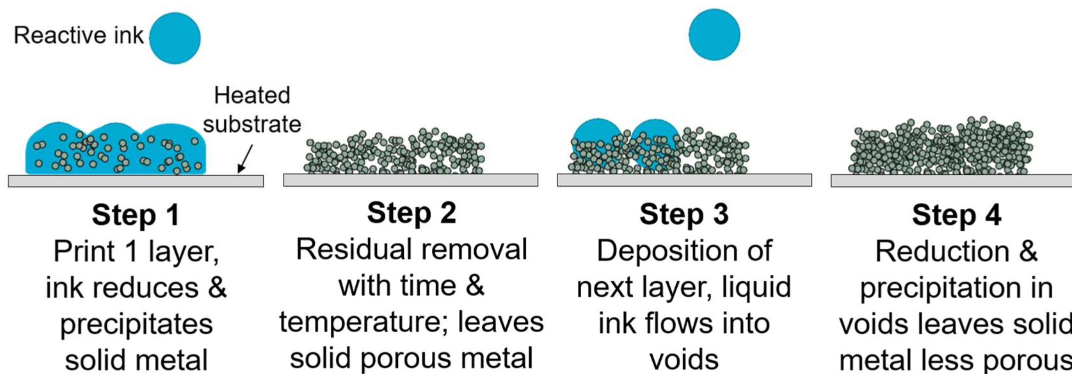

Figure 21. Schematic of the in-filling process. A reactive ink (blue) is deposited onto a heated substrate. The ink is allowed to dry completely and volatilize all residuals before printing additional layers, resulting in a less porous feature than the previous layer.

printed Ag paste (SP Ag paste). This was due to higher resistance, *R,* per unit length of the RSI metallization compared to the SP Ag paste. This higher *R* comes from two factors, first, the low cross-sectional area of the fingers, and second the high porosity. These factors are shown by Figure 16 in the previous work in Chapter 3.1.1 [54].

The cross-sectional geometry of the fingers is dependent on wetting of the RSI to the substrate, and the number of layers printed (passes of the print-head). Porosity is dependent on the solvent type, the solvent to ink ratio, and the temperature of the substrate during deposition [47]. Lefky *et. al.* [47] did a systematic study on the impact of various solvents and solvent:ink ratios at various substrate temperatures on RSI properties and Zhao *et. al* [65] investigated the percolation-limited media resistivity of RSI metallization.

Since power losses of RSI metallization are dependent on the ρ_m, and therefore the porosity, it is extremely important to accurately evaluate the void content and identify ways to tune the desired characteristics. These DoD-printed RSI metallizations rely on printing precursors to a chemical reaction and printing one layer at a time. We

hypothesize that changing the time between printing additional layers, allowing each layer to dry and fully react before printing additional layers, will influence the reaction kinetics and therefore influence the morphology and porosity. Details on how reaction kinetics influence morphology and porosity are reported in detail by Lefky *et. al.* [47].

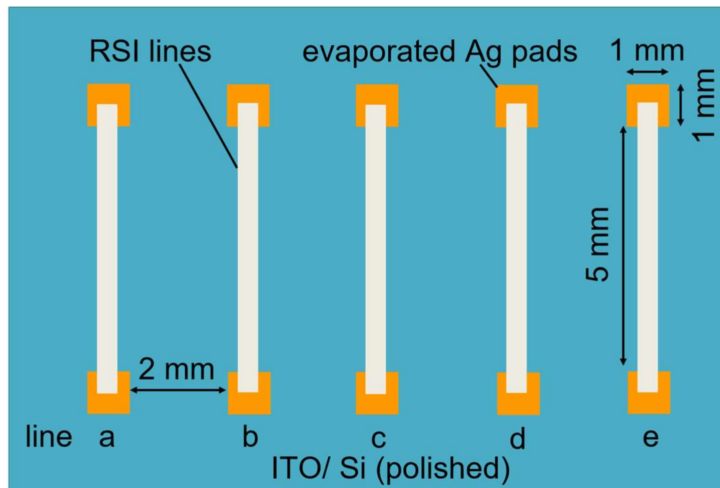

Figure 22. Schematic of RSI lines printed on ITO coated Si polished substrate. The use of the evaporated Ag pads allows electrical probing without damaging the RSI pads.

Another hypothesis is that if the first layer is allowed to dry before the next layer is deposited, the newly deposited layer can in-fill into the pores of the first layer, reducing the porosity of the RSI metallization. This process is exemplified in Figure 21. First, a reactive ink (blue) is deposited on a substrate heated to a mild temperature (generally room temperature – 120 °C), the ink begins to reduce and precipitate solid metal (shown in Step 1 by small grey circles in the blue ink). Step 2 consists of removing all residuals, such as solvents and acetates, with the mild temperature of the substrate over time, yielding a solid, yet porous metal feature. Step 3 shows the deposition of the next layer of the reactive ink over the dried porous metal feature, the liquid ink then flows into the voids. Finally, Step

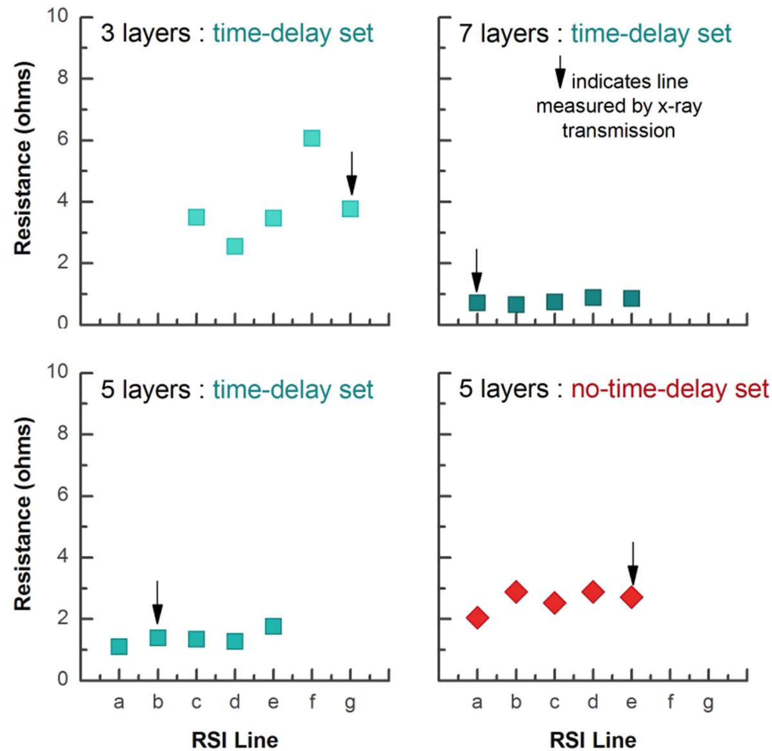

Figure 23. Line resistance of five 5-mm-long RSI lines for 3-, 5-, and 7-layers with time delay between printing consecutive layers, and 5-layers RSI lines with no time delay between printing consecutive layers. The no-time-delay 5-layers lines have higher average resistance compared to the time-delay 5-layers lines despite having the same amount of Ag per line. The arrow indicated lines that were further characterized by x-ray transmission.

4 shows the ink reduces and precipitates in voids and on top of the previously printed layer; After enough time and applied temperature, the residuals are removed completely resulting in a solid metal structure that is less porous than the previous layer.

To test these two hypotheses, we designed an experiment to evaluate the change in in electrical and morphological properties of RSI lines as time delay between layers varied, and as the number of layers varied. As shown later, electrical probing can lead to detrimental scratch damage to the RSI metallization making it difficult to measure the electrical properties, especially for a large number of samples. For this reason, a new test structure was designed and fabricated to characterize the electrical properties

of RSI lines with minimum risk of damage. A schematic of the line resistance test structure is shown in Figure 22. The test structure consists of sets of parallel electron-beam evaporated Ag pads (1 mm ×1 mm) spaced 5 mm apart. The substrate is thin polished Si (~100-120 μm) coated with 80 nm of indium-tin-oxide (ITO). ITO was deposited by RF sputtering using an Angstrom EVOVAC deposition tool, the ITO target composition was 90/10 % by weight ratio of In_2O_3/SnO_2. The resistivity of the ITO, measured with a 4-point probe, is much higher (~10 Ω·cm) than that which would be used on a solar cell device (6×10^{-4} Ω·cm). The purpose of this high resistivity ITO was to have an ITO surface for printing on, while also keeping the current flow path mainly through the RSI lines only.

The resistance of each RSI line was measured using a 4-wire resistance measurement. Current was sourced from a probe placed on one evaporated Ag pad (bottom Ag pad a, Figure 22), through the RSI line and leaves through the current probe on the other evaporated Ag pad (top Ag pad a, Figure 22). The resistance was measured by probing the voltage drop across the RSI line and the evaporated Ag pads. Resistivity of the evaporated Ag pads is ~ 1.6 μΩ·cm and 200 nm in height, the resistance contribution from the Ag pad is less than 0.08 Ω, which is an order of magnitude lower than the total resistances measured for all RSI lines in this experiment and is considered negligible.

A series of RSI lines were printed on these test structures. The base ink was prepared following Walker and Lewis' recipe [45]. All chemicals were used as received. 1.0 g of silver acetate ($C_2H_3AgO_2$, anhydrous 99%, Alfa Aesar) was dissolved in 2.5 mL ammonium hydroxide (NH_4OH, 28-30 wt%, ACS grade, BDH Chemicals). The solution was then stirred for 2 minutes on a vortex mixer to dissolve the silver acetate. Next, 0.2

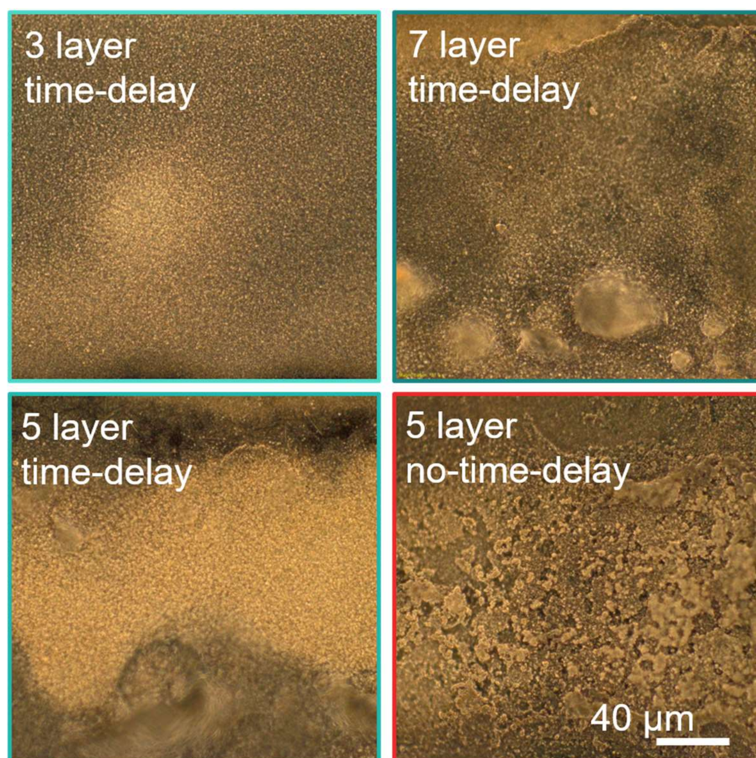

Figure 24. Top-view optical microscope images of each RSI lines indicated by arrows in Figure 23. Line resistance of five 5-mm-long RSI lines for 3-, 5-, and 7-layers with time delay between printing consecutive layers, and 5-layers RSI lines with no time delay between printing consecutive layers. The no-time-delay 5-layers lines have higher average resistance compared to the time-delay 5-layers lines despite having the same amount of Ag per line. The arrow indicated lines that were further characterized by x-ray transmission.. This qualitatively shows the difference in RSI morphology for time-delay RSI lines and no-time-delay RSI line.

mL of formic acid (CH_2O_2, ≥96%, ACS reagent grade, Sigma Aldrich) was added in two steps with a quick stir at the end of each step. The ink was then allowed to sit for 12 hours before being filtered through a 450 nm nylon filter. For the experiments reported here, the RSI was diluted 1:1 by volume with ethanol (EtOH, C_2H_6O, ACS reagent grade, Sigma Aldrich) and then filtered again through the 450 nm nylon filter immediately before use. The RSI lines were printed on substrates heated to 66 °C. The droplet diameter, which determines the amount of Ag deposited, was equal to 44.77 μm for each line. This means the amount of Ag per layer was kept constant for all lines.

One set of samples, referred to as “no-time-delay set”, consisted of 5 lines of 5-layer-thick RSI lines. Each consecutive layer was printed immediately following the completion of the previous layer. Another set of samples, referred to as “time-delay set”, consisted of 5 lines of each 3-, 5-, and 7-layers thick RSI lines. A 225 s time delay was employed between printing of each layer to allow the previous layer to dry fully before printing additional layers. The resistance of these lines is shown in Figure 23 , showing that for the time-delay set, resistance of the lines decreases with increasing number of layers. 5-layers thick lines with time-delay have a lower average resistance than those with no-time-delay. One line from each series was also characterized by profilometry and synchrotron x-ray transmission (XRT), these lines are indicated by arrows in Figure 23. Figure 24 shows optical microscope images these indicated RSI lines; qualitatively showing a smoother, more uniform morphology for the lines printed with time-delay between layers.

Next, the media resistivity, ρ_m, is determined for each line indicated by an arrow in Figure 23 using the following relation:

$$\rho_m = \frac{RA}{L} \qquad \text{Equation 3.2}$$

where *R* is the measured line resistance, *A* is the cross-sectional area, and *L* is the length of the line. The average cross-sectional area of each line was determined by 3D profilometry mapping of the entire length of the line using a Bruker Dektak XT profilometer with a 2 µm radius stylus, with 2.5 mg applied stylus force, vertical resolution less than 10 nm and lateral resolution of 30 nm. The average cross sections of each line are

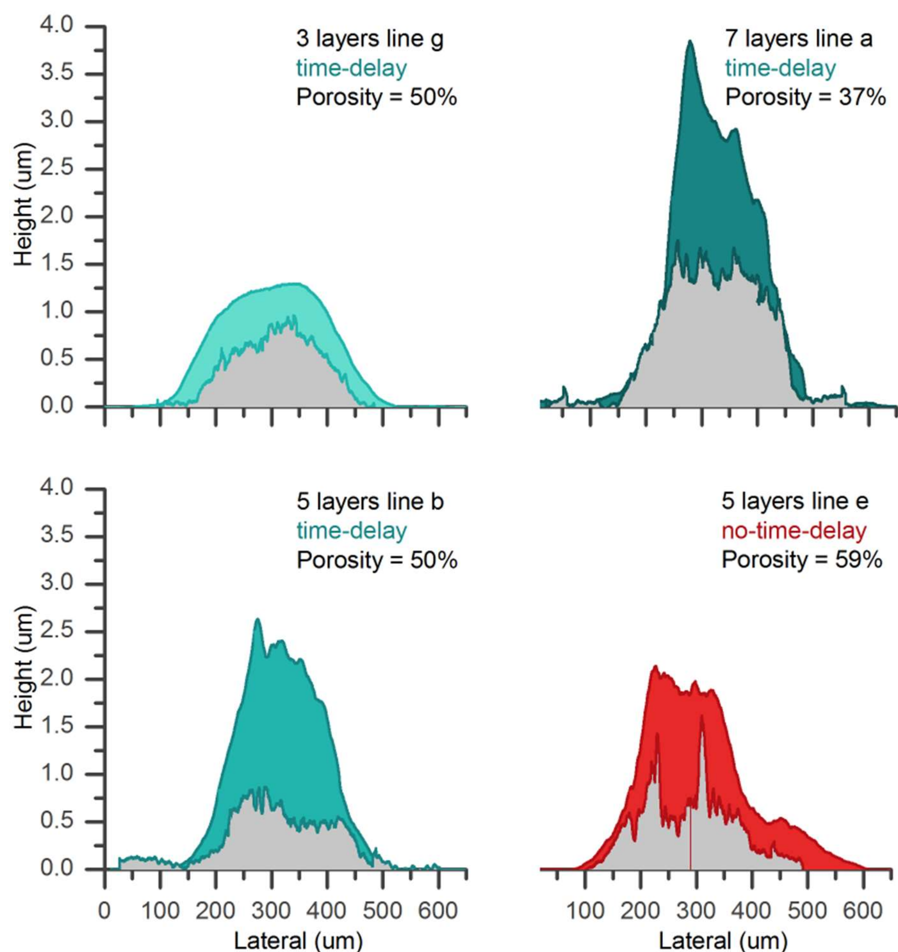

Figure 25. Average cross-sectional profiles determined from profilometry mapping of the entire length of RSI lines (blue and red profiles), and cross-sectional thickness of pure Ag from synchrotron x-ray transmission (grey profiles). The average cross-sectional area A from profilometry is used to determine ρ_m, and the cross-sectional thickness of pure Ag is used to determine the porosity.

shown in Figure 25, and the media resistivity is shown in Figure 26. For the time-delay RSI lines, the media resistivity decreases as number of layers increases, suggesting that there could be in-filling of pores as additional layers are printed on top of dried RSI. To verify this, the porosity must be quantified.

To quantify porosity, synchrotron XRT measurements were done at Argonne National Laboratory to determine the amount of Ag present in the RSI lines. This characterization method allows for the precise determination of the quantity of Ag in

each line with high spatial resolution. The 12.8 keV x-ray beam (~200 nm spot size) is scanned across the width of each line in 3 locations with 100 nm step size. Beer-Lambert law is used to quantify a profile of the thickness of Ag present across each line:

$$\frac{I}{I_0} = \mathrm{e}^{-\mathrm{d}\sigma\mathrm{t}} \qquad \text{Equation 3.3}$$

where I_0 is the initial intensity of the x-ray before traveling through the RSI line, I is the intensity of the x-ray transmission as it is attenuated through the RSI, d is the density of Ag (10.5 g/cm^3), σ is the capture cross section of the x-ray at 12.8 keV through Ag (6.121×10^1 cm^2/g), and t is the thickness of Ag. Each scan across the width of an RSI line will yield a thickness profile of Ag vs. lateral distance. The cross-sectional area of this Ag thickness profile will then be compared to the cross-sectional profiles from profilometry. The profilometry cross-sections include extra area from pores, while XRT is only attenuated significantly through the Ag, not through the air in pores. Thus, the porosity can be precisely calculated as:

$$Porosity\ (\%) = \frac{Area_{profilometry} - Area_{XRT}}{Area_{profilometry}} \times 100 \qquad \text{Equation 3.4}$$

Though the porosity of RSI metallization has already been reported by others previously [45], [47], [65], the work here lays out the hypothesis that the porosity is not only a function of solvent type, solvent:ink ratio, and substrate temperature; the number of layers and time delay between printing additional layers can also influence the porosity and therefore media resistivity. Understanding how to control and reduce the porosity is extremely important in reducing power losses from RSI metallization for solar cells. These results suggest that porosity is lower when each layer is allowed to dry fully before printing an additional layer, allowing the ink to seep into the pores of the dried metallization. Additionally, with a time-delay between layers, the media resistivity decreases with

increasing number of layers, showing that improvements in media resistivity in addition to line resistance are achieved through printing of more layers.

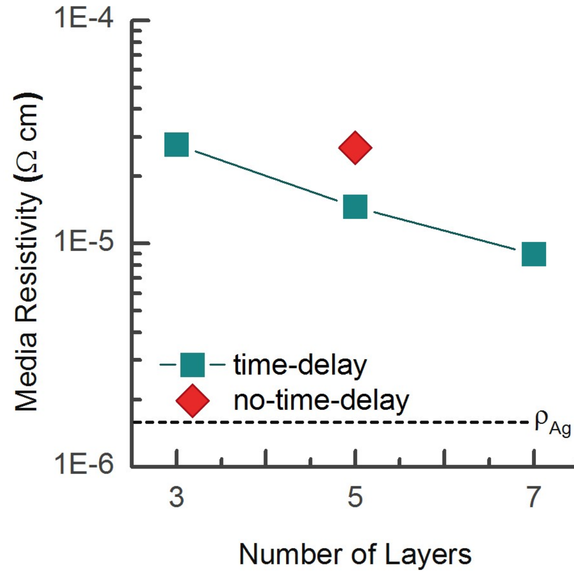

Figure 26. Media resistivity of RSI lines compared to the resistivity of pure Ag (dashed line). For the RSI lines with time-delay between printing of layers, the media resistivity decreases as number of layers increases, suggesting in-filling of pores as additional layers are printed on top of the dried RSI.

4. ADHESION & SPECIFIC CONTACT RESISTANCE

So far in this work, only factors contributing to power losses by the front grid metallization have been discussed. First, Chapters 3.1.1-3.2.2 reported the media resistivity, ρ_m, of RSI metallization along with geometric factors govern the total power lost from grid resistance. Second, Chapters 3.1.1 and 3.2.1 reported on optical and geometric factors that are responsible for power losses from shading by the grid.

In this chapter, factors contributing to power losses at the metallization-cell interface are detailed. First, adhesion performance of DoD printed RSI on ITO is introduced in Chapter 4.1. Second, a Sn-sensitization layer is investigated as a printable adhesion-promoting layer for RSI on ITO in Chapters 4.2-4.3. Third, the effectiveness of the Sn-sensitization solutions on ITO surfaces are thoroughly investigated. RSI and ITO interface properties such as ρ_c, adhesion performance, and surface modification by tin-sensitization solutions are detailed in Chapters 4.4 and 4.5.

4.1 The Effect of In-Filling on Adhesion Performance

Our initial studies showed adhesion performance of RSI fingers on ITO varies significantly with ink composition and printing parameters. This chapter introduces work done to understand these variations in adhesion performance. This work, done in collaboration with A. Mamidanna and O. Hildreth, has been reported in full detail elsewhere [66]. However, the main results of this work are briefly summarized here, as adhesion performance is an essential part of evaluating reactive ink metallizations for use on solar cells.

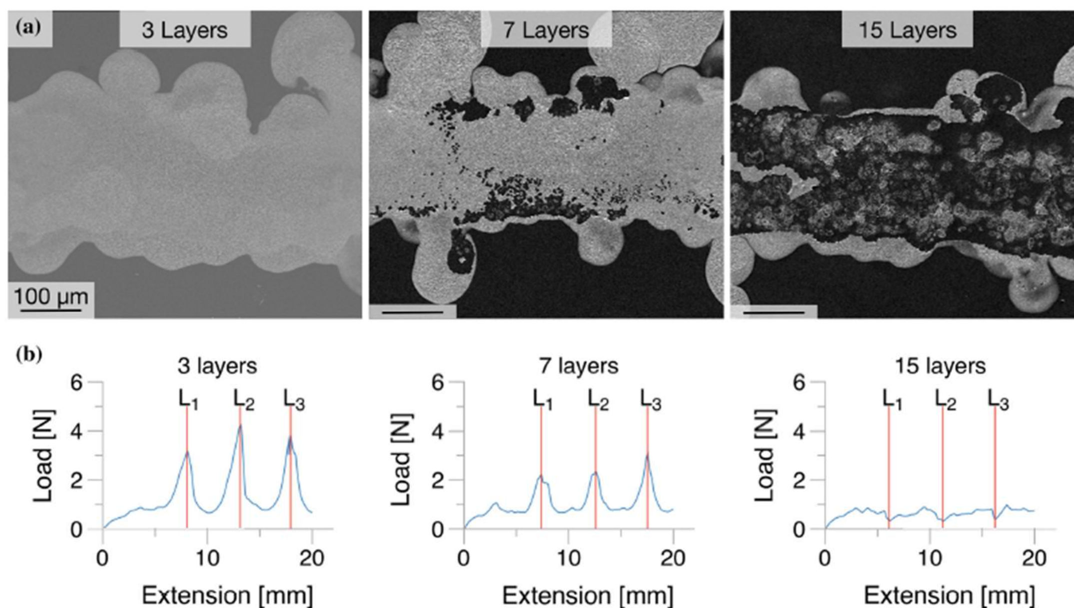

Figure 27. (a) SEM images of 3, 7, and 15-layer RSI samples after tape peel testing.; (b) Load versus extension plots for the 3, 7, and 15-layer RSI lines are shown. L_1, L_2, L_3 denotes location of the three RSI lines printed on the ITO films. Figure taken from Mamidanna *et al*. [67].

A series of RSI samples were prepared to determine adhesion performance for different printing parameters. Each sample consisted of three RSI lines printed on ITO-coated polished Si wafers. A narrowed parameter space investigation of ink concentration and number of layers was carried out to differentiate between "good" and "poor" adhesion performance. Adhesion performance was quantified using a 180° peel test, and top-down optical and scanning-electron microscope image processing, and profilometry mapping. 180° peel tests measure load versus extension, indicating the force necessary to peel tape off the ITO and RSI surface of the sample. Top-down scanning electron microscope (SEM) images are used to observe adhesive failure. Complete results from optical microscope image processing and profilometry mapping are reported in detail elsewhere [66].

Figure 27 exemplifies an important result from this study [66]. Figure 27 (a) shows top-down SEM images of RSI lines printed on ITO-coated polished Si wafers after 180° tape peel testing, for increasing number of layers. The light grey horizontal lines are the printed RSI lines, and the darker grey regions (above and below the RSI line) are the ITO films. For the 3-layers thick RSI line, the inner region of the RSI line remains intact after peel testing, appearing to have no adhesive failure between the RSI and ITO. Whereas, the 7-layers thick RSI line shows some adhesive failure in the inner region of the RSI line. Furthermore, the 15-layers thick RSI line shows significant adhesive failure compared to the 3-layers and 7-layers thick RSI lines.

Figure 27 (b) shows load versus extension for 180° peel tests. The location of each of the three RSI lines is marked by L_1, L_2, L_3 on the extension axis. Where the tape is peeled off the ITO film only, the peel force is between 0-1 N for the 3-, 7-, and 15-layers thick RSI lines. For the 3-layers thick RSI lines, the peak load is between 3-5 N on the RSI lines, showing a higher force is applied to peel the tape off the RSI compared to the ITO film. For the 7-layers thick RSI lines, the peak load magnitude decreases to 1-3.5 N, indicating less force is needed to peel the tape from 7-layers thick RSI lines compared to the 3-layers thick RSI lines. For the 15-layers thick RSI lines, there is a dip in the load at the RSI line locations, showing that the adhesive force of the RSI to ITO is less than that of the tape to the ITO surface. As discussed in earlier chapters, finger resistance can be reduced by printing more layers. However, these results suggest that printing more layers results in poor adhesion performance compared to printing fewer layers.

These results, similarly to the results presented in Chapter 3.2.2. suggest that in-filling of the porous RSI lines by additional layers changes the RSI line properties (see Figure

21). Here, adhesion performance is altered by in-filling, and entrapment of volatile solvents under the solid Ag film formed during the RSI reaction. The pressure built up by the entrapped solvents as they volatilize can be relieved by breaking or puckering in the RSI line, and by delamination of the RSI line from the ITO surface, resulting in decreased adhesion performance. Mamidanna *et al*. showed that diluting the reactive ink reduced this observed puckering phenomenon and improved adhesion performance of RSI on ITO [66]. Most importantly, this study shows that adhesion of reactive ink metallizations can be significantly improved while still forming high aspect- ratio silver lines [66].

4.2 Properties of a Sn-Sensitization Adhesion Promoting Layer

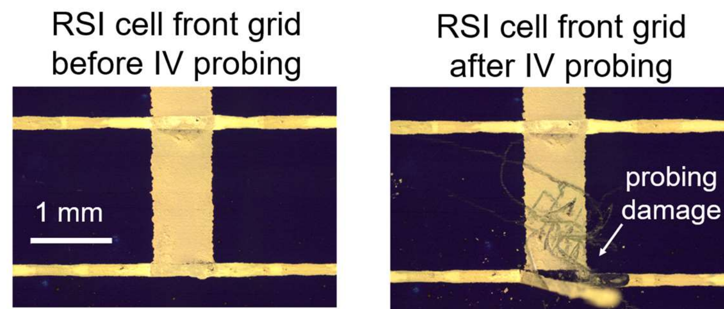

Figure 28. Optical microscope images of a region of the front grid of the RSI SHJ cell without the use of an adhesion promoter before and after IV testing. This shows finger dislodgement from a probe scratch during IV characterization. This exemplifies the importance of improving the durability of RSI metallization for solar cells.

Development and characterization of an adhesion promoting layer is important for durability of RSI cells throughout processing and testing, and ultimately for durability of cells through deployment in the field for 20+ years. Figure 28 exemplifies the necessity for improved adhesion of RSI metallization on solar cells, showing dislodgement of an RSI finger from a probe scratch during electrical characterization. This chapter details several investigations using Sn-sensitization and Ag-activation to

improve adhesion of reactive silver inks on ITO. First in Chapter 4.2.1, Sn-sensitization and Ag-activation is introduced, and the standard process that has been used to improve Ag adhesion on glass substrates industrially for decades is detailed. Next, in Chapter 4.3, a modified process is developed with the goal of producing a printable, electrically conductive adhesion promoter using Sn-sensitization and Ag-activation on ITO surfaces. Then, Chapter 4.4 outlines several experiments used to understand the effects of the printable Sn-sensitization solution on ITO surfaces. Finally, Chapter 4.5 introduces a study on the process of Sn-sensitization and Ag-activation on ITO surfaces, and compares these processes to those on glass surfaces.

4.2.1 Introduction to Sn-Sensitization with $SnCl_2$ Solutions

The aim of Chapters 4.2-4.3 is to develop a printable adhesion promoting layer for RSI on ITO surfaces, while also improving and specific contact resistance (ρ_c). In this case, a Sn-sensitization solution is used as the "adhesion promoting" layer for RSI on ITO surfaces. This adhesion promoting method is based on a set of processes which is commonly referred to as Sn-sensitization and Ag-activation [67], [68]. Historically, Sn-sensitization and Ag-activation were frequently used to improve uniformity and adhesion of Ag mirrors on glass substrates [68]. Here, we aim to apply Sn-sensitization to ITO surfaces, and use RSI as the Ag-activation solution.

A schematic representation of the Sn-sensitization and Ag-activation process on soda-lime glass is generalized and depicted in Figure 29 [52]. First, Sn-sensitization solution (typically made from $SnCl_2$, HCl, and H_2O) reacts with surface species to uniformly modify the glass surface. Specifically, the reaction mechanism involves Sn reacting with the hydroxyl-terminated surface of the substrate to form a covalent bond [52]. Following Sn-

sensitization, the surface is exposed to an Ag-activation solution (typically $AgNO_3$ and H_2O), which reacts with the Sn-sensitized sites, and creates uniformly catalytic sites for further Ag deposition. Specifically, the "sensitized" Sn sites act as nucleation sites for Ag cations in the Ag-activation solution, forming bonds between the Sn and Ag. Again, this process has been used for decades to improve adhesion of Ag films on glass [52], [68]. Here we suggest that the process of Sn-sensitization and Ag-activation can be employed on ITO surfaces. If successful, Sn-sensitization and Ag-activation of ITO surfaces will improve adhesion and electrical contact between the porous RSI and the substrate by uniformly nucleating metallic Sn and forming metallic bonds at the interface of the RSI and ITO.

This process of Sn-sensitization and Ag-activation are assumed to be translatable from glass to other surfaces, including ITO [52], [69]. Accordingly, Sn-sensitization

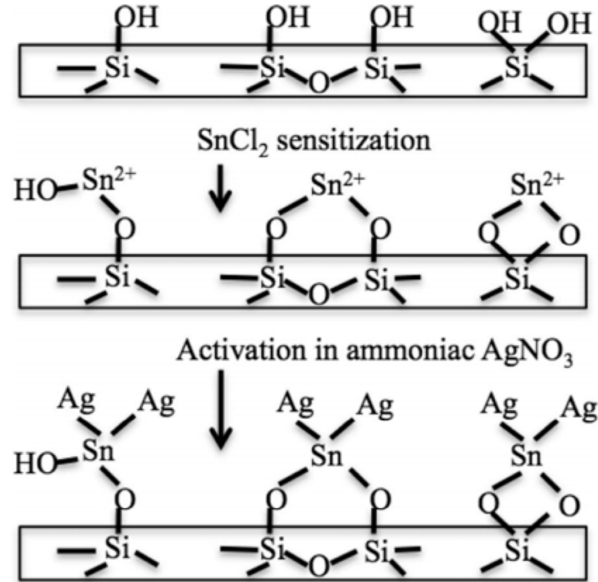

Figure 29. Sn-sensitization and Ag-activation on a glass surface. Taken from Wei and Roper [53].

and Ag-activation of a surface require several sequential procedures which can be broken down into 6 basic steps [52]:

1. Clean and hydroxylate the surface
2. Sensitize hydroxylated surface sites with Sn from $SnCl_2$ sensitization solution
3. Rinse to remove Cl-containing residue from sensitized surface
4. Activate sensitized sites with Ag from $AgNO_3$ activation solution
5. Rinse to remove particulate residue
6. Electrochemically deposit additional metal on activated surface

Following these steps above, the surface will be uniformly activated with catalytic sites for further deposition of metal. In our case, we aim to develop a printable Sn-sensitization solution, omitting steps 3 and 5 above. Furthermore, we aim to replace the $AgNO_3$-based Ag-activation solution with RSI. If successful, this modified process of Sn-sensitization and Ag-activation of ITO surfaces would create a chemical bond between the ITO surface and Ag in the RSI, improving ρ_c and adhesion. These steps and the processes responsible for Sn-sensitization and Ag-activation are used to develop a printable Sn-sensitization solution for ITO films, and will be described in detail in Chapter 4.3.

4.3 Development of a Printable Sn-Sensitization Solution for Indium Tin Oxide Thin Films

4.3.1 ***ITO Surface Cleaning & Hydroxylation***

The first step in the Sn-sensitization and Ag-activation process is to clean and hydroxylate the surface to be sensitized. Foremost, the substrate to be sensitized must be cleaned of any surface contaminants that will interfere with the sensitization process. For

soda-lime glass, this is done by cleaning with concentrated HNO_3 solution to remove the sodium ions shown by the following:

$$HNO_3 + H_2O \leftrightarrow NO_3^-(aq.) + H^+ \quad \text{Equation 4.1}$$

$$Na^+ + NO_3^-(aq.) \leftrightarrow NaNO_3 \quad \text{Equation 4.2}$$

This HNO_3 clean followed by immediate rinsing with D.I. water removes sodium nitrate from the surface and hydroxylates dangling bonds, leaving the surface as depicted in the top row of Figure 29 [52], [68].

To translate this process onto another surface, here ITO, we must analogously clean and hydroxylate the surface dangling bonds. ITO surfaces quickly adsorb atmospheric hydrocarbons, up to 20 at. % within hours of exposure to ambient atmosphere [70]. So first, hydrocarbon contaminants must be removed to ensure uniform sensitization of the surface. Typically, oxygen plasma treatments are employed to clean and even permanently modify ITO surfaces [70]–[73]. Oxygen plasma bombards the surface

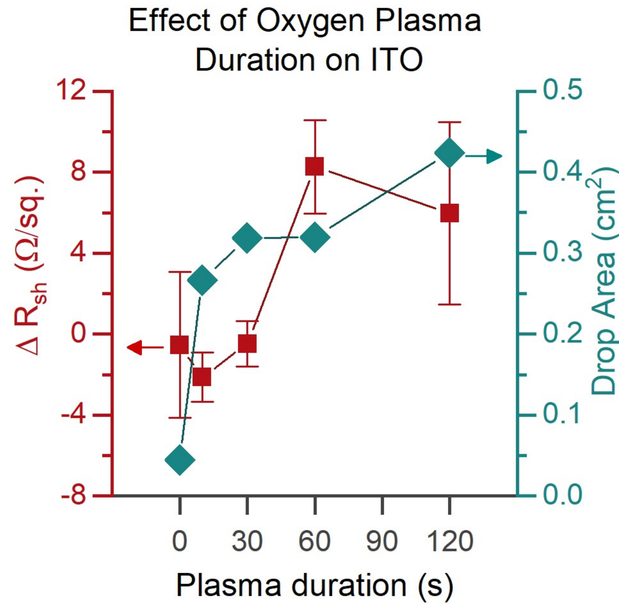

Figure 30. Effect of oxygen plasma duration on ITO sheet resistance, and droplet wettability on ITO films.

hydrocarbons with oxygen radicals, the oxygen radicals first eject the hydrocarbons, and after continued exposure, remove the top layer of the ITO film, leaving dangling bonds at the surface. However, extended exposure to oxygen plasma can significantly damage ITO [73].

Before moving past this first “clean” step of the process, the optimal oxygen plasma duration must be determined for the ITO films used in this work. Here, the optimal plasma duration is defined by two metrics; maximizing droplet wettability and minimizing change in sheet resistance of the ITO film. Oxygen plasma treatment of ITO effectively removes surface hydrocarbons, creating a more hydrophilic surface, resulting in significant increase in droplet wettability [73]. Thus, droplet wettability, or hydrophilicity of the ITO surface indicates effectiveness of hydrocarbon removal. If the ITO film is etched, the ITO sheet resistance will increase after plasma treatment. Thus, an increase in sheet resistance indicates over-exposure of oxygen plasma. Figure 30 shows the effect of oxygen plasma duration on the change in sheet resistance and droplet wettability of ITO films. Sheet resistance was measured before and after plasma cleaning in the same location using a 4-point probe. At 30 s of oxygen plasma exposure, the droplet area is at maximum before the sheet resistance increases, suggesting the cleanest surface prior to damaging or etching the ITO film.

Next, the clean ITO surface must be hydroxylated. So, following the oxygen plasma treatment, immediate immersion of the ITO in D.I. water rehydroxylates dangling bonds [71]. At this point, the surface of the ITO should resemble that of the top row of Figure 29, with the surface hydroxides acting as the sites for Sn-sensitization.

Again, here we aim to make several modifications of the traditional Sn-sensitization and Ag-activation process. Traditionally, Sn-sensitizations solutions were used by dipping glass substrates in Sn-sensitization solution baths, here we aim to develop a printable Sn-sensitization layer for ITO surfaces [52], [68]. Specifically, we aim to omit the rinse step typically employed between Sn-sensitization and Ag-activation. Second, Sn-sensitization solutions are typically made of $SnCl_2$ dissolved in D.I. water with HCl, this can be problematic for ITO films, which are etched by the high molar concentrations of HCl typically used in Sn-sensitization solutions [52], [74], [75]. Thus, formulation of the solution had to be determined based on several restraints:

i. Too much HCl will etch ITO films [76]
ii. Too little HCl will cause hydrolysis of $SnCl_2$ forming an insoluble salt [52]
iii. Too much $SnCl_2$ in solution will leave excess Sn- or Cl-containing residue blocking "sensitized" surface sites from subsequent Ag-activation

Furthermore, it is important to note that several assumptions are made with our modified Sn-sensitization process. These assumptions are:

i. The process of Sn-sensitization and Ag-activation on glass is translatable to ITO surfaces.
ii. The reduced HCl concentration (as described in Chapter 4.3.2) is sufficiently low enough to avoid etching the ITO surface.
iii. The Sn-sensitization solution can be printed prior to printing the Ag-activation solution, without the need to implement a rinse step in between.

Moving forward, these assumptions are used for initial investigations on the effects of the Sn-sensitization solution on ITO surfaces. The next chapter describes a first

approximation for Sn-sensitization solution formulation based on the above restrictions and a review of literature on optimizing $SnCl_2$ solutions.

4.3.2 ***Sn-Sensitization Solution Formulation: A First Approximation***

Now, a new printable Sn-sensitization solution formulation must be determined based on the restraints and assumptions discussed in the previous chapter. A review of literature on Sn-sensitization formulations suggested that the molar concentration of HCl must be at least twice that of $SnCl_2$ in solution to avoid hydrolysis of $SnCl_2$ and formation of an insoluble salt [52], [74], [77]. Thus, the minimum HCl molar concentration is set by the amount of $SnCl_2$ necessary to sensitize the surface. For our application on ITO films, our first approximation of Sn-sensitization solution formulation includes only enough $SnCl_2$ necessary to leave approximately one mono-layer of Sn on the surface.

In order to tune the concentration of $SnCl_2$ in solution, the volume of the solution printed over a given area must be known. In this study, a drop-on-demand printer with a 60 μm nozzle diameter was used, yielding droplets approximately 30 μm in diameter before spreading on the ITO surface. Here, the droplet is assumed to be spherical, so the volume of solution in a droplet is 14130 μm^3, or 1.413×10^{-11} L. The printed droplet is assumed to spread to 3× the droplet diameter on the ITO surface, covering a surface area of ~6300 μm^2 once printed. Using the atomic radius and molar mass of Sn (2.25×10^{-10} m, and 118 g/mol, respectively), the number of Sn atoms in a droplet to deposit a mono-layer was determined to be 3.9×10^9 Sn atoms, or 7.8×10^{-13} g of Sn. The molecular weight of $SnCl_2$ is 189.6 g/mol. Using the number of Sn atoms needed in 1 droplet, the molar concentration of $SnCl_2$ necessary was calculated as 0.46 mM $SnCl_2$ per liter of water, and the molar concentration of HCl is simply twice that of $SnCl_2$.

4.4 Properties of a Printed Sn-Sensitization Layer

In Chapters 4.4.1- 4.4.2, properties of ITO films treated with a printed Sn-sensitization solution are investigated. The initial hypothesis is that if the Sn-sensitization solution "sensitizes" the ITO surface, the Ag^+ ions in RSI will "activate", or bond, to the "sensitized" Sn sites on the ITO surface. Subsequently, Ag bonded to the ITO surface will act as a nucleation site for Ag^+ ion reduction and precipitation of metallic Ag [5]. If this is hypothesis is true, this would result in both:

i. Improved adhesion of RSI to ITO, and

ii. Improved specific contact resistance of RSI to ITO

To test this hypothesis, Chapter 4.4.1 details a qualitative investigation in adhesion of a printed Sn-sensitization layer. Then, Chapter 4.42 describes a study on of the specific contact resistance, ρ_c, of RSI on ITO with varying concentrations of Sn-sensitization solutions. As detailed in the previous chapter, the concentration of 0.46 mM $SnCl_2$ and 0.92 mM HCl is expected to deposit a mono-layer of Sn on the surface of ITO. Here, our initial investigations also included molar concentrations one order or magnitude above a mono-layer, and one order of magnitude below to help determine the relation between concentration of Sn-sensitization solution and properties of the ITO-RSI interface (adhesion and ρ_c).

4.4.1 Adhesion of a Printed Sn-Sensitization Layer

Qualitative scratch tests were performed to determine the effect of printed Sn-sensitization solutions on adhesion of RSI to ITO films. ITO films were deposited on glass slides by DC magnetron sputtering of a In_2O_3/SnO_2 (90/10 wt. %) target at 1kW power, under 3% O_2 flow, with a deposition pressure of 4 mTorr. Immediately prior to

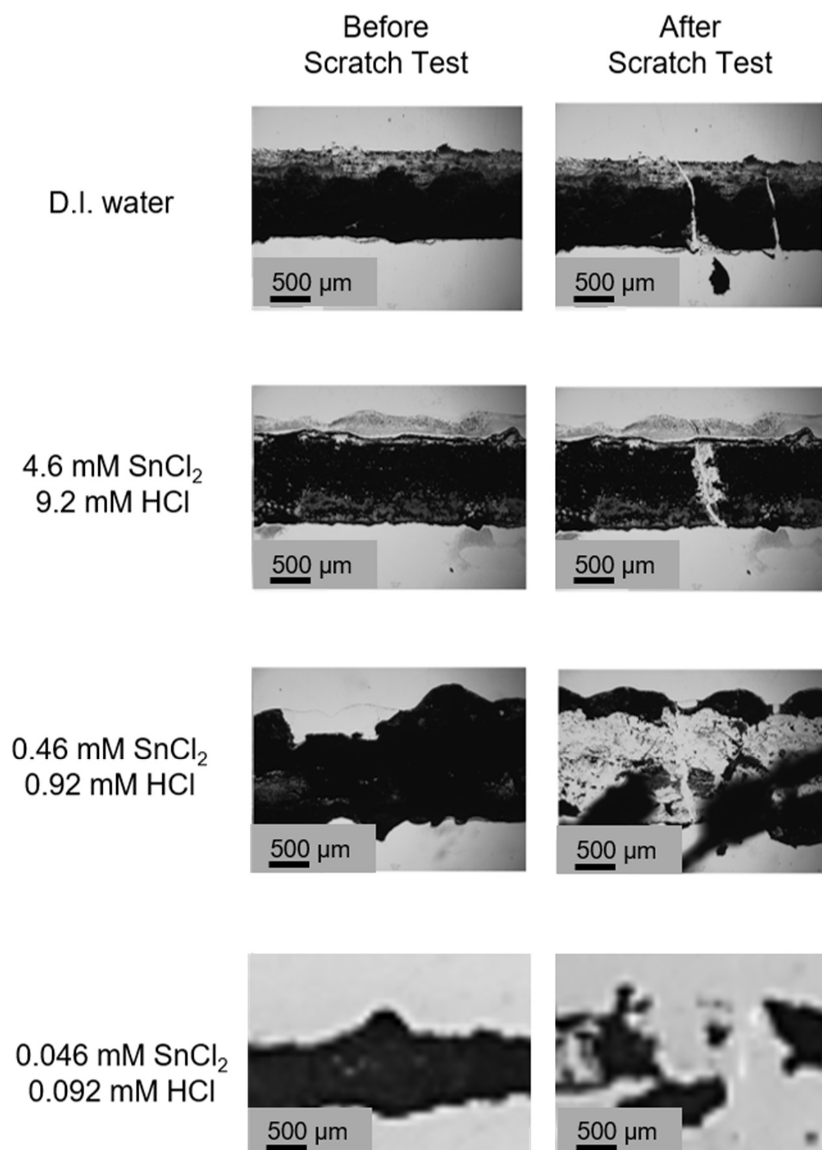

Figure 31. Top-down optical microscope images of RSI printed on ITO films with varying concentrations of a Sn-sensitization layer, before (left) and after (right) qualitative scratch tests. Top row shows a control with D.I. water printed prior to RSI printing.

Sn-sensitization solution printing, ITO films were oxygen plasma cleaned at 60 W for 30 s. Sn-sensitization solutions of varying compositions (see Figure 31) were printed on the ITO coated glass slides, allowed to dry fully before printing RSI directly on top of the Sn-sensitization layer. Scratch tests were performed by dragging a metal tweezer across

the printed RSI line. Although the force exerted on the fingers was not well controlled, it is clear that from Figure 31 that the Sn-sensitization solution did not significantly improve the adhesion of RSI to ITO, regardless of the concentration.

However, when this experiment was repeated, the results were inconsistent. Over several scratch tests, some RSI lines showed little adhesive failure, while other RSI lines had high adhesive failure. These initial findings lead us to develop a quantitative adhesion test to investigate the cause of variations in adhesion of printed RSI lines to ITO. These findings were described in detail in Chapter 4.1 and in a related publication [66]. Nonetheless, these qualitative scratch tests showed no significant improvement in adhesion of RSI to ITO with the use of the printed Sn-sensitization solutions for the concentrations investigated in this study. These results do not support the hypothesis defined in Chapter 4.4. To understand the reason for the lack of improved adhesion, the following chapters lay out a series of experiments used to determine the effects of Sn-sensitization solution on ITO surfaces.

4.4.2 Electrical Properties of a Printed Sn-Sensitization Layer

The previous work in Chapter 3.3.1 reports on ρ_c of RSI without a Sn-sensitization solution and Ag paste to ITO/Si in a SHJ cell. For the Ag paste, ρ_c values range from 4×10^{-3} to 10×10^{-3} $\Omega \cdot cm^2$, typical of those reported for Ag pastes [78]. The range of values for RSI fingers to ITO/Si is $1 - 60 \times 10^{-4}$ $\Omega \cdot cm^2$. On average, the RSI ρ_c values are one order of magnitude lower. The work in Chapter 3.3.1 suggested that where the interfacial contact area between the RSI Ag particles and ITO is larger, ρ_c is at the lower

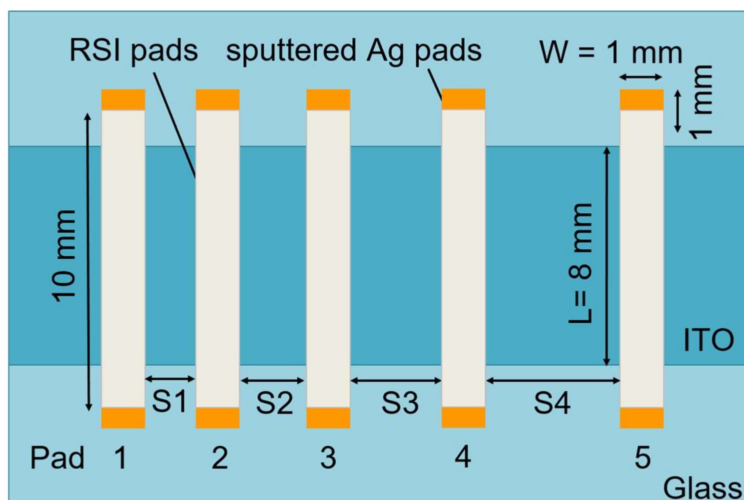

Figure 32. Schematic of TLM test structure used to determine specific contact resistance of RSI pads to ITO. S1, S2… are the spacing between adjacent RSI pads. The use of the evaporated Ag pads allows electrical probing without damaging RSI pads. Schematic is not drawn to scale.

end of the range reported, whereas fingers with less interfacial connectivity result in ρ_c in the higher end of the range.

In this chapter, specific contact resistance, ρ_c, of RSI on ITO with varying concentrations of Sn-sensitization solutions is investigated. As detailed in Chapter 4.3.2, the Sn-sensitization layer is printed from an aqueous solution of $SnCl_2$ and HCl with a constant ratio of 1 M to 0.5 M, respectively. However, such high concentrations (0.5 M) of HCl will etch ITO [79], and only a mono-layer of Sn or less is assumed to be necessary for improved adhesion and electrical contact [68]. Therefore, the concentration of the HCl and $SnCl_2$ were decreased to print only a mono-layer of Sn (see Chapter 4.3.2 for more details). To understand the electrical properties of a range of dilutions of the Sn-sensitization solution, the RSI/ITO interfacial specific contact resistance was characterized. The following concentrations of Sn-sensitization solutions were investigated: one mono-layer (0.46 mM $SnCl_2$, 0.92 mM HCl), and for one order of magnitude of concentrations above (4.6 mM $SnCl_2$, 9.2 mM HCl) and below the mono-

layer concentration (0.046 mM $SnCl_2$, 0.092 mM HCl). Samples with no Sn-sensitization layer were also measured for reference.

As illustrated previously in Figure 28, the sharp tips of electrical probes can damage RSI metallization during electrical characterization. So, before TLM could be performed, a transfer length method (TLM) test structure (schematic shown in Figure 32) was designed and fabricated to conduct TLM measurements without damaging the printed RSI pads. The test structure consists of 5 sets of parallel sputtered Ag pads (1 ×1 mm^2) straddling a strip of ITO; the electrical probes are placed on the evaporated Ag pads to avoid physical contact and possible damage of RSI pads during electrical measurements. ITO (~80 nm, ~80 Ω/□) and the sputtered Ag pads (~300 nm, ~0.05 Ω/□) were DC magnetron sputtered by Materials Research Corporation 944 sputtering system with an In_2O_3/SnO_2 (90/10 wt. %) target at 1kW power, under 3-4% O_2 flow, with a deposition pressure of 4 mTorr. A series of RSI pads were printed on these TLM test structures. The RSI used in these experiments was prepared following a procedure described in detail elsewhere [45]. The RSI was diluted 1:1 by volume with ethanol and printed on substrates heated to 66 °C. RSI pads were printed 2-layers thick, with equal droplet diameter; this means the amount of Ag per pad was kept constant for all lines.

Prior to TLM measurements, each RSI pad was measured by 4-wire resistance measurements to verify that the resistances were similar for all pads in the test structure. Application of the TLM method requires that the resistance of each metal pad is equal, and the pad width to be sufficiently large compared to the transfer length [80], [81]. Transfer lengths on the order of 10s of microns were assessed in previous work

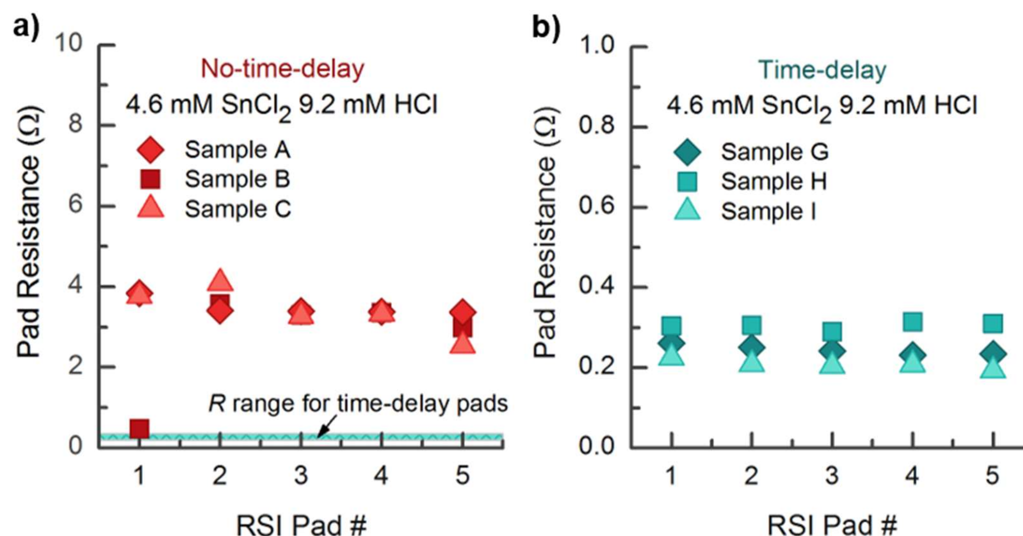

Figure 33. Resistance of each RSI pads printed with the same concentration of Sn-sensitization solution. Pad resistances of three samples with no-time-delay between printing layers (a), and pad resistances from three samples with time-delay between layers (b). Note that the pad resistance scales vary by an order of magnitude. Consistent, low resistance values are shown for each RSI pad when a time-delay (b) is employed, this range in indicated by the blue region in (a). These measurements are done prior to TLM; consistent pad resistance values are a requisite for determining specific contact resistance values using the TLM method.

(Chapter 3.3.1), sufficiently less than the 1 mm width of the RSI pads in the TLM test structure.

If the resistance of each printed pad is not the same, then the contribution to the interfacial resistance between the RSI and ITO will be convoluted. Chapter 3.2.2 describes in more detail instances where RSI lines with the same amount of Ag show quite different resistances as a result of whether the previous layer was allowed to react and dry fully before printing additional layers. This is again exemplified in this experiment, showing the importance of reaction kinetics in the electrical properties of RSI metallizations. Figure 33 shows resistances of each RSI pad in a set of TLM samples with equal concentration of the Sn-sensitization solution, but varied time between printing the 2nd layer. Figure 33 (a) shows pads printed with no-time-delay between printing the 2nd layer, showing the

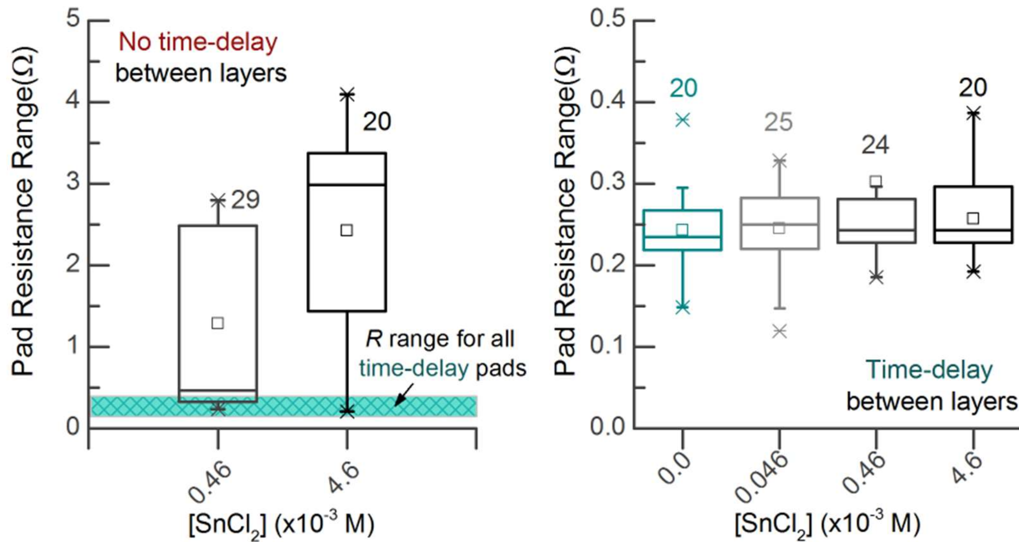

Figure 34. Boxplots showing the range of RSI pad resistances for varying Sn-sensitization solution concentrations, and for pads printed with no-time-delay between layers (left) and for pads that were allowed to dry before printing additional layers (right). This shows that the resistance varies significantly when the ink is not allowed to dry before printing additional layers. Also, this shows that the resistance of the RSI pad does not change with increasing Sn-sensitization solution concentration. The numbers above each box indicate the number of samples. [HCl] molar concentration is twice that of [$SnCl_2$].

resistance of RSI pads varies significantly from < 1 Ω to nearly 4 Ω from one pad to the next; Figure 33 (b) shows pads that were allowed to dry fully before printing the 2nd layer, showing consistent, low resistance values between 0.20-0.35 Ω for pads with time delay. Figure 34 summarizes the pad resistances for all TLM samples for varying concentration of the Sn-sensitization solution with no-time-delay (left) and time-delay (right) between printing additional layers. Furthermore, Figure 34 shows that the changing concentration of $SnCl_2$ and HCl in the Sn-sensitization does not alter the electrical properties of the RSI pad. After verification of low and similar resistance values for each pad, the resistance between adjacent pads must be measured to determine the specific contact resistance between RSI and ITO.

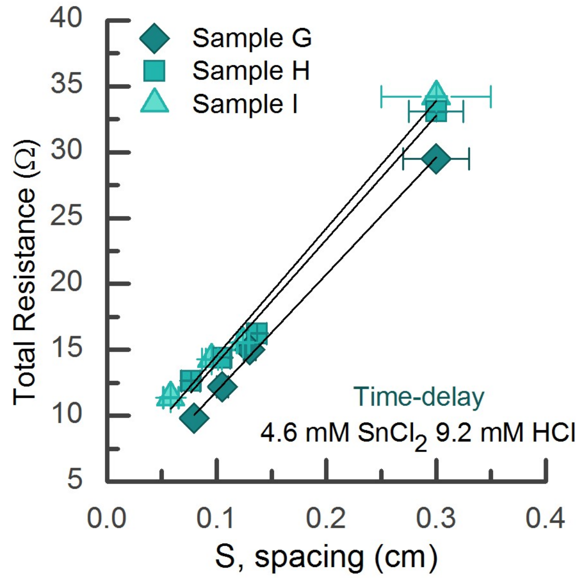

Figure 35. An example of TLM results showing the resistance between adjacent RSI pads as a function of pad spacing. The trend lines, which are well-fitted with the data points, are used to extrapolate the specific contact resistance.

Next, TLM measurements were carried out to determine how the concentration of Sn-sensitization solution ($SnCl_2$ adhesion promoting layer) affects the specific contact resistance of RSI to ITO. TLM measurements are employed by sourcing a current between two adjacent pads through an isolated path, measuring the voltage drop across the same path, and repeating for varied spacing between adjacent pads. Current flows through the isolated path in the TLM test structure; from one evaporated Ag pad, to the RSI pad, through the RSI/ITO interface, through the sheet of ITO; the voltage drop between adjacent pads is measured as a function of spacing (denoted by S1, S2... in Figure 32). The total resistance, R_{Total}, measured between adjacent pads is:

$$R_{Total} = 2R_{metal} + 2R_{interface} + R_{semi} \quad \text{Equation 4.3}$$

where R_{metal} is the resistance of the metal pad, $R_{interface}$ is the interfacial contact resistance, and R_{semi} is the resistance of the layer under the metal pad. Resistivity of the

evaporated Ag pads is 1.6 μΩ·cm and at ~300 nm in height, the resistance contribution from the Ag pad is assumed to be equal and is less than 0.05 Ω. This is less than 20% of the total resistances measured for all RSI pads in this experiment. The resistance contribution from the portion of the RSI pad that is on the glass, before it conducts through the ITO is ~ one-tenth of the resistance from the whole RSI pad. Contributions from the sputtered Ag and RSI pads are comparable from samples to sample. Thus, results presented here assume that the resistance contributions from the metal ($2R_{metal}$) are negligible, and standard TLM method is applied to determine whether the specific contact resistance is changing with increasing concentration of the Sn-sensitization solution. An example of TLM data is shown in Figure 35 for three samples with the same concentration of the Sn-sensitization solution.

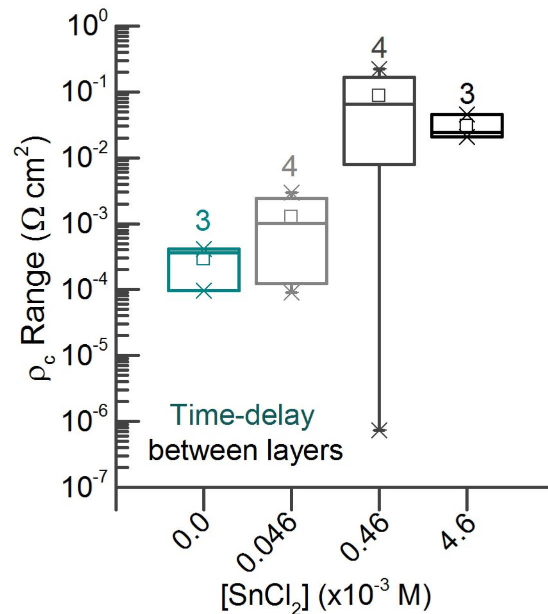

Figure 36. Boxplot of specific contact resistance range for all TLM samples prepared with varying concentrations of Sn-sensitization solution. The numbers adjacent to each box is the total number of samples represented in the boxplot. [HCl] molar concentration is twice that of [$SnCl_2$].

Figure 36 shows a boxplot of ρ_c values determined from TLM for all measured samples. On average, as the concentration of Sn-sensitization solution increases, ρ_c of the interface between RSI and ITO increases. RSI printed without the Sn-sensitization solution has ρ_c of ~1 $\times 10^{-4}$ $\Omega \cdot cm^2$, within the range reported previously for RSI to ITO/Si in Chapter 3.1.1 [54].

Again, the initial hypothesis for these experiments is: If Ag is bonded the ITO surface through Sn-sensitization and Ag-activation, Ag bonded to the surface will act as a nucleation site for Ag+ ions in RSI, creating a chemical bond between the ITO surface and Ag in the RSI, resulting in improved specific contact resistance and adhesion of RSI to ITO. These initial experiments described in Chapters 4.4.1-4.4.2 determined that both the adhesion and the specific contact resistance are not improved with all concentrations of Sn-sensitization solution investigated. These results suggest that some of the initial assumptions made for the Sn-sensitization and Ag-activation process are not valid. The following chapters detail a series of experiments to understand which of these assumptions were invalid, and which parts of the Sn-sensitization and Ag-activation process may not be translatable from glass to ITO surfaces.

4.4.3 The Effect of Sn-Sensitization Solutions on Work Function of ITO

In the previous chapters, one assumption that was made was that the process of Sn-sensitization and Ag-activation on glass is translatable to ITO surfaces. That is, if the Sn-sensitization process is occurs on ITO, the surface should be modified by Sn bonding to surface hydroxide sites. None of the characterization techniques used in Chapters 4.1-4.4.2 are sensitive enough to determine if surface of the ITO has been modified through the Sn-sensitization process.

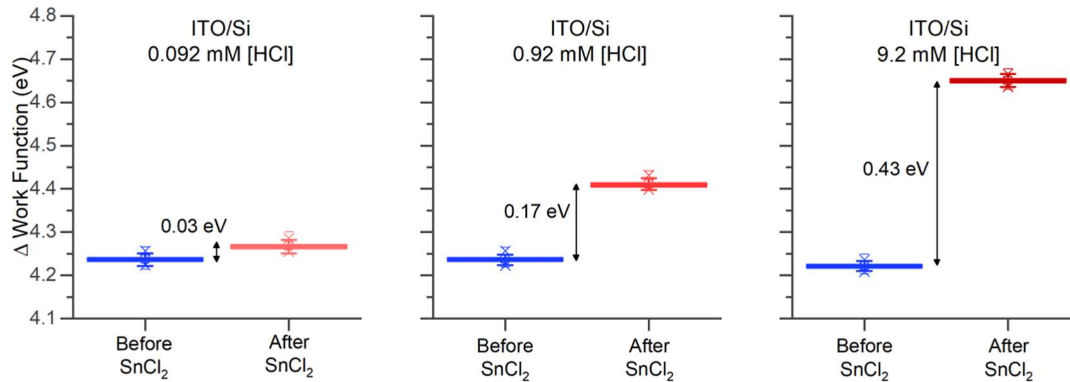

Figure 37. Relative change in work function of ITO films before and after treatment with Sn-sensitization solutions of varying concentrations ([$SnCl_2$]: [HCl] is 1:2). Note that actual work function is not accurate for measurements conducted in ambient atmosphere due to modified surface termination of reference sample.

Kelvin probe is a technique that is highly sensitive to surface modification [82]. This technique measures the contact potential difference (CPD) between two surfaces that are brought close together. The work function of the sample (WF_{sample}) can be measured using the work function of the Kelvin probe and of a known material such as Au (WF_{probe}, and WF_{Au}, respectively), and measured CPD following the equations below:

$$WF_{probe} = WF_{Au} - CPD \qquad \text{Equation 4.4}$$

$$WF_{sample} = WF_{probe} - CPD \qquad \text{Equation 4.5}$$

To our knowledge, the modification of ITO surfaces before and after bonding of one mono-layer of Sn is not documented in literature. However, using Kelvin probe measurements, we can determine the change in CPD before and after ITO is treated with Sn-sensitization solutions; indicating whether the surface electronic structure is modified.

Figure 37 shows the surface work function of three ITO samples before and after pipetting Sn-sensitization solutions of varying concentrations. All three ITO samples start with surface work functions of approximately 4.2 eV, which is ~0.5 - 0.2 eV lower

than typical values reported in literature [83], [84]. The ITO surface work function was determined by measuring 500 points across the surface before and after exposure the the Sn-sensitization solutions, following Equations 4.4 and 4.5. The most accurate way to determine accurate work function is to use a freshly Ar^+ plasma cleaned standard material (such as Au, or highly oriented pyrolytic graphite), and to carry out Kelvin probe measurements under vacuum. Here, we attribute the discrepancy between the ITO work function in our samples and those reported in literature is expected to be from using Au reference material in ambient atmosphere. Nevertheless, all three ITO samples show the same work function prior to exposure to Sn-sensitization solutions. The metric used to indicate change in ITO surface modification is change in ITO work function.

Next, Sn-sensitization solutions were applied to the three ITO-coated samples. 5 µL droplets were pipetted on the ITO surface, the solution was left on the ITO until fully dried before measuring the CPD of the ITO surface again. This was done to simulate the way in which the Sn-sensitization solution would be printed and allowed to dry prior to RSI printing. The following concentrations of Sn-sensitization solutions were investigated: one mono-layer (0.46 mM $SnCl_2$, 0.92 mM HCl), and for one order of magnitude of concentrations above (4.6 mM $SnCl_2$, 9.2 mM HCl) and below the mono-layer concentration (0.046 mM $SnCl_2$, 0.092 mM HCl).

For the 0.092 mM HCl Sn-sensitization solution, there is a small increase in work function of 0.03 eV. For the 0.92 mM HCl solution, a larger increase in work function (0.17 eV) is observed. Finally, for the 9.2 mM HCl solution, the largest decrease of 0.43 eV is shown. This increase in ITO surface work function as Sn-sensitization solution concentration increases suggests that the surface is modified, however from this

experiment alone it cannot be confirmed whether the surface modification is from Sn atoms bonding to the ITO surface, or from increasing amounts of particulate residue accumulating on the ITO surface.

*4.4.4 **The Effect of HCl Concentration on ITO***

Another assumption for Sn-sensitization of ITO surfaces was that the HCl concentration was sufficiently low to avoid etching the ITO surface. Sn-sensitization solutions of varying concentrations were prepared to determine the effects of $SnCl_2$ and HCl molar concentrations on ITO films. Profilometry was used to determine if the ITO film is etched, and/or the Sn-sensitization solution leaves residual particles accumulated around the outer region of the droplet.

If the ITO film is etched, it is possible that the Sn-sensitized surface is etched away. If residual particles from the Sn-sensitization solution are accumulated on top of the ITO surface, it is possible that the residue creates a physical barrier for Ag-activation on the ITO surface. These results could, in part, explain the decrease in ITO surface

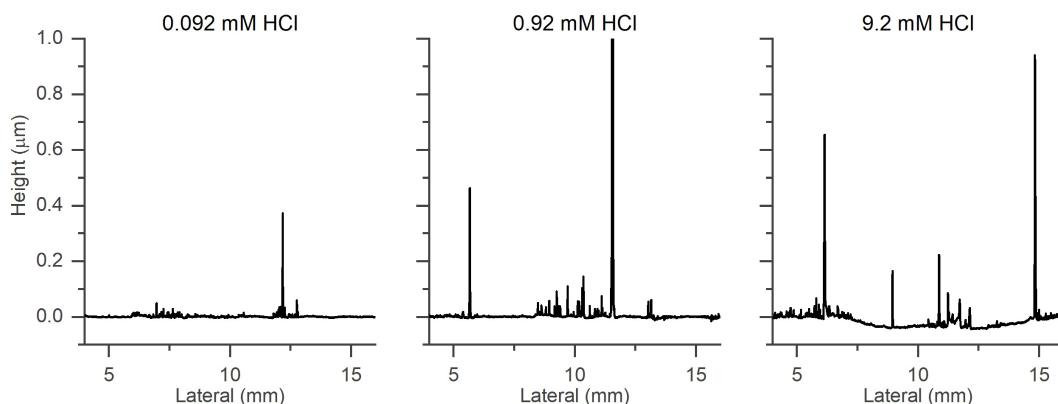

Figure 38. Profilometry of ITO films after pipetting Sn-sensitization solutions with varying concentrations of $SnCl_2$ and HCl ([$SnCl_2$]: [HCl] is 1:2).

work function with increasing Sn-sensitization solution concentration (Chapter 4.4.3), and variable adhesion performance (Chapter 4.4.1) and increased ρ_c.(Chapter 4.4.2).

The following concentrations of Sn-sensitization solutions were investigated: one Sn-mono-layer (0.46 mM $SnCl_2$, 0.92 mM HCl), and for one order of magnitude of concentrations above (4.6 mM $SnCl_2$, 9.2 mM HCl) and below the mono-layer concentration (0.046 mM $SnCl_2$, 0.092 mM HCl). Immediately prior to pipetting Sn-sensitization solution, ITO films were oxygen plasma cleaned at 60 W for 30 s. Then, 2 µL droplets of each Sn-sensitization solution concentration were pipetted on to separate ITO films and allowed to dry. Next, using a Dektak XT stylus profilometer, profilometry was done across the dried droplet region to measure vertical displacement across the smooth ITO film surface, indicating either particulate accumulation, and/or etch depth.

Figure 38 shows the profiles across the droplet region for the different concentrations of Sn-sensitization solutions. The ITO film with lowest concentration Sn-sensitization solution (0.046 mM $SnCl_2$, 0.092 mM HCl) shows the ITO film did not measurably etch beyond the surface roughness of the clean ITO film. However, particulate accumulation near the outer edge of the droplet is still visible, indicating that either a small amount of ITO was etched and transported to the droplet edge during evaporation, or that there are residual particles that did not bond to surface sites nor evaporate. The mono-layer concentration Sn-sensitization solution (0.46 mM $SnCl_2$, 0.92 mM HCl) shows similar results, with more particulate accumulation near the droplet edge region. However, the highest concentration Sn-sensitization solution (4.6 mM $SnCl_2$, 9.2 mM HCl) shows

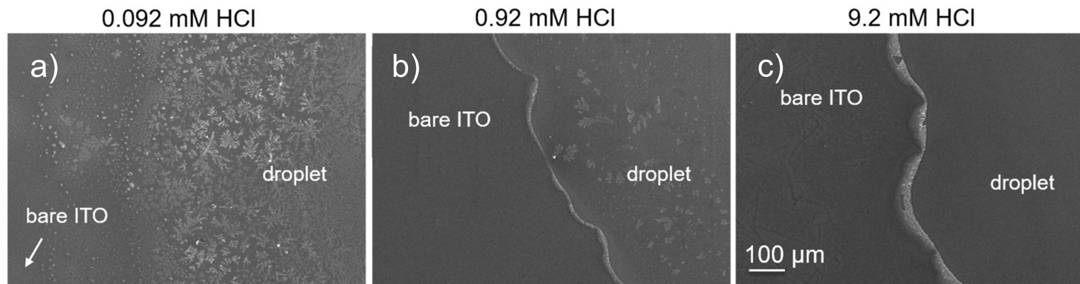

Figure 39. SEM images of ITO films with Sn-sensitization solutions of varying concentrations pipetted on the surface and allowed to dry fully prior to imaging. a) 0.046 mM $SnCl_2$, 0.092 mM HCl, b) 0.46 mM $SnCl_2$, 0.92 mM HCl, and c) 4.6 mM $SnCl_2$, 9.2 mM HCl.

~40 nm of the ITO film is etched. For reference, ITO films on SHJ devices are ~75 nm thick, so 40 nm of etching is significant and should be avoided for use on devices [30].

Taking a closer look at the effects of Sn-sensitization solutions on ITO films, Figure 39 shows SEM images of ITO films with pipetted Sn-sensitization solutions with the same concentrations as those shown in Figure 38. For the two lower concentration Sn-sensitization solutions (Figure 39 (a) and (b)) dendritic particles are visible inside of the droplet region whereas the highest concentration Sn-sensitization solution (Figure 39 (c)) does not show any particulate accumulation inside of the droplet region. The two higher concentration Sn-sensitization solutions show well-defined droplet edge regions. Again, from Figure 38, it is evident that the highest concentration Sn-sensitization solution (4.6 mM $SnCl_2$, 9.2 mM HCl) etches the ITO surface significantly. The etched surface in Figure 39 (c) shows no accumulated particles are visible inside of the droplet region, only at the edge. If the ITO is not etched (as for the 0.092 and 0.92 mM HCl Sn-sensitization solutions), there is still particle residue shown throughout the inside of the droplet region (Figure 39 (a) and (b), respectively).

This might explain previous results that show no improvement of adhesion of RSI to ITO, and an increase in ρ_c when using Sn-sensitization solutions. The 0.092 and 0.92 mM HCl Sn-sensitization solutions show particles covering the ITO surface in the droplet region. If the ITO surface is sensitized, this particulate residue would cover and block Ag-activation on the sensitized sites on the ITO surface. For the higher concentration 9.2 mM HCl Sn-sensitization solution, the ITO film is measurably etched. So, even if the ITO is sensitized, it is possible the sensitized ITO surface is etched away. In summary, HCl concentrations of 0.092-0.92 mM HCl do not measurably etch ITO, but particles accumulate on the ITO surface; These results presented thus far in Chapter 4 suggest:

a. that the first-approximation at Sn-sensitization solution concentrations (detailed in Chapter 4.3.2) might be based on incorrect assumptions leading to higher-than-mono-layer coverage; and/or

b. a rinse step is necessary to remove any remaining residue from the sensitized surface.

Still, data discussed thus far does not validate or invalidate whether the ITO surface is sensitized by the Sn-sensitization solution in the same way a glass surface is sensitized.

*4.4.5 **The Effect of Rinsing Sn-Sensitization Solution from Indium Tin Oxide Surface***

Another assumption that was made for a printable Sn-sensitization solution was that Sn-sensitization solution can be deposited prior to printing the Ag-activation solution, without the need to implement a rinse step in between. Chapter 4.4.3 showed that for dried Sn-sensitization solution droplets on ITO, as Sn-sensitization solution concentration increases, ITO work function decreases. However, Chapter 4.4.4 showed that as Sn-

sensitization solution concentration increases either particulate residue accumulates on the ITO surface, or ITO is etched, indicating that the change in work function is not necessarily due to Sn-sensitization of the ITO surface.

Here, we investigate the effect of Sn-sensitization solutions on the change in surface contact potential difference (CPD) of ITO before and after removing particulate residue left on the ITO surface. This is done by using a Kelvin probe to map CPD values across ITO films treated with Sn-sensitization solutions before and after removing particulate residue. Note that change in CPD is equivalent to change in surface work function (see Equations 4.4 and 4.5). The objective of this experiment is to understand whether ITO surface is modified by the Sn-sensitization solution.

Figure 40 details an experiment used to determine whether the surface bonding is modified by Sn-sensitization solutions, or if it is only temporarily modified by accumulation of residue on the surface. Again, the same concentrations of Sn-sensitization solutions were investigated as in Chapters 4.4.1-4.4.4: one Sn-mono-layer (0.46 mM $SnCl_2$, 0.92 mM HCl), and for one order of magnitude of concentrations above (4.6 mM $SnCl_2$, 9.2 mM HCl) and below the mono-layer concentration (0.046 mM $SnCl_2$, 0.092 mM HCl).

A set of ITO films were oxygen plasma cleaned for 30 s at 60 W to remove any non-uniform contamination across the sample set before storing in ambient atmosphere. Based on previous trials in our laboratory and work by Lok *et al.*, after 48 h of storage in ambient atmosphere, ITO surface modification from the plasma clean is worn off and the ITO films are all uniformly contaminated with atmospheric hydrocarbons [85]. After 48 h of storage in ambient atmosphere, CPD maps were

measured on the ITO films by Kelvin probe. Then, ITO films were oxygen plasma cleaned for 30 s at 60 W immediately prior to pipetting Sn-sensitization solutions of varying concentrations onto the ITO films and allowed to dry. As a control, one ITO film was treated by pipetting D.I. water rather than Sn-sensitization solution. After drying. CPD maps were measured over the same region on the ITO films. Note that the "dried-droplet" CPD measurements occurred ~20 minutes following the oxygen plasma treatment and solution deposition. Then, the ITO films were rinsed thoroughly with pressurized D.I. water for 2 min and dried with nitrogen. Finally, another round of CPD maps were measured over the same region of the ITO films.

Figure 41 shows the CPD maps of ITO films before, and after pipetting and drying Sn-sensitization solutions, and after thoroughly rinsing off remaining particulate residue. The top row shows the as-deposited ITO surface is relatively uniform with an average CPD value ~ 440 meV. After ~48 h of exposure to ambient atmosphere the oxygen-plasma surface modification has worn off completely, but the ITO films are left with comparable surfaces for subsequent Sn-sensitization solution application [85].

The middle row of Figure 41 shows the CPD maps of the ITO films with dried Sn-sensitization solution droplets. The ITO films surrounding the dried droplet regions have an average CPD value of ~ 600 meV, this is 160-200 meV higher than the as-deposited ITO films (shown in the top row of Figure 41). This 160-200 meV increase in CPD of the surrounding ITO film is attributed to the residual effects of the oxygen plasma done prior to pipetting solutions and allowing to dry. Others have reported on the effects of oxygen plasma treatments on ITO surface work function; oxygen plasma treatment can increase or

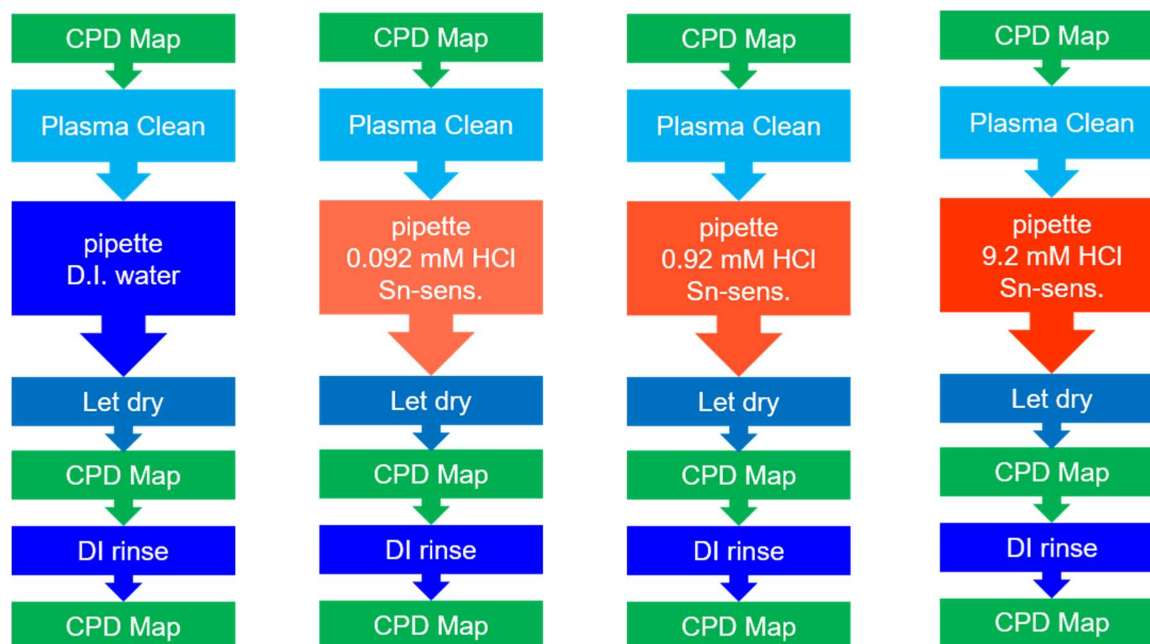

Figure 40. Schematic showing processing steps for an experiment to determine the effect of Sn-sensitization solutions on the change in work function of ITO surfaces, before and after rinsing away particulate residue. [HCl] molar concentration is twice that of [$SnCl_2$].

decrease ITO surface work function between 40-300 meV depending on plasma power and duration, removal of surface species, and exposure duration to ambient atmosphere [71], [84]–[86].

Inside of the dried-droplet regions (middle row, Figure 41), there is a decrease in CPD (corresponding to an increase in surface work function) measured between the Kelvin probe tip and the dried droplet region as the concentration of Sn-sensitization solution increases. For the ITO film with pipetted and dried D.I. water, there is a slight decrease in CPD of ~40 meV in the dried droplet region. This decrease of ~40 meV is attributed to cleaning and rehydroxylating of dangling bonds on the ITO surface and is explained by the following: i) Oxygen plasma treatment modifies the ITO surface predictably, decreasing the surface work function by 40-50 meV [71], [84], and ii) immediately following the oxygen plasma treatment, ITO was rehydroxylated in the

D.I. water droplet region, which is evident by this ~40 meV CPD change from the droplet area to the surrounding ITO film [71].

The middle row of Figure 41 also shows change in CPD values (change in work function) in the dried-droplet regions for ITO films treated with Sn-sensitization solutions. The change in CPD values for the 0.092, 0.92, and 9.2 mM HCl Sn-sensitization solutions are -310, -435, and -750 meV, respectively. This shows that as the concentration of Sn-sensitization solution increases, the surface work function of the dried droplet region on ITO increases.

The bottom row in Figure 41 shows the same regions of the ITO films after rinsing off particulate residue from the dried droplets. Interestingly, the CPD maps show similar results for each of the ITO films treated with Sn-sensitization solutions. Whereas, the ITO film treated with a D.I. water droplet shows no evident change in CPD in the droplet region.

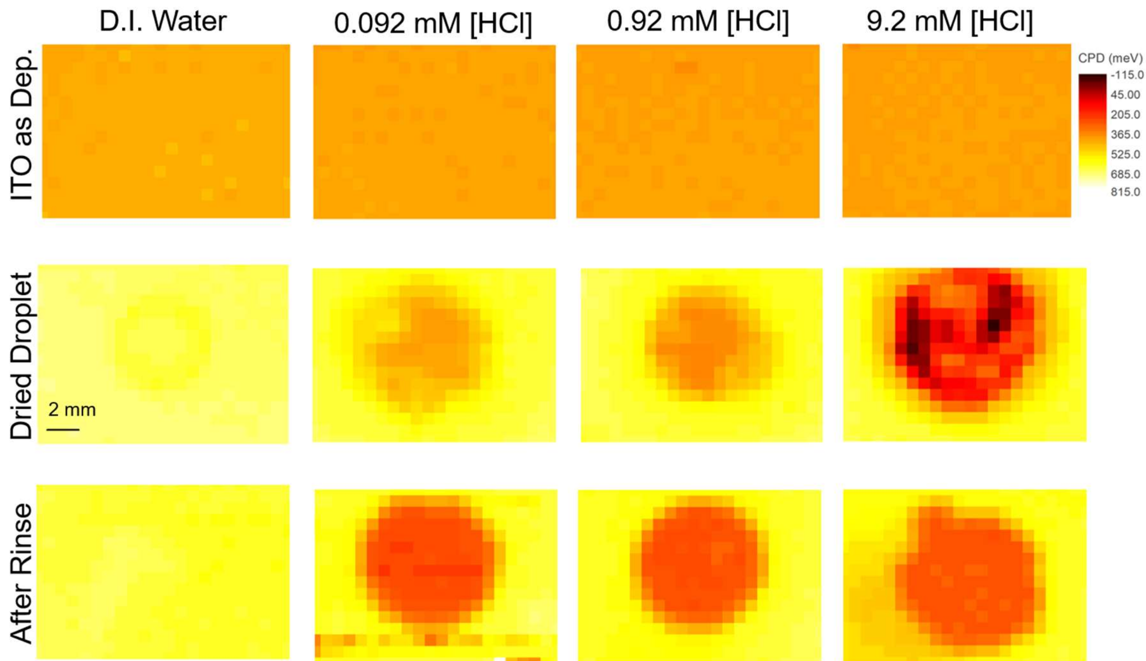

Figure 41. CPD maps of ITO films as deposited (top row), after pipetting D.I. water or Sn-sensitization solution (middle row), and after thoroughly rinsing off particulate residue (bottom row), showing the effect of Sn-sensitization solutions on the ITO surface work function. [HCl] molar concentration is twice that of [$SnCl_2$].

The CPD values are approximately equal for droplet regions across all three concentrations of Sn-sensitization solutions, suggesting the ITO surface is modified by all three concentrations of Sn-sensitization solutions investigated.

Furthermore, these results suggest that the change in CPD over the dried droplet region (middle row, Figure 41) is due to accumulation of residue on the surface, and that more residue accumulates for higher concentration solutions. Based on these results, we suggest that the ITO surface is modified by Sn-sensitization solutions, even for low HCl (and $SnCl_2$) molar concentrations that do not etch ITO films. However, it is evident that for the Sn-sensitization solution concentrations investigated here, a rinse step is necessary in between Sn-sensitization and Ag-activation to remove particulate residue from the ITO surface

4.5 Tin Sensitization and Silver Activation on Indium Tin Oxide

Historically, Sn-sensitization and Ag-activation were frequently used to improve uniformity and adhesion of Ag mirrors on glass substrates [68]. In this work, Sn-sensitization and Ag-activation were investigated as a potential method to improve adhesion and specific contact resistance of RSI to ITO surfaces. The sensitization and activation processes on glass are assumed to be the same on other surfaces, such as epoxies, and even ITO [87], [88]. However, at this time, there are few publications that have looked into Sn-sensitization on ITO, and none examine the damage done to ITO as a result of HCl concentration in the sensitization solution [75], [87].

Chapter 4.3 described an attempt at developing a printable Sn-sensitization solution to improve adhesion and specific contact resistance of RSI on ITO without etching ITO films. However, in Chapter 4.4, it was observed that the printed Sn-sensitization layer

did not improve adhesion nor specific contact resistance of RSI on ITO. Chapter 4.4.3-4.4.5 detailed a series of experiments to test assumptions that were made while developing this Sn-sensitization layer. It was evident from these experiments that Sn-sensitization solutions modified the ITO surface, even for Sn-sensitization solutions with sufficiently low HCl molar concentrations that do not measurably etch ITO films. However, it was not clear whether the process of Sn-sensitization and Ag-activation is translatable from glass surfaces, as used historically, to ITO surfaces. In this study, we investigate the process of Sn-sensitization and Ag-activation on indium tin oxide (ITO)—a dominant transparent conducting oxide used in optoelectronic devices. The main findings of this study are summarized below, the study is reported in full detail published elsewhere [89].

This work is relevant outside of the application to next generation photovoltaics as well; Transparent conducting oxides (TCO) are widely employed in flat panel displays, smart windows, and thin-film solar cells among numerous other optoelectronic devices [73], [75], [90], [91]. Tin doped indium (ITO) is the dominant TCO used in such devices due to ease of deposition, high conductivity, carrier concentrations, and

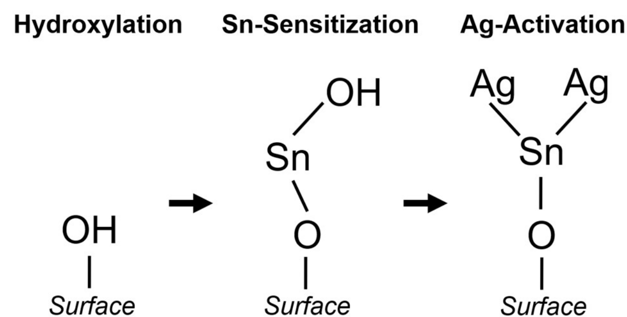

Figure 42. Simplified schematic showing the steps for Sn-sensitization and Ag-activation of a glass or ITO surface.

transparency [91]. Bonding and adhesion of metals-to-oxides is inherently poor, and results in uniformity and durability challenges [69], [92], [93].

Figure 42 shows a simplified schematic of the Sn-sensitization and Ag-activation process. This process of sensitization and activation of oxide surfaces has been used for decades mainly for the purposes of improving adhesion and uniformity of silver films to glass [67], [94], [95]. Multiple in-depth studies have thoroughly characterized the mechanisms behind this process of Sn-sensitization and subsequent activation on glass surfaces [67], [94], [95]. However, the sensitization and activation processes on glass are suggested to be the same on other surfaces, such as epoxies, and even ITO , but have not been detailed thoroughly [87], [88].

As discussed in Chapter 4.4.4, Sn-sensitization solutions in molarities reported in literature can etch ITO films [67], [76], [87]. At this time, only two studies have looked into Sn-sensitization on ITO, and neither have examined damage done to ITO as a result of high HCl concentration in the sensitization solution [75], [87].

The mechanisms of Sn-sensitization and Ag-activation on glass rely on a multistep process which are described elsewhere in full detail by Wei and Roper [67]. These steps are as described in detail in our publication and in Chapter 4.2 [89]. The three main steps are summarized in Figure 42 as 1) hydroxylation of the surface, 2) Sn-sensitization, and 3) Ag-activation. It is important to note that surface -OH sites react with the Sn-sensitization solution, leaving Sn^{2+} ions on the surface [67], [94]. Accordingly, successful Sn-sensitization of a surface will result in an increased Sn concentration at the surface, specifically Sn^{2+} [68], [96], [97]. Here, successful

hydroxylation of the Sn, bonded to the surface is what is commonly known as "sensitization".

The 3rd step of the process (Ag-activation) relies on the Ag ions in the activation solution reacting with the Sn^{2+} following [68], [96], [97]:

$$Sn^{2+} + 2Ag^{+} \leftrightarrow Sn^{4+} + 2Ag \quad \text{Equation 4.6}$$

Successful Ag-activation will results in 2 Ag^{+} ions from solution reduce into metallic Ag bonded to a Sn^{4+}. In this study, we treat ITO surfaces with Sn-sensitization and Ag-activation solutions, and compare compositional changes in ITO surfaces throughout these steps through X-ray Photoelectron Spectroscopy (XPS) and compare to surface composition to that of glass.

ITO films were prepared and treated with Sn-sensitization solutions of varying concentrations. All Sn-sensitization solutions had HCl molar concentrations twice that of $SnCl_2$ in order to avoid hydrolysis of the $SnCl_2$ in the solution. Ag-activation solutions were prepared following de Minjer *et al.* [68].

Prior to all surface treatments, ITO films were cleaned with an oxygen plasma for 30 s at 60 W following the optimization shown in Chapter 4.3. Immediately following plasma treatment, individual samples were thoroughly rinsed in D.I. Sn-sensitization solutions were pipetted on the ITO surface before rinsing again in D.I. water. Then Ag-activation process was done by submerging the sample in Ag-activation solution. Last, the final rinse was done in D.I. water held between 90- 95 °C then dried with a nitrogen gun. ITO surface composition was measured by 4 X-ray photoelectron spectroscopy (XPS).

Sn-sensitization solutions reported in literature have HCl concentrations varying orders of magnitude from 0.001 – 9M HCl [67], [68], [94], [96]. First, sheet resistance of ITO

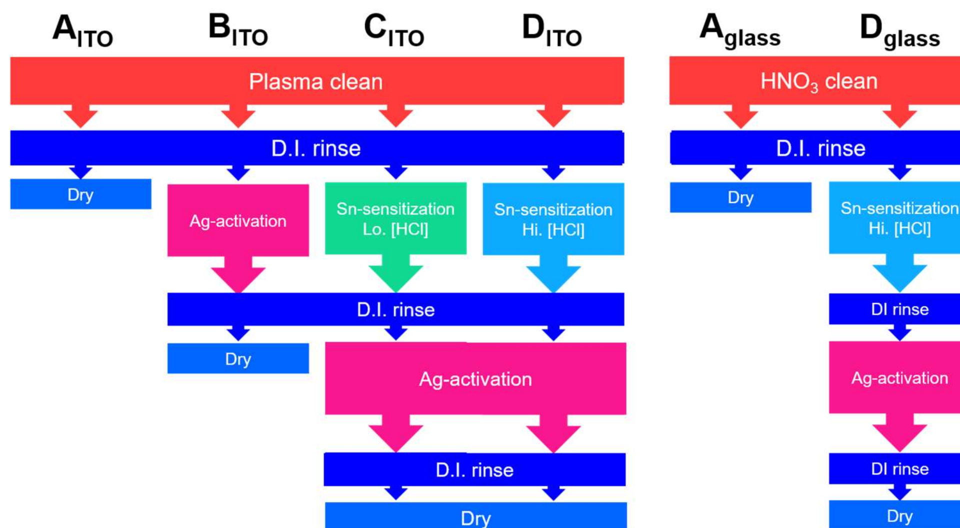

Figure 43. Schematic showing samples ITO and glass samples prepared for XPS study.

films was measured before and after exposure to HCl in varying concentrations (Figure 43) to determine concentrations which damage ITO films used in this study by etching. HCl solutions were pipetted onto ITO films and allowed to dry fully before measuring changes in sheet resistance, profilometry (see Chapter 4.4.4) was also conducted to measure etch depths. A range of HCl concentrations were investigated to represent various concentrations commonly found in literature [67], [68], [94], [96].

Profilometry results in Chapter 4.4.4 show no measurable etching for ITO films with ~1 mM HCl and below. To our knowledge, the lowest HCl concentration reported for Sn-sensitization is 10 mM HCl, this is low-enough concentration to avoid etching through the entire ITO layer [68]. Next, these two Sn-sensitization solutions (1 and 10 mM HCl) were prepared [68]. Figure 43 schematically shows the surface treatments for the ITO and glass samples used for XPS studies. One glass sample (D_{glass}) was prepared using the high-concentration Sn-sensitization solution following the procedure reported by de Minjer *et al*. [68], an identical process was used on an ITO

sample (D_{ITO}) as well to use a known process reported in literature that results in successful Sn-sensitization and Ag-activation on glass surfaces [68].

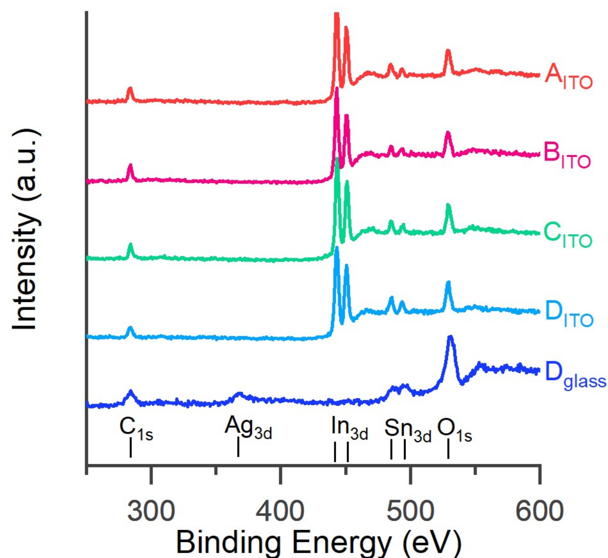

Figure 44. XPS spectra of glass and ITO samples treated with various steps of the Sn-sensitization and Ag-activation process. Binding energies of elements of interest are labeled under the spectra. D_{ITO} and D_{glass} were treated with identical processes, following de Minjer *et al.*, showing that the same process used on glass does not work identically on ITO [71]. Figure taken from our publication, which is reported in full detail elsewhere [90].

Next, these samples were measured by XPS to determine whether the Sn-sensitization and Ag-activation occurred on the ITO and glass surfaces. Figure 44 shows the XPS spectra of these samples treated with various Sn-sensitization and Ag-activation steps (see Figure 43**Error! Reference source not found.**). Sample A_{ITO}, and B_{ITO} were not subjected to Sn-sensitization and act as controls for “clean” and “Ag-activation-only” ITO surfaces, respectively. D_{ITO} was treated with a Sn-sensitization solution and Ag-activation solution replicated from de Minjer *et al.* [68]. To avoid etching the ITO, C_{ITO} was treated with a lower concentration of Sn-sensitization solution (0.1 mM HCl and 0.05 mM $SnCl_2$), followed by Ag-activation following de Minjer *et al.*[68].

Figure 44 shows that all ITO film surfaces have C, In, Sn, and O present, but no Ag was detected on D_{ITO} as expected. The glass sample (D_{glass}) shows the presence of both Sn and Ag. This confirms both the successful Sn-sensitization and Ag-activation of the glass surface. The absence of Ag on all ITO samples suggests that Ag-activation does not occur for ITO samples. This result demonstrates that the process of sensitization and activation occurs differently on ITO than on glass. To understand which part of the sensitization and activation process differs, high resolution XPS measurements were conducted on the ITO samples to evaluate the presence of the O1s and Sn $3d_{5/2}$ peaks to evaluate the process across the 3 steps depicted in Figure 43. The full analysis is reported in our publication detailed elsewhere [89].

The main findings from the high resolution XPS measurements show that both ITO samples treated with Sn-sensitization solutions show an increase in Sn concentration at the surface, and furthermore, an increase in the Sn^{2+} component. These results suggest that D_{ITO} has a sensitized surface, confirming the 2nd step of the process is successful. Regardless of sensitization, there is no apparent Ag-activation on ITO within the detection limits of our experiment. Whereas, successful Sn-sensitization and Ag-activation are evident on glass (D_{glass}).

At this time, only two studies report Sn-sensitization on ITO [69], [75]. These studies by Kim *et al*. report successful Sn-sensitization and Pd-activation for ITO [69], [75]. These results reported by Kim *et al*., and the results in our study point to differences in the activation process [69], [75], [89]. In our study, Sn-sensitization appears to be successful on D_{ITO} due to the increased Sn composition, and specifically increased Sn^{2+} composition near the surface compared to the rest of the ITO samples.

Pd-Activation vs Ag-Activation

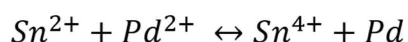

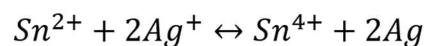

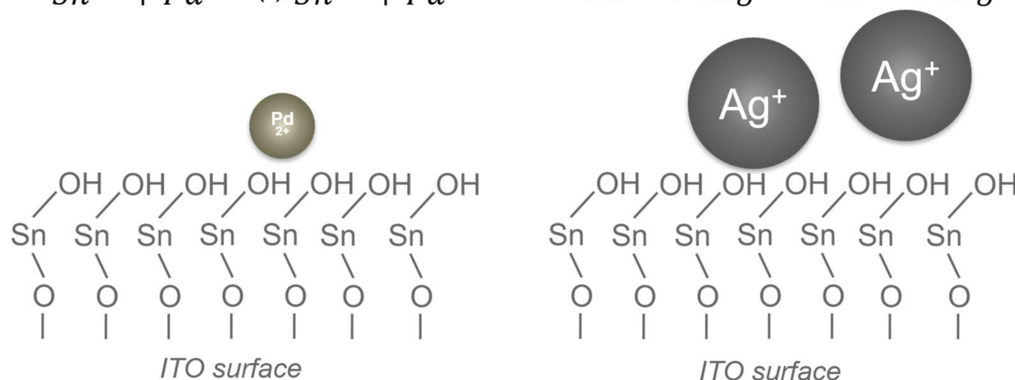

Figure 45. Schematic showing Pd-activation vs Ag-activation on ITO surfaces.

Based on the discussion above, we suggest Ag-activation on ITO surfaces is the limiting step in the process. Figure 45 schematically shows the difference in the Pd-activation and Ag-activation processes on an ITO surface. Table X lists the hydroxide site densitites for ITO and glass surfaces, and the cross-sectional area of one Pd^{2+} ion, and two Ag^{+} ions.Pd activation requires one Pd^{2+} ion to activate the sensitized sites, whereas Ag-activation requires two Ag^{+} ions. Furthermore, the size of the Ag^{+} ions relative to the hydroxide site density on ITO likely results in hinderance of the Ag-activation process on ITO surfaces compared to glass surface, and compared to Pd-activation on ITO surfaces [89]. This ionic hinderance effect could account for the differences observed by Kim *et al*. and our study [69], [75], [89].

Table 4. Pd and Ag ionic cross-sectional areas and hydroxide site density for ITO and glass surfaces.

1× Pd^{2+} area (Å^2)	**2× Ag^{+} area (Å^2)**	**OH site density (Å^2/#)**
1.2 – 2.2	6.2 – 21.2	10.0 *(ITO surface* [98]*)* 17.6 *(glass surface* [68]*)*

From this study, we can conclude that Sn-sensitization solutions modify ITO surfaces, resulting in an increase in surface Sn^{2+} composition. Thus, Sn-sensitization of ITO surfaces is possible with low HCl molar concentrations compatible with ITO thin films. However, Ag-activation on ITO surfaces is not evident. We suggest this is due to a high density of surface hydroxide sites on ITO compared to glass, and smaller area to accommodate two Ag+ ions, which can be amended by using smaller metal ions such as Pd^{2+} for the activation step [89].

5. DEVICE PERFORMANCE & DEGRADATION STUDIES

The previous work presented in 3.1.1 compares an un-optimized DoD-printed RSI to a commercially available screen-printed Ag paste (SP Ag Paste, Namics H9455 series). That work showed that with little optimization, RSI and SP Ag Paste perform comparably as front-grid metallizations for 2×2 cm^2 SHJ cells. Although these first results are promising, more work is necessary to determine whether reactive ink metallizations perform well enough to be a replacement for industrial screen-printing of Ag pastes.

The work presented in this chapter builds on that previous work in several ways. First, a more industrially-scalable dispense printer was used in place of the DoD printer; this new dispense printer ejects a continuous stream of ink, whereas the DoD printer ejected single drop at a time. This continuous-stream dispense printer increases printing speeds from 2-10 mm/s (typical of the DoD printer used in Chapter 3.1.1) up to 20-200 mm/s. Second, using this new dispense printer, we explore the relationship between w_f, finger sheet R, and ρ_m for two reactive silver inks and compare these properties to that of SP Ag Paste. These properties necessitate grid design modifications for each metallization type. Third, mini- and full-sized-SHJ cells are prepared and performance and degradation of cells with RSI and SP Ag Paste front grids are compared. Finally, we report on an experiment designed to study corrosion in diluted acetic acid between RSI and other Ag-based metallizations, a common degradation mechanism of metallization in solar cells.

5.1 Performance of Silicon Heterojunction Solar Cells with RSI and SP Ag Paste

Building on the work presented in Chapter 3.1.1, a series of mini-SHJ cells were fabricated to evaluate performance and relation to metallization type and, to examine losses due to shading, and series resistance.

Table 5. Front-Grid Metallization Properties.

Metallization Properties	RSI f1	RSI f2	SP Ag Paste
w_f (µm)	235	270	150
finger sheet R (Ω/sq)	24.5	27.3	10.5
ρ_c (mΩ cm^2)	5	15	10
finger cross-sectional area (mm^2)	1.0×10^{-3}	1.9×10^{-3}	8.6×10^{-3}
finger Ag usage (mg/cm)	0.1	0.2	0.8

Three sets of four mini- SHJ cells were prepared identically except for front metallization methods. These twelve mini-SHJ cells were prepared from 2×2 cm^2 islands on a full 156 mm wafer. SHJ fabrication was completed following a procedure reported in detail elsewhere [54]. Next, all cells were annealed for 20 min at 200 °C in air to recover damage done to the ITO and passivation layers during sputtering, which recovers carrier lifetime [59], [99], [100].

One set of four mini-cells was prepared with front grids formed from a low-cure-temperature screen-printed Ag paste, Namics XH9455 series (SP Ag Paste). SP Ag Paste cells were then annealed for 40 minutes at 200 °C in air to cure the paste per the manufacturer's specifications. Another set of four mini-cells was prepared with front grids formed from dispense-printed RSI with the base RSI ink formula developed by Walker and Lewis (RSI f1) [43]. A third set of four mini-cells was prepared with dispense-printed front grids formed from a newly-developed RSI by Gaitan (RSI f2). This RSI f2 base ink is made

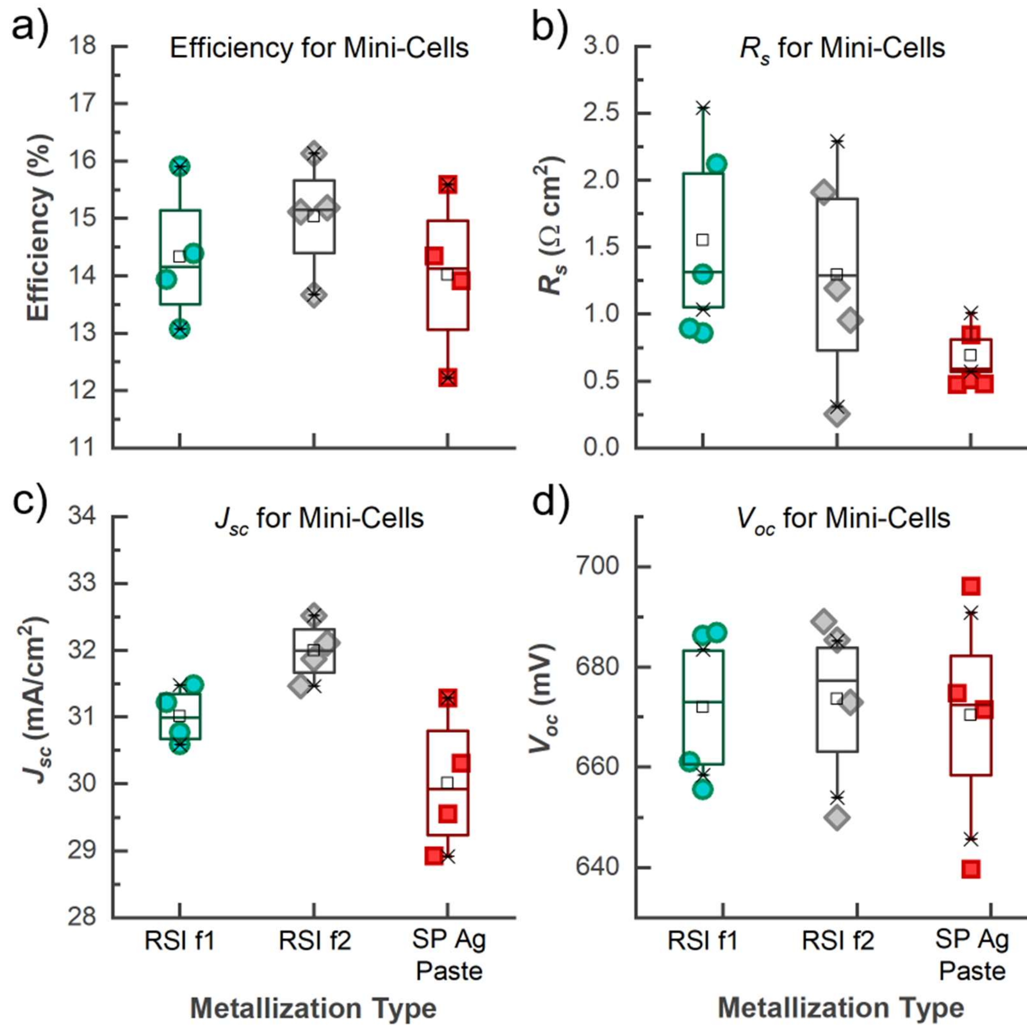

Figure 46. Efficiency (a), R_s (b), J_{sc} (c), and V_{oc} (d) are shown for 4 cm^2 SHJ cells with front grids formed from RSI formula 1 (teal circles), RSI formula 2 (grey diamonds), and SP Ag Paste (red squares). Boxplots are overlaid on the four data points for each type of metallization to show the mean (black square) and median (horizontal line).

from ethylene glycol, silver acetate, and ammonium hydroxide. Both sets of RSI front grids (RSI f1 and RSI f2) were printed at a substrate temperature set point ~100 ˚C.

Front grid patterns were coarsely optimized using Griddler 2.5 software [101]. w_f, ρ_c, and finger sheet R were input for each metallization type. All other parameters were kept constant, and the number of fingers was varied to determine a grid pattern with minimum power loss. Based on the grid optimizations, the RSI f1 front grids had 7 fingers and 1 busbar; the RSI f2 front grids had 5 fingers and 1 busbar; the SP Ag Paste front grids had

10 fingers and 1 busbar. However, it should be noted that this optimization is approximate; this work aims to evaluate performance rather than a complete optimization of a vast parameter space.

Following cell fabrication, one-sun and Suns-V_{oc} IV characteristics were measured on a Sinton FCT 450 tester. A square opaque mask was used to expose only the 4 cm^2 active cell area during IV characterization. External quantum efficiency (EQE) was measured from to 300-1250 nm (PV Measurements, Model QEX10).

Figure 47 shows efficiency (a), R_s (b), J_{sc} (c), and V_{oc} (d) for each set of mini-cells. All three sets (RSI f1, RSI f2, and SP Ag Paste) of SHJ cells have efficiencies ranging from 12.2-16.1 %, the highest efficiency cell is an RSI f2 metallized cell. This highest-efficiency cell also had the lowest R_s value (0.3 $\Omega \cdot cm^2$) of all the cells. RSI f1 had the highest average R_s of 1.5 $\Omega \cdot cm^2$, followed by RSI f2 with R_s of 1.25 $\Omega \cdot cm^2$, and the lowest R_s for SP Ag Paste with R_s of 0.7 $\Omega \cdot cm^2$ (Figure 47 (b)).

On the other hand, average J_{sc} for RSI f1 and RSI f2 cells was 1 mA and 2 mA higher than for the SP Ag Paste cells, respectively (Figure 47 (c)). EQE measurements showed that all three sets of cells had similar active-area J_{sc} with an average of 37.7 ± 1.1 mA/cm^2 for all 12 cells. This suggests that the difference in J_{sc} (measured by IV) for each metallization type is due to extent of shading by the front grid. RSI f2 cells had the highest average J_{sc}, and the least number of fingers (5 fingers) from the grid optimization. SP Ag Paste had the lowest average J_{sc}, and the highest number of fingers (10 fingers). Figure 47 (d) shows V_{oc} for all cells was low (~670 mV) and relatively constant for all three sets of cells, suggesting that the poor efficiency is due to poor lifetime of the solar cell and not related to the metallization type.

From these results, it is clear that for all three metallization types, i) performance of the cells is comparable, and ii) losses from R_s and J_{sc} can still be improved by further optimizing the grid designs and minimizing process variability. One RSI f2 cell has the highest efficiency (16.1%), lowest R_s (0.3 $\Omega \cdot cm^2$), and highest J_{sc} (32.5 mA/cm^2) values, suggesting that the front grid design is closer to optimal compared to the rest of the RSI f1, and SP Ag Paste front grid designs.

Although these results suggest that the mini-cells perform comparably regardless of the metallization type, there is a dramatic difference in the amount of Ag used per solar cell. The RSI f1, and RSI f2 finger cross-sectional areas were less than 25% of the SP Ag Paste cross-sectional area (Table 5). Assuming the SP Ag Paste is 90 % (vol.) Ag, and RSI f1 and RSI f2 are 100 % (vol.) Ag, the RSI cells use 1/4 to 1/8th the amount (by mass) of Ag per cm of metallization. Note that the actual porosity of RSI f1 and RSI f2 for these printing parameters has not yet been evaluated, but it is likely porous like the RSI metallizations described in Chapters 3 and 4.

Table 5 also shows finger sheet R for RSI f1, RSI f2 and SP Ag Paste. To reduce the finger sheet R for the RSI f1 and RSI f2 fingers below that of the SP Ag Paste fingers, the finger cross-sectional areas should be increased by a factor of ~2.3, and ~2.6 respectively. Finger sheet R can be reduced by optimizing the number of layers printed; However, additionally, solvent: ink ratio needs to be optimized for printing a higher number of layers without compromising adhesion performance (see Chapter 4.1). Still, with these conservative estimates, this would result in a significant decrease in Ag usage (savings of 0.3- 0.6 mg Ag/cm) compared to SP Ag Paste.

5.1.1 Printing Process Variation & Optimization Opportunities

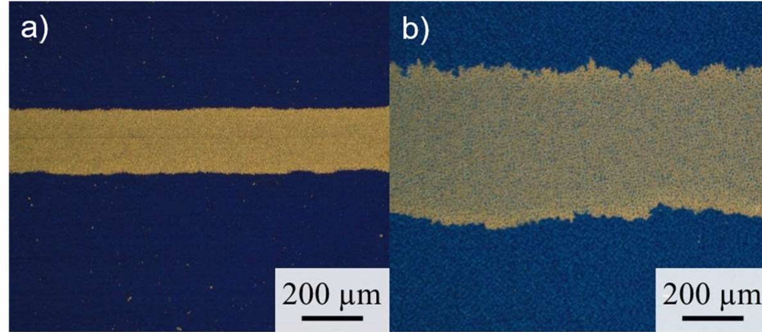

Figure 47. Optical microscope images of two RSI f1 fingers printed on ITO-coated textured Si. Fingers were printed with similar printing parameters. However, the resulting line widths are significantly different, showing the variation in contact angle of the reactive ink on ITO surfaces. a) High contact angle finger with w_f of 210 µm. b) Low contact angle finger with w_f of 503 µm.

Above, we note that the finger geometries for the mini-cell front grids are not quite representative of what could be done with a further optimized and repeatable process. First, the SP Ag Paste fingers spread more than on the preliminary test samples that were used for grid optimization. This is due to a change in paste to a product that was slightly less viscous, resulting in quite wide w_f (150 µm) compared to those used to optimize the grid (100 µm). In an industrial setting, screen-printed Ag paste fingers of <100 µm are routinely produced by process-controlled manufacturing lines [8], [25].

Second, the relatively new dispense printer was not yet operating without occasional defects. An example of common unresolved defects occurs when the nozzle tip is too close to the surface of the sample, scrapes off some of the previously printed layers resulting in higher resistance than expected. This is currently under investigation by collaborators and is expected to be fixed for future work.

Third, we found that dispense printing reactive inks is quite sensitive to the surface properties of the substrate. Specifically, we observed that the w_f was dramatically different from sample to sample, and over time on the same sample.

Table 5. Summarized experiments and findings used to determine the cause for variation in contact angle, θ, for various ITO-coated samples.

Factor Tested	**Approach**	**Findings**
Si Wafer Texture	Compared θ for textured vs. untextured Si	θ varied independently of texturing. Textured silicon shows lower θ.
a-Si layer under ITO	Compared θ with and without a-Si layer	θ varied independently of of a-Si layer
Lifetime of Si wafer	Compared θ in regions/samples with low and high lifetimes.	θ varied independently of lifetime.
ITO sheet resistance	Measured R_{sh} across multiple samples and ITO thicknesses.	θ varied independently of lifetime R_{sh}.
Wafer size and placement in ITO	Cleave mini-wafers and place in different locations	θ was higher at the edges but still low in the center. θ is independent of location in the ITO.
Annealing temperatures	Varied annealing temperature from 120 ˚C to 200 ˚C.	θ was higher at the edges but still low in the center.
Wafer loading during ITO Deposition	Wafer is held under tension (flat) or compression (bowed) during ITO	θ was higher at the edges but still low in the center.
Annealing duration	Varied annealing from 0 min to 40 minutes.	Some wafers showed uniform, high θ before annealing. After annealing θ variation was observed.
ITO surface composition	Compared θ for different ITO surface compositions using XPS	Wafers with low θ had low C at.% composition, wafers with high θ had high C at. % composition.

Figure 48 shows an example of different w_f achieved using the same printing parameters on an ITO-coated textured Si wafer. This suggested that surface energy of our samples was variable, and this variability significantly influenced ink wettability, or contact angle (θ), and therefore w_f. Table 6 summarizes a series of experiments that were conducted to determine the cause for variation in θ from sample to sample.

Finally, a study using X-ray Photoelectron Spectroscopy (XPS) was conducted to determine the compositional difference in surfaces with high θ vs. low θ. ITO-coated

textured Si wafers were prepared, stacked, and stored in ambient conditions for 4 days. Immediately before XPS measurements, D.I. water (5 μL) was pipetted on a portion of the sample to determine if it had relatively low or high contact angle. Three samples were cut out from wafers with relatively high θ, and one sample was cut out from a wafer with relatively low θ. We found that ITO-coated Si wafers with relatively lower θ had relatively low amounts of carbon on the surface compared to those with high θ (see Table 7). The wafer with relatively low θ was stored in a stack of other wafers immediately following deposition, limiting the surface contamination compared to the other three wafers. These results are in line with observation by others, and suggests that atmospheric hydrocarbon adsorption, is the cause of the increased contact angle [83], [102].

Table 6. XPS results for ITO-coated textured Si wafers with varying relative contact angles.

Sample	Relative Contact Angle	Carbon at. %
A	High	25.2
B	High	20.8
C	High	22.9
D	Low	12.1

These results show the sensitivity of the dispense printing process for reactive inks. We suggest that with further optimization of printing parameters, substrate surface treatments, and implementation of statistical process controls for the dispense printing process, dispense printed reactive inks can outperform SP Ag Paste with a fraction of the Ag usage.

5.2 Reliability & Performance of RSI and SP Ag Paste Cells Through Damp Heat

The previous chapter showed performance of mini-SHJ cells with front grids formed from three different Ag-based metallizations; RSI f1, RSI f2, and SP Ag Paste. The next step is to address whether reactive ink metallized solar cells are durable enough to withstand performance degradation throughout industry standard reliability testing. Understanding the long-term reliability and durability along with modes of failure are necessary to determine whether this novel metallization method is competitive with conventional metallization methods.

Three sets of four mini- SHJ cells were prepared identically except for front metallization methods (the same cells from Chapter 5.1). Each set of four mini-cells had front grids formed from RSI f1, RSI f2, and SP Ag Paste. Additionally, four full-sized (156×156 mm^2) SHJ cells were prepared following the same procedure. One full-sized cell was prepared with a front grid formed from RSI f1, three other full-sized cells were prepared with front grids formed from SP Ag Paste(see Chapter 5.1).

All cells were annealed for 20 min at 200 °C in air to recover damage done to the ITO and passivation layers during sputtering, and to recover effective carrier lifetime [59], [99], [100]. After printing, SP Ag Paste cells were annealed for 40 minutes at 200 °C in air to cure the paste as per the manufacturer's specifications. Both sets of RSI front grids (RSI f1

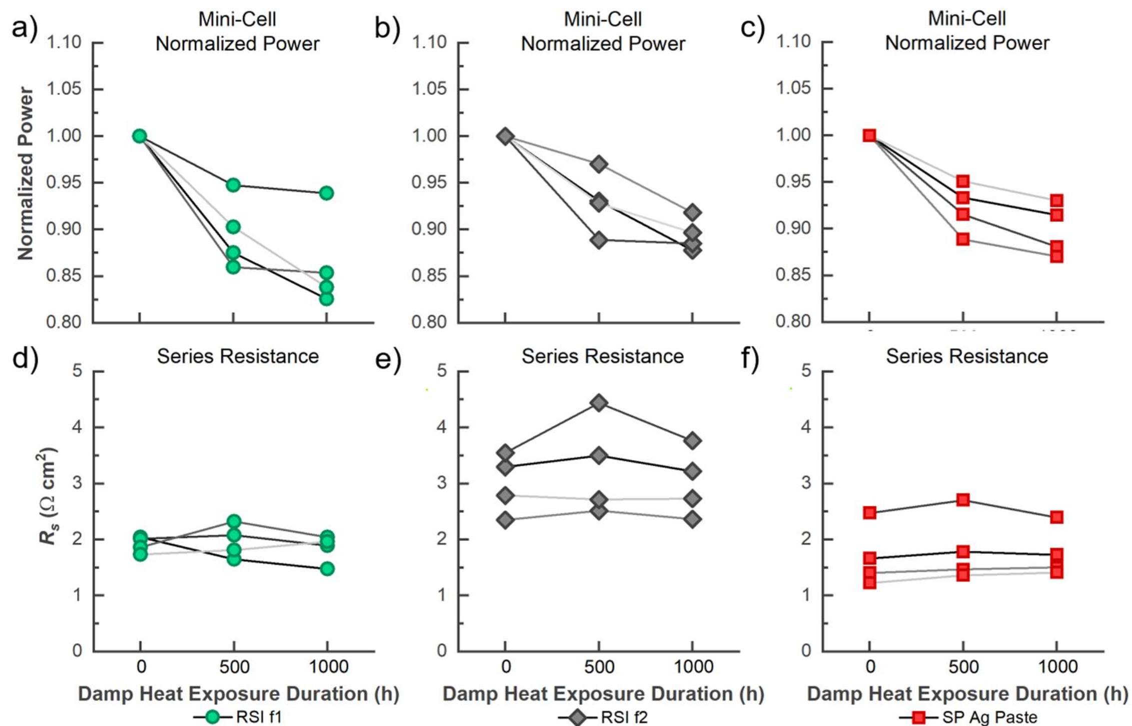

Figure 48. Normalized power and series resistance throughout 1000 h of damp heat exposure (IEC 61215) for mini cells (4 cm^2) with front grids formed from RSI formula 1 (a,d), RSI formula 2 (b,e), and a low-cure temperature SP Ag Paste (c-f).

and RSI f2) were printed at a substrate temperature set point ~100 ˚C. Based on a coarse grid optimization (described in Chapter 5.1), the large-area 156×156 mm^2 RSI f1 cell had 50 fingers and 5 busbars, and the SP Ag Paste cells had 70 fingers and 3 busbars.

Here, for reliability and performance evaluation, the cells are encapsulated to form single-cell modules. We have seen from previous experiments that soldering busbar ribbons to printed RSI busbars results in severe damage to the RSI cells. So, for the RSI f1 and RSI f2 cells, busbar ribbons were adhered to the printed busbars using a high-purity silver paint (SPI Supplies). For the SP Ag Paste cells, busbar ribbons were soldered to the screen-printed busbars. Next, these cells were laminated with ethylene vinyl acetate (EVA) encapsulant, back sheet, and front glass typical of PV industry methods.

Modules were then characterized by one-sun and Suns-V_{oc} IV measurements (Sinton FCT 450), qualitative electroluminescence (EL) and photoluminescence (PL) imaging, and external quantum efficiency (EQE, PV Measurements Model QEX10). Images from EL images were taken with a 600 mV applied bias. EL and PL images were adjusted for clarity in figures; brightness was increased so that features and artefacts on each cell were visible before and after the DH 1000 exposure. This adjustment still allows for determination of variability of bright and dark regions within each cell, and for observation of cracks, and finger delaminations and breakage.

Following initial characterization, the full-sized modules were then placed in an environmental chamber for damp heat testing (DH 1000, IEC 61215, see Chapter 1.2.4 for more details). The purpose of the DH 1000 test is to determine the ability of the module to withstand long-term exposure to penetration of humidity by applying 85 ˚C ± 2 ˚C with a relative humidity of 85% ± 5% for 1000 hours [103]. The DH test particularly challenges the lamination process and the edge sealing from humidity. DH exposure can cause module delaminations and corrosion of cell parts as a result of humidity penetration. Corrosion of materials within the module can lead to power losses from degradation of the metallization, solder bonds, the antireflective coating, and the base [104], [105]. To pass the DH 1000 test (IEC 61215 standard qualification test), the maximum power (P_{mp}) must not degrade more than 5% of the initial P_{mp} at the end of the test [103]. In this work, we focus on degradation incurred for different Ag-based metallizations, specifically R_s increases throughout time. Furthermore, a detailed study of corrosion of Ag-based metallizations is presented in Chapter 5.3.

IV characterization was carried out after encapsulation (0 h), half-way through the DH 1000 exposure (500 h), and at the completion of DH 1000 (1000 h). Figure 48 (a-c) shows normalized power (P_{mp} normalized to P_{mp} at 0 h for each mini-cell module) throughout the DH 1000 exposure. All twelve mini-cell modules degraded at least 2 % of initial P_{mp} after 500 h, and more than 5% of initial P_{mp} after 1000 h, which is considered failure of the DH 1000 test. On average, the mini-cell modules degraded to about 89 ± 3 % of initial P_{mp}, and degradation is not distinct based on metallization type. P_{mp} degradation may occur for various reasons, many not related to metallization. Common examples of non-metallization related degradation are yellowing of encapsulation, antireflective coating deterioration, hydrolysis of the EVA encapsulant, shunts, and a loss in surface passivation [105], [106].

Metallization related degradation, such as corrosion or finger delaminations, manifests in increased series resistance (R_s) [105], [106]. Figure 48 (d-f) shows R_s of the mini-cell modules throughout the 1000 h of DH exposure. Here, R_s is not normalized to each modules' initial value in order to show the absolute difference in R_s among the different metallization types. RSI f1 modules have the narrowest distribution of R_s values of the three metallization types. Note that compared to initial R_s values reported in Chapter 5.1, R_s increased by ~0.5, ~1.6, and ~1.2 $\Omega \cdot cm^2$ for RSI f1, RSI f2, and SP Ag Paste modules (at 0 h), respectively. This shows that compared to RSI f2, and SP Ag Paste cells, the RSI f1 grid properties after encapsulation resulted in most repeatable, and lowest R_s losses from the encapsulation process. SP Ag Paste modules have comparable R_s values to RSI f1 modules, but a wider distribution; we suggest this is from variations in the soldering contact between the

busbar ribbons and the SP Ag Paste grid. On the other hand, RSI f2 modules has the highest average R_s, and largest variation in R_s from cell to cell. Since RSI f1 and RSI f2 were both printed by the same dispense printer, we suggest that the variation in R_s is not due to dispense printing defects. Rather, RSI f2 is a relatively new ink that was developed only several weeks prior to printing these cells and had only a short time for optimization of printing parameters, ink formulation, understanding of ink reaction kinetics and mechanical durability. We observed that the RSI f2 metallization was quite fragile compared to RSI f1 and SP Ag Paste metallizations. So, we suggest this larger variation in R_s for RSI f2 modules (at 0 h) is a result of inhomogeneous damage to the front grid from handling and the encapsulation process.

At the end of 1000 h of DH exposure, R_s values for all mini-cell modules are approximately the same as the initial R_s values, again suggesting that degradation to P_{mp} is not due to metallization degradation. Significant losses in J_{sc} and V_{oc} occur throughout the 1000 h of exposure; on average, J_{sc} decreases 4 mA/cm^2, and V_{oc} decreases 20 mV. These losses are not dependent on metallization type, and account for P_{mp} degradation. At this time, very little literature exists on degradation of SHJ modules. Jordan *et al.*, recently published a study on power degradation of SHJ modules deployed in the field for 10 years [107]. They found that V_{oc} degradation is the main contributor to power losses over time, and that increased R_s and recombination, and decreased minority carrier lifetime occur uniformly within the cells (i.e. neither on the cell surface nor local to the metallization) [107].

These results showed that both RSI f1 and RSI f2 metallized mini-cell modules degradation was not due to degradation of the RSI metallizations. However, mini-cell

modules are not representative of cells that are employed in the field. Thus, the next step is to scale-up to full-sized cell (156 × 156 mm^2) modules and monitor degradation related to metallization.

49 (a) shows P_{mp} normalized to initial P_{mp} for four full-sized modules; one with RSI f1 front grid metallization (green circles), and three with SP Ag Paste front grid metallization (red squares). For all three SP Ag Paste full-sized modules, P_{mp} degrades

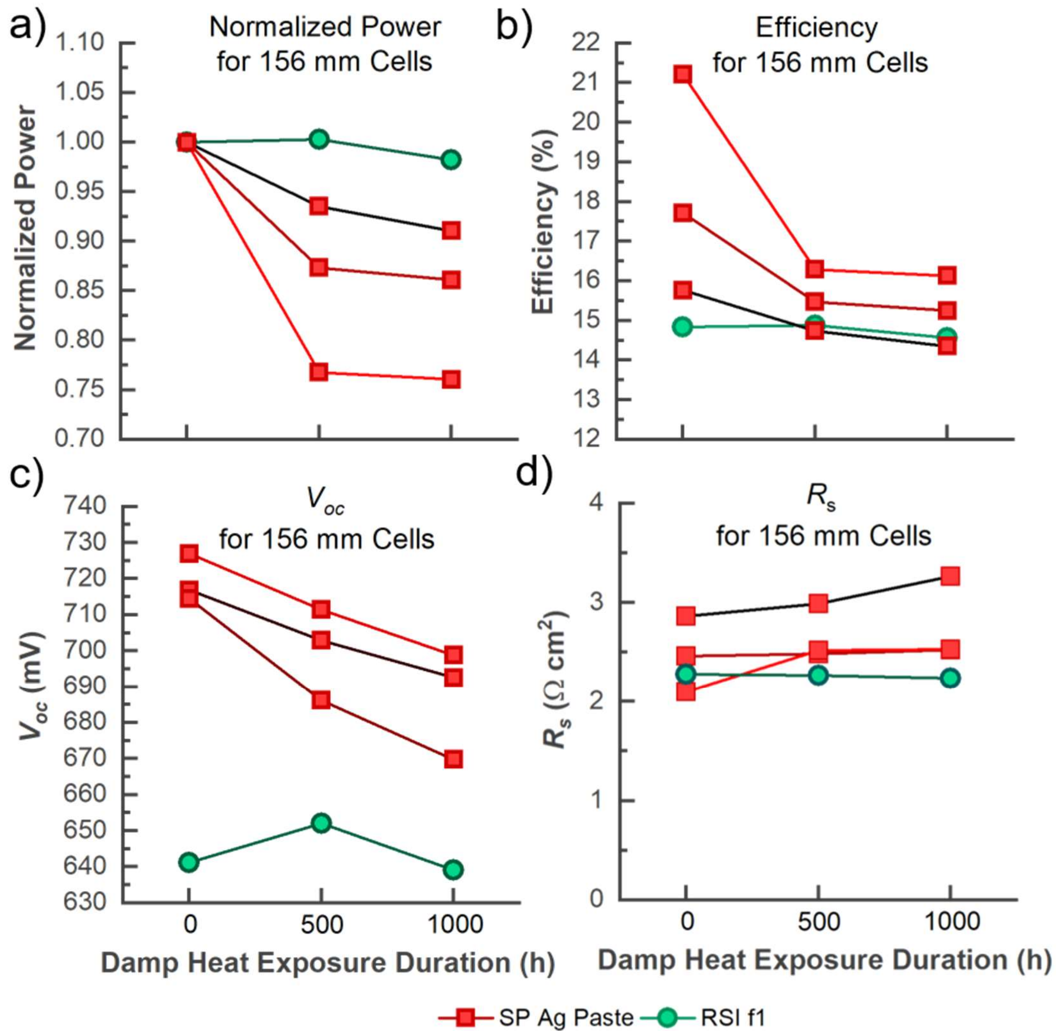

Figure 49. Normalized power (a), efficiency (b), V_{oc} (c), and R_s (d) throughout 1000 h of damp heat exposure (IEC 61215) for full-sized cells (239 cm^2) with front grids formed from RSI formula 1 (green circles), and a low-cure temperature SP Ag Paste (red squares). Line color connecting data points for each individual sample are kept the same for (a-c), and in Figures 50-51.

significantly more than 5 % of initial P_{mp} after only 500 h of exposure. On the other hand, the RSI f1 full-sized module degrades only 1.8% of initial P_{mp} after the 1000 h exposure. Again, to pass the DH 1000 test according to IEC 61215 standard qualification, P_{mp} must not degrade more than 5% of the initial P_{mp} after the completion of the 1000 h exposure [103]. Here, we have shown that the full-sized module with RSI f1 front grid metallization passes the IEC 61215 DH 1000 test.

Figure 49 (b) shows efficiency of the full-sized modules throughout the exposure to compare differences based on metallization type. Although, the RSI f1 module P_{mp} degraded minimally, it started with the lowest efficiency showing there are still significant areas for improvement in initial performance of full-sized cells. We suggest that the lower efficiency exhibited by the RSI f1 module can be improved with further improvements in the printing parameters and process, and grid optimization. For example, J_{sc} for the RSI f1 cell is ~20 mA/cm^2 lower than for SP Ag Paste cells, this is primarily due to large w_f of ~250 µm for the RSI f1 fingers compared to ~100 µm for the SP Ag Paste fingers. Still, although the RSI f1 cell starts with an efficiency of only 14.8 %. At the end of the 1000 h exposure, the RSI f1 cell has an efficiency of 14.6 % which is comparable to the efficiency of the SP Ag Paste cell that has degraded the most. V_{oc}, and J_{sc} for these full-sized modules also significantly degraded.

Figure 49 (c) shows V_{oc} for the full-sized modules. Initially (at 0 h), the RSI f1 module, V_{oc} is 640 mV, which is ~80 mV lower than the average V_{oc} for the SP Ag Paste modules. V_{oc} values for SHJ cells are typically above 700 mV, this is in part due to the excellent passivation provided by the hydrogenated a-Si layers [30], [108]. Such low V_{oc} exhibited

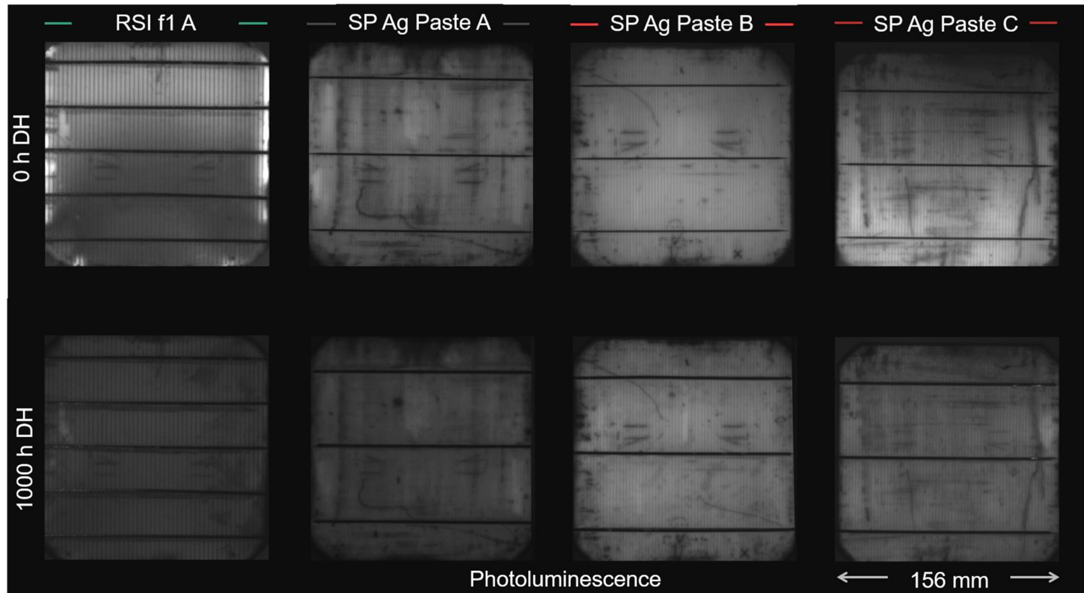

Figure 50. Photoluminescence of full-sized cells before and after 1000 h of Damp Heat (IEC 61215). The colored lines next to the sample names indicate the colored lines for each sample shown in Figure 49.

by the RSI f1 module suggests poor passivation and minority carrier lifetimes. This can be from two factors; First, the RSI f1 cell was stored and handled differently than the SP Ag Paste cells; Cells for RSI printing were removed from the cleanroom-controlled environment for approximately one month for printing in our collaborator's lab, while the SP Ag Paste cells were stored in the cleanroom for this duration. Second, the RSI f1 cell and SP Ag Paste cells undergo different thermal treatments; Prior to front-gird metallization, all cells are annealed at 200 °C for 20 min in air to recover damage done to the ITO layer during sputtering and recover passivation by the hydrogenated a-Si layers. Following screen-printing, the SP Ag Paste cells are annealed for 40 min at 200 °C to cure the paste. Whereas, during dispense printing, the RSI cells are heated only to ~100 °C for less than 30 minutes. Generally, SHJ cells improve minority carrier lifetime and implied V_{oc} by a post-processing anneal at ~200 °C in air for at least 10 minutes [59], [99], [100], [109]. However, some studies report on continued

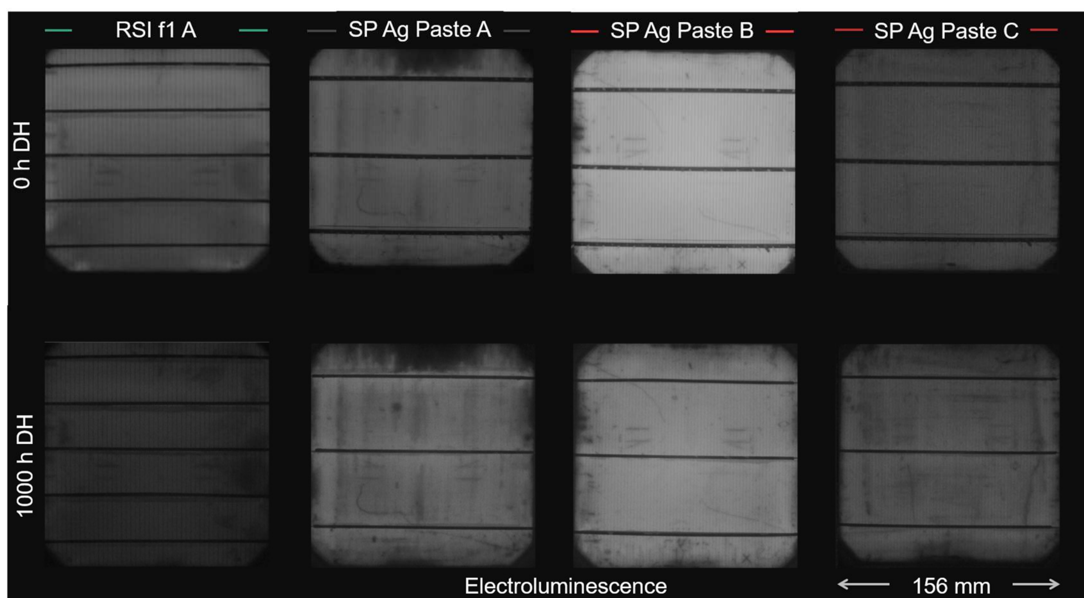

Figure 51. Electroluminescence of full-sized cells before and after 1000 h of damp heat exposure (IEC 61215). The colored lines next to the sample names indicate the colored lines for each sample shown in Figures 49 and 50.

improvement to minority carrier lifetime and implied V_{oc} as the annealing duration is extended ≥ 60 min at ~200 °C in air [99], [100]. We suggest this is a potential cause for the significant difference in V_{oc} for the RSI f1 and SP Ag Paste cells initially. That is, the metallization itself did not influence the V_{oc}, rather the different thermal processes for each metallization influences the V_{oc} and should be optimized for future performance and reliability studies.

Figures 50 and 51 show photoluminescence (PL) and electroluminescence (EL) images, respectively, of the full-sized modules at 0 h and after 1000 h of damp heat exposure. EL imaging was done by applying the same voltage for each sample at each exposure duration, and imaging light emitted from the cells. Both EL and PL show darkening around the edge of the cells suggesting a decrease in lifetime. These results are in line with observations reported by Jordan *et al*. about degradation of field-exposed SHJ modules [107]. This appears in all four full-sized modules, indicating that this darkening

is not distinct for either metallization type. The EL images otherwise show no new artefacts after 1000 h of exposure, which indicates that no finger delaminations or breaks have occurred. However, it is clear from Figure 49 (c) that the R_s increases more for full-sized modules with SP Ag Paste than for RSI f1.

To focus on the clear metallization-related degradation, 490 (d) shows R_s of the full-sized modules throughout the 1000 h exposure. The RSI f1 cell has the second lowest R_s initially, and R_s remains relatively constant. Whereas, for the SP Ag Paste cells throughout the entire 1000 h exposure, one cell's R_s value remains relatively constant, another cell's R_s increases by ~0.4 $\Omega\cdot cm^2$, and the final cell's R_s increases by 0.5 $\Omega\cdot cm^2$. These first results are limited, yet promising, as they suggest that RSI f1 cells do not degrade more than their SP Ag Paste counterparts.

These are the first results that report on i) performance of a full-sized SHJ cell with reactive ink front gird metallization, and ii) DH 1000 performance for SHJ cell modules with reactive ink front gird metallization. For the mini-modules, all RSI f1, RSI f2, and SP Ag Paste cells degraded significantly due to V_{oc} and J_{sc} losses not related to degradation of the metallization. We also showed that for the RSI f1 full-sized module, performance (P_{mp} at 0 h) through DH 1000 not degrade below 95 % of its initial performance (P_{mp} at 1000 h). However, the initial performance of the full-sized module needs to be improved through further optimization of printing parameters, substrate surface treatments, and implementation of statistical process controls for the dispense printing process, dispense printed reactive inks can outperform SP Ag Paste with a fraction of the Ag usage. Furthermore, there is some indication that the full-sized SP Ag Paste cells had a higher R_s increase during the DH 1000 test. It is unclear from the

results presented in this chapter whether the RSI metallization is more resistant to corrosion than the SP Ag Paste. The next chapter details a study where we expose two different SP Ag Pastes, and RSI f1 to an isolated corrosive environment mimicking that of a field- and DH-exposed module to study the difference in corrosion of these Ag-based metallizations.

5.3 Corrosion of Silver-Based Metallizations in Diluted Acetic Acid

Corrosion can cause significant power losses in field- and damp heat-exposed modules throughout their operational lifetime [104], [110], [111]. Again, economic viability of PV technology is dictated by levelized cost of energy (LCOE) for solar PV compared to competing generation sources [6]. The previous chapters showed that R_s did not significantly increase for RSI cells throughout DH 1000. Here, we implement an experiment to study corrosion of metallizations in an aggressive and isolated environment prior to running additional DH1000 tests and waiting for degradation in field-exposed modules.

Corrosion occurs in modules primarily from degradation of encapsulation materials. Specifically, modules are commonly encapsulated with ethylene vinyl acetate (EVA). EVA, when exposed to moisture, elevated temperature, or ultraviolet light, produces acetic acid [111], [112]. Inopportunely, Ag-based metallizations are corroded by acetic acid [113], [114]. Corrosion of Ag-based metallizations used on diffused junction solar cells (HT Ag Paste) has been studied for decades [110], [111], [114]. However, at this time, sparse literature is available on LT Ag Pastes corrosion, such as those used on SHJ cells, and none exists on RSI. The work described here summarized a publication reported in full detail elsewhere [115].

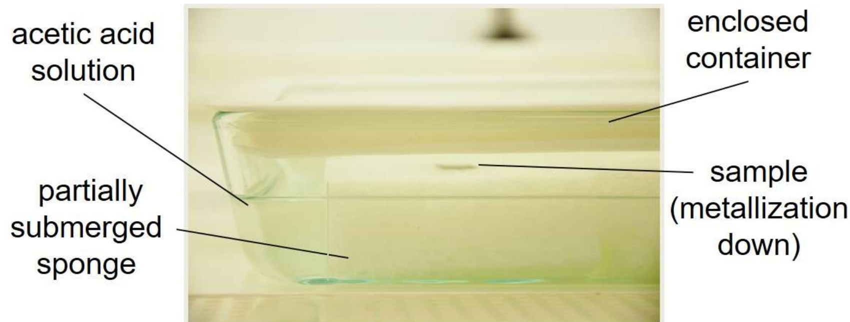

Figure 52. Photograph showing the experimental setup for exposing metallization pads to diluted acetic acid by leaching the solution through a cellulose sponge. This figure is copied from our publication, which is reported elsewhere [116].

The work presented in Chapter 5.2 evaluated performance and R_s degradation throughout 1000 h of damp heat exposure (IEC 61215) for two sets of SHJ cells with different front-grid metallizations; one set prepared dispense-printed RSI, and the other set prepared with screen-printed LT Ag Paste. We found that R_s for the RSI cell did not notably change throughout the 1000 h exposure, whereas the LT Ag Paste cell R_s increased by ~ 0.3 $\Omega \cdot cm^2$ on average. From those limited results, it was not conclusive whether the difference in R_s degradation was due to differences in RSI and LT Ag Paste corrosion in the damp heat-exposed modules.

Here, we investigate the corrosion of three Ag-based metallizations exposed to acetic acid solutions in concentrations representative of those found in field- and damp heat-exposed PV modules. The acetic acid exposure used in this experiment mimics corrosion in degraded modules while also allowing intermittent characterization of the throughout the exposure. This study is summarized briefly below.

Three sets of Ag-based metallization samples were prepared: 1) HT Ag Paste, a high-temperature fire-through Ag-paste sintered above 800 °C which is commonly used for Si diffused junction solar cells; 2) LT Ag Paste, a low-temperature paste cured at 200 °C that

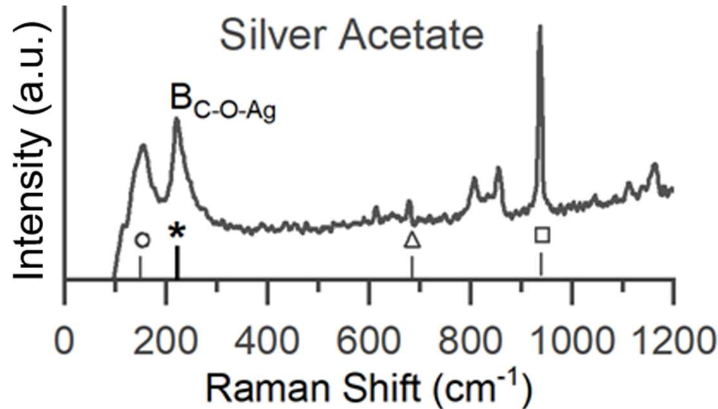

Figure 53. The $B_{C\text{-}O\text{-}Ag}$ mode of silver acetate is indicated by an asterisk. The $V_{Pb\text{-}OH}$ mode of lead acetate is indicated by a filled diamond. The V_{SiO4} mode from the leaded glass frit is indicated by the filled-black circle. The V_{Ag}, $B_{C=O}$, and R_{CH3} modes for silver acetate are indicated by the unfilled circle, triangle, and square, respectively.

is used for SHJ cells (the same paste studied in Chapters 3-5.2); and 3) RSI (RSI f1 from Chapters 3-5.2), which is heated to just 65 °C for solvent evaporation [45], [116].

The experimental exposure setup is shown in Figure 52. This is a simplified setup which aims to simulate the way in which acetic acid leaches out from EVA in modules. Sealed glass containers were partially filled with a solution of 2.4 % acetic acid by volume. This concentration is representative of acetic acid concentrations found in field- and damp heat-exposed modules [117]–[119]. The cellulose sponges deliver an essentially infinite source of the diluted acetic acid and air to the samples. These samples were placed metallization-side down and left for an accumulated exposure duration of 3000 h. Intermittently throughout the exposure, corrosion was monitored by Raman spectroscopy mapping, SEM, and XRD.

Silver acetate is an expected corrosion product of Ag-based metallizations [111], [113]. Figure 53 shows a reference Raman spectrum of 99 % pure silver acetate measured in this study, which agrees with those reported in literature [111], [120]. The Raman mode in Figure 53 between 224-260 cm^{-1} is attributed to bending of the C-O-Ag bond (referred to

as $B_{C\text{-}O\text{-}Ag}$) in silver acetate ($AgCH_3COO$) [120]. Thus, the $B_{C\text{-}O\text{-}Ag}$ mode is a straightforward proxy for the presence of silver acetate and will be used as a metric to determine susceptibility to corrosion by acetic acid in this study [115].

Although each type of metallization studied in this experiment is mainly composed of Ag, each metallization has other compositional components as well. For example, the HT Ag Paste is ~ 98 % solid vol. Ag, and the remaining 2 % is the leaded-glass frit [15]. The initial averaged Raman modes are reported elsewhere [115]. Figure 54 shows boxplots summarizing the relevant Raman modes for each metallization throughout the 3000 h exposure.

Figure 54 (a) shows for the HT Ag Paste, an increase followed by a decrease in the relative intensity of the $B_{C\text{-}O\text{-}Ag}$ and vibrational mode of Pb-OH ($V_{Pb\text{-}OH}$) in silver acetate, and lead acetate, respectively [120] [121], [122]. Unfortunately, the $B_{C\text{-}O\text{-}Ag}$ and $V_{Pb\text{-}OH}$ modes are close in Raman shift, and are not distinguishable from this dataset.

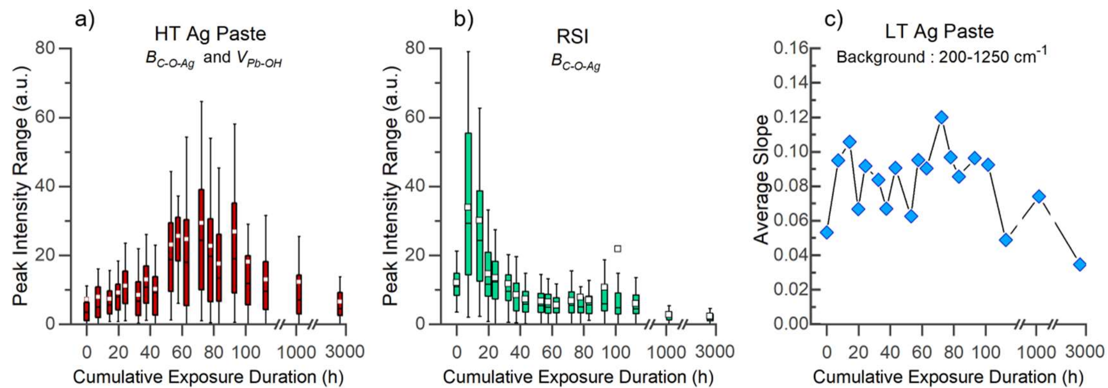

Figure 54. Boxplots showing the distribution of the $B_{C\text{-}O\text{-}Ag}$ and $V_{Pb\text{-}OH}$ for HT Ag Paste (a), and $B_{C\text{-}O\text{-}Ag}$ for RSI (b), and average slope of the background from 200-1250 cm^{-1} for LT Ag Paste throughout 3000 h of exposure to diluted acetic acid. The colored-box region shows the 25th - 75th percentile, and the whiskers extend to ±1 inner quartile range from the colored-box. The mean is shown by the white square, and the median is shown by a horizontal black line. (a) and (b) are copied from our publication reported elsewhere [116].

Nevertheless, this shows an increase followed by a decrease in the relative intensity of

these Raman modes throughout the exposure for HT Ag Paste. Figure 54 (b) shows a similar behavior for RSI; there is an increase followed by a decrease in the relative intensity, but with only $B_{C\text{-}O\text{-}Ag}$ since there is no leaded glass frit in RSI.

On the other hand, Raman modes were not observed for the LT Ag Paste, likely due to a high fluorescence background from the relatively high polymer content [123]. Because of this, Figure 54 (c) shows the average slope of the background for the LT Ag Paste. After 110 h there is a decrease in the background slope and overall intensity. This decrease in background slope and intensity continues to the end of the exposure. Solid polymers exhibit a strong background fluorescence signals, so we suggest that this background comes from the organic polymers in the LT Ag Paste, and that over time, the polymers interact with the acetic acid and are slowly removed from the LT Ag Paste surface[115], [123].

The relevant chemical reactions during the exposure are shown in Equations 5.1-5.5 below:

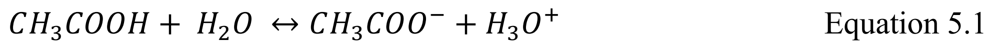

$$CH_3COOH + H_2O \leftrightarrow CH_3COO^- + H_3O^+ \quad \text{Equation 5.1}$$

$$CH_3COO^- + Ag^+ \leftrightarrow AgCH_3COO \quad \text{Equation 5.2}$$

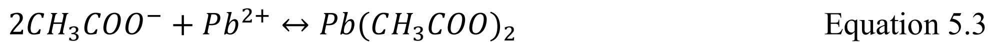

$$2CH_3COO^- + Pb^{2+} \leftrightarrow Pb(CH_3COO)_2 \quad \text{Equation 5.3}$$

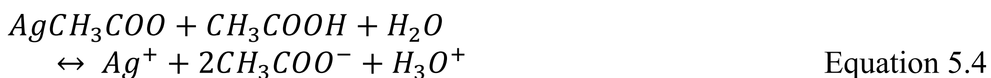

$$AgCH_3COO + CH_3COOH + H_2O \leftrightarrow Ag^+ + 2CH_3COO^- + H_3O^+ \quad \text{Equation 5.4}$$

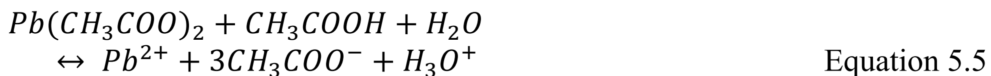

$$Pb(CH_3COO)_2 + CH_3COOH + H_2O \leftrightarrow Pb^{2+} + 3CH_3COO^- + H_3O^+ \quad \text{Equation 5.5}$$

First, acetic acid partially dissociates in water (Equation 5.1). For the HT Ag Paste, the acetate ions react with Ag and Pb ions, forming silver acetate, and lead acetate (Equations 5.2 and 5.3, respectively). Similarly, for the RSI, silver acetate forms (Equation

5.2). However, these corrosion products (lead acetate and silver acetate) are somewhat soluble in water, and their solubilities change depending on pH. Over time, the silver acetate and lead acetate in contact with the solution will dissolve (Equations 5.4-5.5), with lead acetate having higher solubility and dissolving more compared to silver acetate [115]. So, there is a competing reaction between the formation and dissolution of corrosion products until equilibrium is reached between these reactions.

Most importantly, the HT Ag Paste approaches this equilibrium at 3000 h more silver acetate and/or lead acetate than its initial composition at 0 h. Whereas, the RSI approaches equilibrium at 3000 h with less silver acetate than its initial composition. Again, the RSI used in this study has silver acetate initially as it is one of the ingredients in the formulation [45], [54]. We suggest that this behavior (corrosion product formation, followed by dissolution) would happen for both RSI and HT Ag Paste as cyclic corrosion, until equilibrium is met locally. On the other hand, the LT Ag Paste shows no detectable change in surface chemical composition. These results are in line with literature reporting the corrosion-resistant qualities of additives in the LT Ag Paste , suggesting that LT Ag Paste corrosion is minimal compared to HT Ag Paste and RSI [124], [125].

Summarized below are the main findings from this study that have been reported in full detail elsewhere [115]. We found that throughout 3000 h of exposure to dilute acetic acid, there are different corrosion behaviors for each of the three Ag-based metallizations investigated. Specifically, we found that for:

1. HT Ag Paste, the leaded-glass frit and silver corroded in the presences of diluted acetic acid, forming lead acetate and silver acetate over time. We suggest that these

corrosion products formed, accumulated, then dissolved back into the solution, approaching an equilibrium towards the end of the exposure.

2. LT Ag Paste, there was no detectable change in surface chemical composition using Raman spectroscopy mapping and XRD for the first 110 h of exposure. We suggest that this is due to phenol resin, which is well-suited to protect the Ag metal from corrosion during that timeframe. However, at the end of the 3000 h exposure, SEM and Raman spectroscopy mapping suggest that the LT Ag Paste is being affected by the diluted acetic acid, still to a lesser extent than HT Ag Paste and RSI.

3. RSI, the initial silver acetate in the RSI formulation dissolved in the diluted acetic acid, exposing the Ag for further corrosion into silver acetate. Similarly to HT Ag Paste, we suggest that silver acetate formed, accumulated, then dissolved back into the solution over time. Compared to HT Ag Paste, the dissolution reaction dominates sooner in the exposure, suggesting that the silver acetate present in the RSI initially might supply the dissolution reaction with silver acetate, reducing the amount of Ag consumed to form and dissolve silver acetate until equilibrium is met.

Comparing our results to those reported in literature suggest that our isolated exposure experiment is relevant to corrosion in degraded modules. With this new understanding of how each of these Ag-based metallizations react with acetic acid in an isolated environment, improved formulations can be designed to mitigate degradation due to corrosion. Specifically, we suggest that the initial presence of silver acetate in the RSI might reduce the amount of Ag consumed to reach an equilibrium between the formation and dissociation of silver acetate. Furthermore, we suggest the phenol resin additive in the LT Ag Paste is well-suited to protect Ag-based metallizations from corrosion from diluted

acetic acid, and therefore could be implemented as a capping layer to protect HT Ag Paste and RSI metallizations as well. Furthermore, we suggest that this process would occur in a module, but on a different time-scale as delivery of fresh acetic acid solution to the metallization surface is limited by diffusion compared to our setup.

6. SUMMARY OF REACTIVE SILVER INK METALLIZATION FOR NEXT GENERATION PHOTOVOLTAICS

The work presented in this dissertation focused on characterization and advancement of reactive ink metallizations. We have laid the ground work of evidence supporting the use of reactive ink metallizations for next generation photovoltaics. Compared to industry standard practices, we laid out a path to reduce silver usage per solar cell without compromising performance.

Specifically, this path consisted of evaluating the four primary factors that govern power losses from the front grid metallization and developing methodologies to tune these properties. First, this work demonstrated low media resistivity for reactive silver ink metallization (ρ_m, of ~ 2 μΩ·cm), lower than that of state-of-the-art low-cure-temperature Ag pastes. The relatively high purity (~97 % solid vol.) of the reactive silver ink metallization allows for reduction in finger resistance while using less Ag per solar cell compared to commercially available pastes.

Second, we demonstrated narrow finger widths (<100 μm) with dispense printing and studied process sensitivities which influence ink wettability, finger width, and optical properties. Third, the resistance between the grid and the underlying layer (ρ_c) was studied with and without the use of a Sn-sensitization layer. Through these studies, we examined the process of Sn-sensitization and Ag-activation on ITO surfaces, and determined that Sn-sensitization occurs on ITO surfaces, even for low Sn-sensitization solution concentrations that do not etch ITO, which has not been previously reported. We investigated adhesion, and studied processing parameters that influence reactive silver ink adhesion to ITO.

Fourth, we evaluated performance of silicon heterojunction solar cells with front grids formed from reactive silver ink, and from a commercially available low-cure temperature Ag paste; from this we demonstrated better performance for a reactive silver ink cell. Furthermore, we evaluated performance and series resistance throughout industry standard reliability damp heat testing. Through these studies, we demonstrated a “pass” of the IEC61215 DH1000 test for a silicon heterojunction cell with reactive silver ink front grid metallization. Finally, we developed a method to study corrosion of three Ag-based metallizations exposed to diluted acetic acid in an isolated environment. Significantly, we found that this isolated exposure is comparable and relevant to corrosion in field-degraded modules. This study revealed that RSI metallization forms, and dissolves corrosion products at a different rate than HT Ag Paste. This laid the ground work for future studies on the role of initial silver acetate content in the metallization formulation on the corrosion of Ag-based metallizations.

This work not only evaluated and demonstrated potential of a novel metallization technique –dispense printing of reactive inks –to become a high efficiency replacement for solar cell metallization; This work used reactive silver inks as a prototype, which in the future, can be extended to other reactive inks such as Cu reactive inks as the photovoltaic industry continues to minimize Ag consumption.

7. ACCOMPLISHMENTS

7.1 Peer-Reviewed Journal Publications

1. **A. M. Jeffries**, T. Neitzold, M. I. Bertoni, "Corrosion of Silver-Based Metallizations in Diluted Acetic Acid", *in progress, submitted to Journal of Photovoltaics, 2019.*

2. **A. M. Jeffries**, A. Mamidanna, Z. Wang, O. Hildreth, B. Opila, and M. I. Bertoni, "Tin Sensitization and Silver Activation on Indium Tin Oxide", *in progress, submitted to Applied Surface Science, or Surface and Coatings Technology, 2019*.

3. A. Mamidanna, **A. M. Jeffries**, M. I. Bertoni, and O. Hildreth, "Adhesion of Reactive Silver Inks on Indium Tin Oxide" Journal of Materials Science, vol. 54, no. 4, pp. 3125-3134, 2018.

4. X. Meng, M. Stuckelberger, L. Ding, B. West, **A. M. Jeffries**, and M. I. Bertoni, "Quantitative Mapping of Deflection and Stress on Encapsulated Silicon Solar Cells", Journal of Photovoltaics, vol. 8, no. 1, pp. 189 - 195, 2018.

5. **A. M. Jeffries**, A. Mamidanna, L. Ding, O. Hildreth, and M. I. Bertoni, "Low-temperature drop-on-demand reactive silver inks for solar cell front grid metallization", Journal of Photovoltaics, vol. 7, no. 1, pp. 37–43, 2017.

6. **A. M. Jeffries**, L. Ding, J. J. Williams, T. L. Williamson, M. A. Hoffbauer, C. B. Honsberg, and M. I. Bertoni, "Gallium nitride grown by molecular beam epitaxy at low temperatures", Thin Solid Films, *under review*.

7. B. West, M. Stuckelberger, **A.M. Jeffries**, S. Gangam, B. Lai, B. Stripe, J. Maser, V. Rose, S. Vogt, and M. I. Bertoni, "X-ray Fluorescence at Nanoscale Resolution for Multicomponent Layered Structures: A Solar Cell Case Study", Journal of Synchrotron Radiation 24, pp. 288-295, 2017.

7.2 Patents

1. Patent Disclosure M17-053P, Binding Technology for Reactive Inks, 2016.

2. Patent Disclosure M17-035P, Application of High Precision Printing for Solar Cell Technologies, 2016.

3. Provisional US Patent 62/406,836, Conductive Adhesion Promoters for Reactive Silver Inks, 2016.

7.3 Conference Proceedings

1. **A. M. Jeffries** and M. I. Bertoni, “Reactive Silver Ink as a Novel Low-Temperature Metallization: Monitoring Corrosion”, 2018 7th World Conference on Photovoltaic Energy Conversion, Waikoloa, HI pp. 1984-1988. 2018.

2. **A. M. Jeffries**, A. Mamidanna, L. Ding, O. Hildreth and M. I. Bertoni, “Reactive silver ink as front contacts for high efficiency silicon heterojunction solar cells,” 2016 IEEE 43rd Photovoltaic Specialists Conference (PVSC), Portland, OR, pp. 1984-1988. 2016.

3. X. Meng, M. Stuckelberger, L. Ding, B. West, **A. M. Jeffries** and M. Bertoni, Characterization of encapsulated solar cells by x-ray topography, Proceedings of the 43rd IEEE Photovoltaic Specialist Conference, Portland, OR, pp. 0111 – 0114, 2016.

4. **A. M. Jeffries**, A. Mamidanna, J. Clenney, L. Ding, O. Hildreth, and Mariana Bertoni, “Innovative Methods for Low-Temperature Contact Formation for Photovoltaic Applications”, Proceedings of the 42nd IEEE Photovoltaic Specialist Conference, pp. 1-5, New Orleans, LA, 2015.

5. B. West, H. Guthrey, L. Chen, **A. M. Jeffries**, S. Bernardini, B. Lai, J. Maser, W. Shafarman, M. Al-Jassim, and M. I. Bertoni, “Electrical and compositional characterization of gallium grading in Cu(In,Ga)Se2 solar cells”, Proceedings of the 40th IEEE Photovoltaic Specialist Conference, pp. 1726-1728, Denver, CO, 2014.

6. J. J. Williams, **A. M. Jeffries**, L. Ding, S. Gangam, K.Ghosh, T. L. Williamson, M. I. Bertoni, C. B. Honsberg, Structural and optical investigations of GaN-Si interface for a heterojunction solar cell, Proceedings of the 40th IEEE Photovoltaic Specialist Conference, pp. 0841-0843, Denver, CO, 2014.

7. L. Ding, M. Boccard, J. Williams, **A. M. Jeffries**, S. Gangam, K. Ghosh, C. Honsberg, S. Bowden, Z. Holman, H. Atwater, T. Buonassisi, S. Bremner, M. Green, C. Ballif, and M. I. Bertoni, “Thin silicon solar cells: A path to 35% Shockley-Queisser limits, a doe funded FPACE II project”, Proceedings of the 40th IEEE Photovoltaic Specialist Conference, pp. 2464-2470, Denver, CO, 2014.

8. **A. M. Jeffries**, S. Bowden, C. Honsberg and M. Bertoni, “Sensitivity analysis of materials availability for terawatt PV deployment,” 2013 IEEE 39th Photovoltaic Specialists Conference (PVSC), Tampa, FL, 2013.

9. S. Gangam, D.P. Fenning, **A. M. Jeffries**, S. Hudelson, B. Newman, M.A. Marcus, S. Fakra, B. Lai, J. Maser, T. Buonassisi, and M. I. Bertoni, "In-situ stage development for high-temperature X-ray nanocharacterization of defects in solar cells", Proceedings of the 39th IEEE Photovoltaic Specialist Conference, pp. 1394-1395, Tampa, FL, 2013.

7.4 Presentations

1. **A. M. Jeffries**, A. Mamidanna, O. Hildreth, and M. I. Bertoni, "Reactive Silver Ink as a Novel Low-Temperature Metallization: Performance & Degradation", 7th Workshop on Metallization & Interconnection for Crystalline Silicon Solar Cells, Konstanz, Germany, 2017. (oral)
2. **A. M. Jeffries**, A. Mamidanna, Hildreth and M. I. Bertoni, "Optimization of Reactive Silver Ink Fingers for Silicon Heterojunction Solar Cells," 9th International Workshop on Crystalline Silicon for Solar Cells (CSSC-9) 3rd Silicon Materials Workshop, 2016. (poster)
3. **A. M. Jeffries**, A. Mamidanna, Hildreth and M. I. Bertoni, "Optimization of Reactive Silver Ink Fingers for Silicon Heterojunction Solar Cells," Arizona Student Energy Conference, Flagstaff, AZ, 2016. (poster)
4. **A. M. Jeffries**, A. Mamidanna, L. Ding, O. Hildreth and M. I. Bertoni, "Reactive silver ink as front contacts for high efficiency silicon heterojunction solar cells," 2016 IEEE 43rd Photovoltaic Specialists Conference (PVSC), 2016. (oral)
5. **A. M. Jeffries**, A. Mamidanna, Hildreth and M. I. Bertoni, "Optical Characteristics of Reactive Silver Inks as Front Electrodes for High Efficiency Silicon Heterojunction Solar Cells", Materials Research Society Spring 2016 Meeting and Exhibit, 2016. (oral)
6. **A. M. Jeffries**, A. Mamidanna, J. Clenney, L. Ding, O. Hildreth, and Mariana Bertoni, "Innovative Methods for Low-Temperature Contact Formation for Photovoltaic Applications", 42nd IEEE Photovoltaic Specialist Conference, 2015. (poster)
7. L. Ding, M. Boccard, J. Williams, **A. M. Jeffries**, S. Gangam, K. Ghosh, C. Honsberg, S. Bowden, Z. Holman, H. Atwater, T. Buonassisi, S. Bremner, M. Green, C. Ballif, and M. I. Bertoni, "Thin silicon solar cells: A path to 35% Shockley-Queisser limits, a doe funded FPACE II project", 40th IEEE Photovoltaic Specialist Conference, 2014. (poster)

8. **A. M. Jeffries**, S. Bowden, C. Honsberg and M. Bertoni, "Sensitivity analysis of materials availability for terawatt PV deployment," 39th IEEE Photovoltaic Specialists Conference (PVSC), 2013. (oral)

7.5 Awards

April Jeffries - Distinguished Poster Award Arizona Student Energy Conference 2016: "Optimization of Reactive Silver Ink Fingers for Silicon Heterojunction Solar Cells".

8. REFERENCES

[1] International Panel on Climate Change, “Fifth Assessment Report on Climate Chang,” 2015.

[2] D. B. Needleman, J. R. Poindexter, R. C. Kurchin, I. Marius Peters, G. Wilson, and T. Buonassisi, “Economically sustainable scaling of photovoltaics to meet climate targets,” *Energy Environ. Sci.*, vol. 9, no. 6, pp. 2122–2129, 2016.

[3] A. Feltrin and A. Freundlich, “Material considerations for terawatt level deployment of photovoltaics,” *Renew. Energy*, vol. 33, no. 2, pp. 180–185, 2008.

[4] M. Z. Jacobson and M. A. Delucchi, “A Path to Sustainable Energy by 2030,” *Sci. Am.*, vol. 301, no. 5, pp. 58–65, Nov. 2009.

[5] Solar Energy Industries Association, “Solar Industry Data, Solar Industry Growing at a Record Pace,” 2017. [Online]. Available: http://www.seia.org/research-resources/solar-industry-data.

[6] V. Jean, J., Brown, P.R., Jaffe, R., Buonassisi, T., Bulovic, “Pathways for Solar Photovoltaics,” *Energy Environ. Sci.*, vol. 8, no. 4, 2015.

[7] A. Louwen, W. van Sark, R. Schropp, and A. Faaij, “A cost roadmap for silicon heterojunction solar cells,” *Sol. Energy Mater. Sol. Cells*, vol. 147, pp. 295–314, Apr. 2016.

[8] ITRPV, “International Technology Roadmap for Photovolatics 2015 Results,” 2016.

[9] R. Jones-Albertus, D. Feldman, R. Fu, K. Horowitz, and M. Woodhouse, “Technology advances needed for photovoltaics to achieve widespread grid price parity,” *Prog. Photovoltaics Res. Appl.*, vol. 24, no. 9, pp. 1272–1283, Sep. 2016.

[10] S. Blair, N.; Dobos, A.; Freeman, J.; Neises, T.; Wagner, M.; Ferguson, T.; Gilman, P.; Janzou, “System Advisor Model.” National Renewable Energy Laboratory, Golden, CO, 2014.

[11] D. M. Powell, R. Fu, K. Horowitz, P. A. Basore, M. Woodhouse, and T. Buonassisi, “The capital intensity of photovoltaics manufacturing: barrier to scale and opportunity for innovation,” *Energy Environ. Sci.*, vol. 8, no. 12, pp. 3395–3408, 2015.

[12] S. Hegedus, “Thin film solar modules: the low cost, high throughput and versatile alternative to Si wafers,” *Prog. Photovoltaics*, vol. 14, no. 5, pp. 393–411, 2006.

[13] P. G. Coll, R. Meier, and M. Bertoni, “Dynamics of Crack Propagation during Silicon Spalling,” in *2018 IEEE 7th World Conference on Photovoltaic Energy Conversion (WCPEC) (A Joint Conference of 45th IEEE PVSC, 28th PVSEC & 34th EU PVSEC)*, 2018, pp. 2537–2539.

[14] “Silver Prices Today, Live Spot Prices & Historical Charts,” *Money Metals Exchange*, 2019. [Online]. Available: https://www.moneymetals.com/precious-metals-charts/silver-price. [Accessed: 01-Jan-2019].

[15] M. A. Green, “Ag requirements for silicon wafer-based solar cells,” *Prog. Photovoltaics Res. Appl.*, vol. 19, no. 8, pp. 911–916, Dec. 2011.

[16] J. J. Williams, A. M. Jeffries, L. Ding, S. Gangam, K. Ghosh, L. Todd, M. I. Bertoni, and C. B. Honsberg, “Structural and Optical Investigations of GaN-Si Interface for a Heterojunction Solar Cell,” pp. 3–5, 2014.

[17] G. Niu, X. Guo, and L. Wang, "Review of recent progress in chemical stability of perovskite solar cells," *J. Mater. Chem. A*, vol. 3, no. 17, pp. 8970–8980, 2015.

[18] H. Meier, U. Löffelmann, D. Mager, P. J. Smith, and J. G. Korvink, "Inkjetprinted, conductive, 25 uμm wide silver tracks on unstructured polyimide," *Phys. Status Solidi Appl. Mater. Sci.*, vol. 206, no. 7, pp. 1626–1630, 2009.

[19] D. M. Powell, M. T. Winkler, A. Goodrich, and T. Buonassisi, "Modeling the cost and minimum sustainable price of crystalline silicon photovoltaic manufacturing in the United States," in *2012 IEEE 38th Photovoltaic Specialists Conference (PVSC) PART 2*, 2013, pp. 1–8.

[20] M. Wolf and H. Rauschenbach, "Series resistance effects on solar cell measurements," *Adv. Energy Convers.*, vol. 3, no. 2, pp. 455–479, 1963.

[21] D. L. Meier and D. K. Schroder, "Contact resistance: Its measurement and relative importance to power loss in a solar cell," *IEEE Trans. Electron Devices*, vol. 31, no. 5, pp. 647–653, May 1984.

[22] D. S. McLachlan, M. Blaszkiewicz, and R. E. Newnham, "Electrical Resistivity of Composites," *J. Am. Ceram. Soc.*, vol. 73, no. 8, pp. 2187–2203, Aug. 1990.

[23] T. J. Kurtz, S., Wohlgemuth, J., Kempe, M., Hacke, P., Jordan, D., Miller, D.C., Silverman, "Photovoltaic Module Qualification Plus Testing," Golden, CO, 2013.

[24] T. Shanmugam, V.,, Wong, J., Peters, I. M., Cunnusamy, J., Zahn, M., Zhou, A., Yang, R., Chen, X., Aberle, A. G., Mueller, "Analysis of Fine-Line Screen and Stencil-Printed Metal Contacts for Silicon Wafer Solar Cells," *IEEE J. Photovoltaics*, vol. 5, no. 2, pp. 525–533, 2015.

[25] A. Mette, "New Concepts for Front Side Metallization of Inductrial Silicon Solar Cells," Fraunhofer-Institute for Solar Energy, 2007.

[26] Y. Aleeva and B. Pignataro, "Recent advances in upscalable wet methods and ink formulations for printed electronics," *J. Mater. Chem. C*, vol. 2, no. 32, pp. 6436–6453, 2014.

[27] A. Ebong and N. Chen, "Metallization of crystalline silicon solar cells: A review," in *High Capacity Optical Networks and Emerging/Enabling Technologies*, 2012, pp. 102–109.

[28] H. Hannebauer, T. Dullweber, T. Falcon, X. Chen, and R. Brendel, "Record Low Ag Paste Consumption of 67.7 mg with Dual Print," *Energy Procedia*, vol. 43, pp. 66–71, 2013.

[29] J. D. Fields, M. I. Ahmad, V. L. Pool, J. Yu, D. G. Van Campen, P. A. Parilla, M. F. Toney, and M. F. A. M. van Hest, "The formation mechanism for printed silver-contacts for silicon solar cells," *Nat. Commun.*, vol. 7, pp. 11143, Apr. 2016.

[30] S. De Wolf, A. Descoeudres, Z. C. Holman, and C. Ballif, "High-efficiency Silicon Heterojunction Solar Cells : A Review," vol. 2, pp. 7–24, 2012.

[31] S. De Wolf and M. Kondo, "Nature of doped a-Si:H/c-Si interface recombination," *J. Appl. Phys.*, vol. 105, 2009.

[32] H. Yang and C. S. Davis, "Silver Pastes Capable of Narrow Line, High Aspect Ratio and High Pastes Transferability for Knotless High Mesh Screen Printing," in *2018 IEEE 7th World Conference on Photovoltaic Energy Conversion (WCPEC) (A Joint Conference of 45th IEEE PVSC, 28th PVSEC & 34th EU PVSEC)*, 2018, pp. 1079–1080.

[33] M. Pospischil, M. Kuchler, M. Klawitter, C. Rodríguez, M. Padilla, R. Efinger, M. Linse, A.

Padilla, H. Gentischer, M. König, M. Hörteis, L. Wende, O. Doll, R. Zengerle, F. Clement, and D. Biro, “Dispensing Technology on the Route to an Industrial Metallization Process,” *Energy Procedia*, vol. 67, pp. 138–146, Apr. 2015.

[34] U.S. Geological Survey, “U.S. Geological Survey: Mineral commodity summaries 2016,” Washington, D.C., 2016.

[35] H. Tokuhisa, M. Yoshida, U. Itoh, I. Sumita, S. Sekine, and T. Kamata, “Glass-fritless Cu alloy pastes for silicon solar cells recquiring low temperature sintering,” in *2011 37th IEEE Photovoltaic Specialists Conference*, 2011, pp. 001140–001143.

[36] P. Chien, Y., Chen, M., Chang, J., Liu, J. S. Q, Chang, Y., Huang, M., Yang, “Metallization optimization for high efficiency silicon heterojunction solar cells using low-temperature paste screen printing,” *39th IEEE Photovoltaics Spec. Conf.*, 2013.

[37] Y. Farraj, M. Grouchko, and S. Magdassi, “Self-reudction of a copper complex MOD ink for inkjet printing conductive patterns on plastics,” *Chemi. Commun.*, vol. 51, pp. 1587, 2015.

[38] A. Lennon, Y. Yao, and S. Wenham, “Evolution of metal plating for silicon solar cell metallisation,” *Prog. Photovoltaics Res. Appl.*, vol. 21, no. 7, pp. 1454–1468, Nov. 2013.

[39] A. J. Lennon, A. W. Y. Ho-Baillie, and S. R. Wenham, “Direct patterned etching of silicon dioxide and silicon nitride dielectric layers by inkjet printing,” *Sol. Energy Mater. Sol. Cells*, vol. 93, no. 10, pp. 1865–1874, Oct. 2009.

[40] B. R. BABU, S. U. BHANU, and K. S. MEERA, “Waste Minimization in Electroplating Industries: A Review,” *J. Environ. Sci. Heal. Part C*, vol. 27, no. 3, pp. 155–177, Aug. 2009.

[41] M. Singh, H. M. Haverinen, P. Dhagat, and G. E. Jabbour, “Inkjet Printing-Process and Its Applications,” *Adv. Mater.*, vol. 22, no. 6, pp. 673–685, Feb. 2010.

[42] J. Perelaer, P. J. Smith, D. Mager, D. Soltman, S. K. Volkman, V. Subramanian, J. G. Korvink, and U. S. Schubert, “Printed electronics: the challenges involved in printing devices, interconnects, and contacts based on inorganic materials,” *J. Mater. Chem.*, vol. 20, no. 39, pp. 8446, 2010.

[43] S. B. Walker and J. A. Lewis, “Reactive Silver Inks for Patterning High-Conductivity Features at Mild Temperatures,” *J. Am. Chem. Soc.*, vol. 134, no. 3, pp. 1419–1421, Jan. 2012.

[44] S. G. A. Gautrein, C. Schmiga, M. Glatthaar, W. Tremel, “Nanometallic Silver Inks for Metallization of ITO-Coated Silicon Solar Cells: Influence of Organic Components,” in *29th European Photovoltaic Solar Energy Conference and Exhibition*, 2014.

[45] S. B. Walker and J. a. Lewis, “Reactive silver inks for patterning high-conductivity features at mild temperatures,” *J. Am. Chem. Soc.*, vol. 134, no. 3, pp. 1419–1421, 2012.

[46] N. T. K. Thanh, N. Maclean, and S. Mahiddine, “Mechanisms of Nucleation and Growth of Nanoparticles in Solution,” *Chem. Rev.*, vol. 114, no. 15, pp. 7610–7630, Aug. 2014.

[47] O. Lefky, C. S., Mamidanna, A., Huang, Y., Hildreth, “Impact of Solvent Selection and Temperature on Porosity and Resistance of Printed Self- Reducing Silver Inks.,” *Phys. Status Solidi Appl. Mater. Sci.*, 2016.

[48] A. K. Galeway, D. M. Jamieson, and M. E. Brown, “Thermal Decompotion of Three Crystalline Modifications of Anhydrous Copper (II) Formate,” *J. Phys. Chem.*, vol. 78, pp. 2664–2670, 1974.

[49] D. Shin, S. Woo, H. Yem, M. Cha, S. Cho, M. Kang, S. Jeong, Y. Kim, K. Kang, and Y. Piao, "Self-Reducible and Alcohol-Soluble Copper-Based Metal-Organic Decomposition Ink for Printed Electronics," *ACS Appl. Mater. Interfaces*, vol. 6, pp. 3312–3319, 2014.

[50] D. Kim, S. Jeong, B. K. Park, and J. Moon, "Direct writing of silver conductive patterns: Improvement of film morphology and conductance by controlling solvent compositions," *Appl. Phys. Lett.*, vol. 89, no. 26, pp. 264101, Dec. 2006.

[51] D. Pesach and A. Marmur, "Marangoni effects in the spreading of liquid mixtures on a solid," *Langmuir*, vol. 3, no. 4, pp. 519–524, Jul. 1987.

[52] X. Wei and D. K. Roper, "Tin Sensitization for Electroless Plating Review," *J. Electrochem. Soc.*, vol. 161, no. 5, pp. D235–D242, Mar. 2014.

[53] P. Metals, "HISTORICAL SILVER/COPPER SPOT PRICE CHART," 2019. [Online]. Available: https://www.providentmetals.com/spot-price/chart/silver/. [Accessed: 21-Jan-2019].

[54] A. M. Jeffries, A. Mamidanna, L. Ding, O. J. Hildreth, and M. I. Bertoni, "Low-Temperature Drop-on-Demand Reactive Silver Inks for Solar Cell Front-Grid Metallization," *IEEE J. Photovoltaics*, vol. 7, no. 1, pp. 37–43, Jan. 2017.

[55] National Renewable Energy Laboratory, "Best Research-Cell Efficiencies," 2015.

[56] M. Taguchi, A. Terakawa, E. Maruyama, and M. Tanaka, "Obtaining a higherVoc in HIT cells," *Prog. Photovoltaics Res. Appl.*, vol. 13, no. 6, pp. 481–488, Sep. 2005.

[57] D. Li, D. Sutton, A. Burgess, D. Graham, and P. D. Calvert, "Conductive copper and nickel lines via reactive inkjet printing," *J. Mater. Chem.*, vol. 19, no. 22, pp. 3719, 2009.

[58] Y. Tao, Y. Tao, B. Wang, L. Wang, and Y. Tai, "A facile approach to a silver conductive ink with high performance for macroelectronics," *Nanoscale Res. Lett.*, vol. 8, no. 1, pp. 1–6, 2013.

[59] Demaurex, B., De Wolf, S., Descoeudres, A., Holman, Z.C., and C. Ballif, "Damage at hydrogenated amorphous/crystalline silicon interfaces by indium tin oxide overlayer sputtering," *Appl. Phys. Lett.*, vol. 101, no. 17, pp. 171604, 2012.

[60] V. Shapovalov, "Porous Metals.," *MRS Bull.*, vol. 19, no. 04, pp. 24–28, Apr. 1994.

[61] L. J. Cunningham and A. J. Braundmeier, "Measurement of the correlation between the specular reflectance and surface roughness of Ag films," *Phys. Rev. B*, vol. 14, no. 2, pp. 479–483, Jul. 1976.

[62] G. Rasigni, F. Varnier, M. Rasigni, J. P. Palmari, and A. Llebaria, "Roughness spectrum and surface plasmons for surfaces of silver, copper, gold, and magnesium deposits," *Phys. Rev. B*, vol. 27, no. 2, pp. 819–830, Jan. 1983.

[63] D. Pysch, a. Mette, and S. W. Glunz, "A review and comparison of different methods to determine the series resistance of solar cells," *Sol. Energy Mater. Sol. Cells*, vol. 91, no. 18, pp. 1698–1706, 2007.

[64] S. R. Aberle, A.G., Wenham and M. a Green, "Series Resistance of Solar Cells," in *Photovoltaic Specialist Conference, 1993., IEEE*, 1993, pp. 133–139.

[65] Z. Zhao, A. Mamidanna, C. Lefky, O. Hildreth, and T. L. Alford, "A percolative approach to investigate electromigration failure in printed Ag structures," *J. Appl. Phys.*, vol. 120, no. 12, pp.

125104, Sep. 2016.

[66] A. Mamidanna, A. M. Jeffries, M. I. Bertoni, and O. Hildreth, “Adhesion of Reactive Silver Ink on Indium Tin Oxide,” *Phys. Status Solidi*, vol. submitted, 2018.

[67] X. Wei and D. K. Roper, “Tin Sensitization for Electroless Plating Review,” *J. Electrochem. Soc.*, vol. 161, no. 5, pp. D235–D242, Mar. 2014.

[68] C. H. de Minjer and P. F. J. v. d. Boom, “The Nucleation with SnCl[sub 2]-PdCl[sub 2] Solutions of Glass Before Electroless Plating,” *J. Electrochem. Soc.*, vol. 120, no. 12, pp. 1644, 1973.

[69] J. J. Kim and S. H. Cha, “Optimized Surface Treatment of Indium Tin Oxide (ITO) for Copper Electroless Plating,” *Jpn. J. Appl. Phys.*, vol. 41, no. Part 2, No. 11A, pp. L1269–L1271, Nov. 2002.

[70] J. A. Chaney and P. E. Pehrsson, “Work function changes and surface chemistry of oxygen , hydrogen , and carbon on indium tin oxide,” *Appl. Surf. Sci.*, vol. 180, pp. 214–226, 2001.

[71] D. J. Milliron, I. G. Hill, C. Shen, A. Kahn, and J. Schwartz, “Surface oxidation activates indium tin oxide for hole injection,” *J. Appl. Phys.*, vol. 87, no. 1, pp. 572–576, Jan. 2000.

[72] M. Brumbach, P. A. Veneman, F. S. Marrikar, T. Schulmeyer, A. Simmonds, W. Xia, P. Lee, and N. R. Armstrong, “Surface Composition and Electrical and Electrochemical Properties of Freshly Deposited and Acid-Etched Indium Tin Oxide Electrodes,” *Langmuir*, vol. 23, no. 22, pp. 11089–11099, Oct. 2007.

[73] D. Lu, Y. Wu, J. Guo, G. Lu, Y. Wang, and J. Shen, “Surface treatment of indium tin oxide by oxygen-plasma for organic light-emitting diodes,” *Mater. Sci. Eng. B*, vol. 97, no. 2, pp. 141–144, Jan. 2003.

[74] D. P. Thomas, T. M., Williamson, D. L., Rainville, “Role of Tin Complexes in Bonding Silver to Glass: Mossbauer Studies,” in *Industrial Applications of the Mössbauer Effect*, Plenum Publishing, 1986, pp. 715–723.

[75] J. J. Kim, S.-K. Kim, and Y. S. Kim, “A Novel Method for Cu Electrodeposition on Indium Tin Oxide Aided by Two-Step Sn-Pd Activation,” *Jpn. J. Appl. Phys.*, vol. 42, no. Part 2, No.9A/B, pp. L1080–L1082, Sep. 2003.

[76] C. . Huang, Y. . Su, and S. . Wu, “The effect of solvent on the etching of ITO electrode,” *Mater. Chem. Phys.*, vol. 84, no. 1, pp. 146–150, Mar. 2004.

[77] D. P. Chitvoranund, N., Jiemsirilers, S., Kashima, “Effects of surface treatments on adhesion of silver film on glass substrate fabricated by electroless plating,” *J. Aust. Ceram. Soc.*, vol. 49, no. 1, pp. 62–69, 2013.

[78] M. Marinkovic, “Contact resistance effects in thin film solar cells and thin film transistors,” Jacobs University, 2013.

[79] M. Hoheisel, A. Mitwalsky, and C. Mrotzek, “Microstructure and etching properties of sputtered indium—tin oxide (ITO),” *Phys. Status Solidi*, vol. 123, no. 2, pp. 461–472, Feb. 1991.

[80] D. L. Meier and D. K. Schroder, “Contact resistance: Its measurement and relative importance to power loss in a solar cell,” *IEEE Trans. Electron Devices*, vol. 31, no. 5, pp. 647–653, May 1984.

[81] G. S. Marlow and M. B. Das, “The effects of contact size and non-zero metal resistance on the

determination of specific contact resistance," *Solid. State. Electron.*, vol. 25, no. 2, pp. 91–94, Feb. 1982.

[82] K. He, X. Yang, H. Yan, J. Gong, S. Zhong, Q. Ou, and R. Liang, "Surface properties of indium tin oxide treated by Cl 2 inductively coupled plasma," *Appl. Surf. Sci.*, vol. 316, pp. 214–221, Oct. 2014.

[83] K. H. Lee, H. W. Jang, K.-B. Kim, Y.-H. Tak, and J.-L. Lee, "Mechanism for the increase of indium-tin-oxide work function by O2 inductively coupled plasma treatment," *J. Appl. Phys.*, vol. 95, no. 2, pp. 586–590, Jan. 2004.

[84] H. Y. Yu, X. D. Feng, D. Grozea, Z. H. Lu, R. N. S. Sodhi, A.-M. Hor, and H. Aziz, "Surface electronic structure of plasma-treated indium tin oxides," *Appl. Phys. Lett.*, vol. 78, no. 17, pp. 2595–2597, Apr. 2001.

[85] B. K. Lok, P. Y. Ng, X. Hu, and H. P. Low, "Effect of plasma treated ITO substrate on inkjet printing of conductive ink," in *2006 8th Electronics Packaging Technology Conference*, 2006, pp. 154–160.

[86] K. Sugiyama, H. Ishii, Y. Ouchi, and K. Seki, "Dependence of indium–tin–oxide work function on surface cleaning method as studied by ultraviolet and x-ray photoemission spectroscopies," *J. Appl. Phys.*, vol. 87, no. 1, pp. 295–298, Jan. 2000.

[87] J. J. Kim, S. H. Cha, J. J. Kim, S. H. Cha, Y. Lee, J. J. Kim, S. Kim, Y. S. Kim, G. Scheen, M. Bassu, A. Douchamps, C. Chang, C. Lin, M. Chen, C. Lin, P. Chen, M. Chen, T. Meen, W. R. Chen, and C. Huang, "Optimized Surface Treatment of Indium Tin Oxide (ITO) for Copper Electroless Plating silicon Optimized Surface Treatment of Indium Tin Oxide (ITO) for Copper Electroless Plating," *Jpn. J. Appl. Phys.*, vol. 41, no. 2, 2002.

[88] E. Uzunlar, Z. Wilson, and P. A. Kohl, "Electroless Copper Deposition Using Sn/Ag Catalyst on Epoxy Laminates," *J. Electrochem. Soc.*, vol. 160, no. 12, pp. D3237–D3246, Nov. 2013.

[89] M. I. Jeffries, A.M., Wang, Z., Oplia, R., Bertoni, "Tin Sensitization and Silver Activation on Indium Tin Oxide Surfaces," *Surf. Coatings Technol.*

[90] K. H. Lee, H. W. Jang, K. Kim, Y. Tak, and J. Lee, "Mechanism for the increase of indium-tin-oxide work function by O 2 inductively coupled plasma treatment Mechanism for the increase of indium-tin-oxide work function by O 2 inductively coupled plasma treatment," vol. 586, no. May 2015, pp. 2–7, 2007.

[91] A. Kumar and C. Zhou, "The Race To Replace Tin-Doped Indium Oxide: Which Material Will Win?," *ACS Nano*, vol. 4, no. 1, pp. 11–14, Jan. 2010.

[92] C. H. F. Peden, K. B. Kidd, and N. D. Shinn, "Metal/metal-oxide interfaces: A surface science approach to the study of adhesion," *J. Vac. Sci. Technol. A Vacuum, Surfaces, Film.*, vol. 9, no. 3, pp. 1518–1524, May 1991.

[93] N. F. M. Benjamin, P., Weaver, C., "Adhesion of metal films to glass," *Proc. R. Soc. London. Ser. A. Math. Phys. Sci.*, vol. 254, no. 1277, pp. 177–183, Feb. 1960.

[94] R. Thomas, Williamson, "Role of Tin Complexes in Bonding Silver to Glass: Mossbauer Studies," in *Industrial Applications of the Mossbauer Effect*, 1986, pp. 715–723.

[95] J. F. D'Amico, M. A. De Angelo, J. F. Henrickson, J. T. Kenney, and D. J. Sharp, "Selective Electroless Metal Deposition Using Patterned Photo-Oxidation of Sn(II) Sensitized Substrates," *J.*

Electrochem. Soc., vol. 118, no. 10, pp. 1695, 1971.

[96] L. R. Pederson, "Comparison of stannous and stannic chloride as sensitizing agents in the electroless deposition of silver on glass using X-ray photoelectron spectroscopy," *Sol. Energy Mater.*, vol. 6, no. 2, pp. 221–232, Jan. 1982.

[97] G. M. Dalpian, Y. Yan, and S.-H. Wei, "Impurity-induced phase stabilization of semiconductors," *Appl. Phys. Lett.*, vol. 89, no. 1, pp. 11907, 2006.

[98] P. B. Paramonov, S. A. Paniagua, P. J. Hotchkiss, S. C. Jones, N. R. Armstrong, S. R. Marder, and R. V May, "Theoretical Characterization of the Indium Tin Oxide Surface and of Its Binding Sites for Adsorption of Phosphonic Acid Monolayers Jean-Luc Bre Indium tin oxide (ITO) is currently the most widely used transparent electrode in organic light-emitting devi," *Chem. Mater.*, vol. 20, no. c, pp. 5131–5133, 2008.

[99] A. Descoeudres, L. Barraud, S. De Wolf, B. Strahm, D. Lachenal, C. Guérin, Z. C. Holman, F. Zicarelli, B. Demaurex, J. Seif, J. Holovsky, and C. Ballif, "Improved amorphous/crystalline silicon interface passivation by hydrogen plasma treatment," *Appl. Phys. Lett.*, vol. 99, no. 12, pp. 123506, Sep. 2011.

[100] F. Wang, X. Zhang, L. Wang, Y. Jiang, C. Wei, S. Xu, and Y. Zhao, "Improved amorphous/crystalline silicon interface passivation for heterojunction solar cells by low-temperature chemical vapor deposition and post-annealing treatment," *Phys. Chem. Chem. Phys.*, vol. 16, no. 37, pp. 20202, Aug. 2014.

[101] J. Wong, "Griddler: Intelligent computer aided design of complex solar cell metallization patterns," in *2013 IEEE 39th Photovoltaic Specialists Conference (PVSC)*, 2013, pp. 0933–0938.

[102] J. A. Chaney and P. E. Pehrsson, "Work function changes and surface chemistry of oxygen, hydrogen, and carbon on indium tin oxide," *Appl. Surf. Sci.*, vol. 180, no. 3–4, pp. 214–226, Aug. 2001.

[103] I. R. Arndt, R., Puto, "Basic Understanding of IEC Standard Testing for Photovoltaic Panels," *In Compliance Magazine*, In Compliance Magazine, 2010.

[104] C. Peike, S. Hoffmann, P. Hülsmann, B. Thaidigsmann, K. A. Weiβ, M. Koehl, and P. Bentz, "Origin of damp-heat induced cell degradation," *Sol. Energy Mater. Sol. Cells*, vol. 116, pp. 49–54, Sep. 2013.

[105] E. L. Meyer and E. E. van Dyk, "Assessing the Reliability and Degradation of Photovoltaic Module Performance Parameters," *IEEE Trans. Reliab.*, vol. 53, no. 1, pp. 83–92, Mar. 2004.

[106] J. Zhu, M. Koehl, S. Hoffmann, K. A. Berger, S. Zamini, I. Bennett, E. Gerritsen, P. Malbranche, P. Pugliatti, A. Di Stefano, F. Aleo, D. Bertani, F. Paletta, F. Roca, G. Graditi, M. Pellegrino, O. Zubillaga, F. J. C. Iranzo, A. Pozza, T. Sample, and R. Gottschalg, "Changes of solar cell parameters during damp-heat exposure," *Prog. Photovoltaics Res. Appl.*, vol. 24, no. 10, pp. 1346–1358, Oct. 2016.

[107] D. C. Jordan, C. Deline, S. Johnston, S. R. Rummel, B. Sekulic, P. Hacke, S. R. Kurtz, K. O. Davis, E. J. Schneller, X. Sun, M. A. Alam, and R. A. Sinton, "Silicon Heterojunction System Field Performance," *IEEE J. Photovoltaics*, vol. 8, no. 1, pp. 177–182, Jan. 2018.

[108] Z. C. Holman, A. Descoeudres, L. Barraud, F. Z. Fernandez, J. P. Seif, S. De Wolf, and C. Ballif, "Current Losses at the Front of Silicon Heterojunction Solar Cells," *IEEE J. Photovoltaics*, vol. 2, no. 1, pp. 7–15, Jan. 2012.

[109] D. Zhang, A. Tavakoliyaraki, Y. Wu, R. A. C. M. M. van Swaaij, and M. Zeman, "Influence of ITO deposition and post annealing on HIT solar cell structures," *Energy Procedia*, vol. 8, pp. 207–213, 2011.

[110] F. J. Czanderna, A.W., Pern, "Encapsulation of PV modules using ethylene vinyl acetate copolymer as a pottant: A critical review," *Sol. Energy Mater. Sol. Cells*, vol. 43, no. 2, pp. 101–181, 1996.

[111] I. Duerr, J. Bierbaum, J. Metzger, J. Richter, and D. Philipp, "Silver grid finger corrosion on snail track affected PV modules ΰ investigation on degradation products and mechanisms," *Energy Procedia*, vol. 98, pp. 74–85, 2016.

[112] C. Peike, T. Kaltenbach, K.-A. Weiß, and M. Koehl, "Non-destructive degradation analysis of encapsulants in PV modules by Raman Spectroscopy," *Sol. Energy Mater. Sol. Cells*, vol. 95, no. 7, pp. 1686–1693, Jul. 2011.

[113] T. E. Graedel, "Corrosion Mechanisms for Silver Exposed to the Atmosphere," *J. Electrochem. Soc.*, vol. 139, no. 7, pp. 1963, 1992.

[114] A. Kraft, L. Labusch, T. Ensslen, D. Ines, J. Bartsch, M. Glatthaar, S. Glunz, and A. S. C. Samples, "Investigation of Acetic Acid Corrosion Impact on Printed Solar Cell Contacts," *IEEE J. Photovoltaics*, vol. 5, no. 3, pp. 736–743, 2015.

[115] M. I. Jeffries, A.M., Neitzold, T., Schelas, L., Bertoni, "Corrosion of Silver-Based Metallizations in Diluted Acetic Acid," *IEEE J. Photovoltaics*.

[116] O. Lefky, C. Mamidanna, A., Hildreth, "Impact of solvent selection and temperature on porosity and resistance of printed self-reducing inks," *Submitt. Publ.*, 2016.

[117] M. D. Kempe, G. J. Jorgensen, K. M. Terwilliger, T. J. McMahon, C. E. Kennedy, and T. T. Borek, "Acetic acid production and glass transition concerns with ethylene-vinyl acetate used in photovoltaic devices," *Sol. Energy Mater. Sol. Cells*, vol. 91, no. 4, pp. 315–329, Feb. 2007.

[118] K. A. Eder, G., Voronko, Y., Knausz, M., Berger, "Permeation of water vapour, oxygen and acetic acid through PV-backsheets: correlation with material properties and ageing induced changes," in *EU PVSEC*, 2015.

[119] S. Marais, E. Bureau, F. Gouanvé, E. Ben Salem, Y. Hirata, A. Andrio, C. Cabot, and H. Atmani, "Transport of water and gases through EVA/PVC blend films—permeation and DSC investigations," *Polym. Test.*, vol. 23, no. 4, pp. 475–486, Jun. 2004.

[120] I. Martina, R. Wiesinger, D. Jembrih-Simburger, and M. Schreiner, "MICRO-RAMAN CHARACTERISATION OF SILVER CORROSION PRODUCTS: INSTRUMENTAL SET UP AND REFERENCE DATABASE," *e-Preservation Sci.*, vol. 9, pp. 1–8, 2012.

[121] S. Bernard, M.C., Costa, V., Joiret, "Assessing Indoor Lead Corrosion Using Raman Spectroscopy During Electrochemical Reduction," in *the 8th international conference of the Infrared and Raman Users' Group*, 2008.

[122] L. Burgio, R. J. H. Clark, and S. Firth, "Raman spectroscopy as a means for the identification of plattnerite (PbO2), of lead pigments and of their degradation products," *Analyst*, vol. 126, no. 2, pp. 222–227, 2001.

[123] P. Lu, J. Ding, R. Cheng, and R. Qian, "Suppression of fluorescence in raman spectroscopy of chromophore-containing polymer samples," *Macromol. Rapid Commun.*, vol. 15, no. 11, pp. 835–840, Nov. 1994.

[124] M. M. Fleischmann, M., Hill, I.R., Musiani, “A Raman spectroscopic investigation of the electropolymerization of phenol on silver electrodes,” *Electrochim. Acta*, vol. 28, no. 11, pp. 1545–1553, 1983.

[125] M. B. Hocking, “Phenyl acetate preparation from phenol and acetic acid: Reassessment of a common textbook misconception,” *J. Chem. Educ.*, vol. 57, no. 7, pp. 527, 1980.